

# Switchable silver clusters: crystals for novel electronics

THÈSE N° 7091 (2016)

PRÉSENTÉE LE 9 DÉCEMBRE 2016

À LA FACULTÉ DES SCIENCES ET TECHNIQUES DE L'INGÉNIEUR  
LABORATOIRE DES NANOMATÉRIAUX SUPRAMOLÉCULAIRES ET INTERFACES - CHAIRE CONSTELLIUM  
PROGRAMME DOCTORAL EN SCIENCE ET GÉNIE DES MATÉRIAUX

ÉCOLE POLYTECHNIQUE FÉDÉRALE DE LAUSANNE

POUR L'OBTENTION DU GRADE DE DOCTEUR ÈS SCIENCES

PAR

**Sergio ALLEGRI**

acceptée sur proposition du jury:

Prof. V. Michaud, présidente du jury  
Prof. F. Stellacci, directeur de thèse  
Prof. P. Samori, rapporteur  
Prof. T. Bürgi, rapporteur  
Prof. D. Damjanovic, rapporteur



ÉCOLE POLYTECHNIQUE  
FÉDÉRALE DE LAUSANNE

Suisse  
2016



# Acknowledgements

Firstly, I want to thank my advisor, Prof. Francesco Stellacci, who accepted and welcomed me in his laboratory. Francesco motivated me throughout the four years thanks to his endless passion for science. He always found time to discuss with me, giving me suggestions and advice.

I want to thank Prof. Thomas Bürgi, Prof. Dragan Damjanovic and Prof. Paolo Samorì for being part of my thesis committee; I would also like to thank Prof. Véronique Michaud for being the president of the committee.

The years at EPFL have been an incredible journey that allowed me to work with exceptional people, brilliant in science and life. My sincere acknowledgements go to: Prof. Holger Frauenrath and the whole LMOM group; Prof. Anna Fontcuberta i Morral and the LMSC people, but especially Dr. Alberto Casadei and Dr. Esther Alarcón Lladó; Prof. Nicola Marzari and Dr. Moraes de Almeida; again Prof. Dragan Damjanovic and Sina Hashemi Zadeh; Prof. Fabien Sorin and people of his lab, a special mention goes to Wei Yan; Dr. Arnaud Magrez who helped me with the power XRD experiment; Dr. Florance Pojer, Dr. Rosario Scopelliti and Dr. Euro Solari for the single crystal XRD experiments. Dr. Andrea Pisoni for teaching me how to use the FIB and helping me with the low temperature experiments. Dr. Igor Stolichnikov for his assistance with AFM and PFM experiments; Dr. Antonios Bazigos and Dr. Wladek Grabinski for the enormous help and assistance in the electrical characterization; Jury Sandrini, Mariazel Maqueda Lopez and Emanuele Casu for help and discussions; Michel Schär for introducing me to many characterization techniques; all the CMi staff for teaching me the tricks of microfabrication.

I also want to thank my external collaborators: Prof. Paolo Samorì for hosting and welcoming me in Strasbourg so many times; Prof. Osman Bakr for fruitful discussion on IBAN; Dr. Abdul Halim, or simply Lina, for having set up an export facility of IBAN crystals at KAUST for me; Prof. Emanuele Orgiu for hosting me and helping me with the characterization and for the immeasurable scientific support over Skype; Dr. Horst Puschmann from Olexsys, who guided me through the mystery of refining a crystal structure. Among the students I supervised I want to thank Pietro Clement, who worked on the electrical characterization of the crystals, and Graham Kimble, who did an incredible amount of work in a very limited amount of time. A mention goes to one student, Adrian Trömel, who helped for two semesters working by my side in a really tough project and eventually became a friend.

I'd like to thank Chrystelle Demierre and Anne Kolly for their assistance and help with administrative matters. Merci!

## Acknowledgements

---

Among the skills of Francesco that I admire, there is the ability of choosing extraordinary people to work with. Therefore, many people have worked in the SUNMIL group, but I really need to thank them all, because it was such a good experience being surrounded by them. Javier, Juan José, Mauro, Marta, Kislun, Kellen, Yun, Tam, Randy, Stefan, Maria, Paulo, Marie, Anna, Alejandro, Elif, Ahmet, Sam, Rosie, Huayan, Pelin, Chiara, Nikos, Özgün, Simone, Yulia, Matej, Shun, Lina, Adam, Zhi, Evi, Quy and Ula. A special mention goes to the "Merenda Club", originally composed of myself, Nikos and Maria, and then extended to Evi, Pelin, Ula, Matej and Rosie.

Outside the lab, I was lucky to be surrounded by sincere and good friends. I wish to thank Antonio, Lucian, Diego, Matteo for their initial support that has not finished yet; Carla, who tolerated me and laughed with me for nearly two years; Mario and Alessandra for their long distance support and lively friendship; those who arrived later, but that somehow have always been there, Ferdinando, Giovanna, Mariana, Bea, Pietro, Patrizia, Giulia, Gigi and Alberto.

Grazie alla mia famiglia. Ringrazio mia mamma e mio papà per avermi cresciuto, educato, bacchettato e sempre sostenuto. Grazie anche a mia sorella Perla, mio fratello Alessandro e alla sua famiglia.

Infine, voglio ringraziare la persona che da qualche mese è con me l'altro componente della mia nuova famiglia: Ombri. Per me sei stata e sempre sarai fonte d'ispirazione. Grazie!

*Lausanne, September 2016*

S. A.

# Abstract

Metallic nanoclusters form a family of novel materials with atomically defined hybrid organic/inorganic structures. Among these materials, clusters containing 44 silver atoms have emerged as one of the most interesting, because of their exceptional electronic and optical properties. Recently synthetic progresses made possible their crystallisation. Crystals of  $\text{Ag}_{44}$  clusters form what is defined as a superlattice, a periodic three dimensional structure, whose properties are expected to depend on the collective interaction of its constituents. In this thesis, clusters with a molecular formula  $\text{Ag}_{44}(\text{SC}_6\text{H}_4\text{F})_{30}^{4-}$  have been crystallized in the presence of four tetraphenyl phosphonium  $[(\text{C}_6\text{H}_5)_4\text{P}^+]$  counterions and the crystals have been fully characterized. The response of these crystals to an external electric field was then tested in a two- and four- terminal configuration, and showed conductivity switching at high voltages between a less and a more conductive phase. Single crystal X-ray diffraction measurements showed that each of the conductive phase was characterized by a different crystal structure, suggesting an electric-field induced phase transition. The change in properties is attributed to the collective displacement of the tetraphenyl phosphonium counterions, which causes a change in orientation of 3 of the 30 fluorophenyl thiols that coat the cluster. Overall all these local changes lead to a global redistribution of the charges in the crystal. To the best of my knowledge, this work presents the first experimental observation of the phenomenon due to a collective behavior in a crystal of nanoclusters as well as in a crystal with more than 1000 atoms in the unit cell.

Key words: nanocluster,  $\text{Ag}_{44}$ , superlattice, collective properties, thiol, XRD, phase transition.



## Sommario

I nanoaggregati metallici sono una famiglia di materiali nuovi con strutture ibride organiche/inorganiche dal numero di atomi definito. Tra tutti questi materiali, gli aggregati con 44 atomi d'argento hanno attirato l'attenzione della comunità scientifica a causa delle loro proprietà ottiche ed elettroniche. Di recente, grazie ai miglioramenti nella sintesi di questi aggregati, è stato possibile cristallizzarli. I cristalli di aggregati atomici d'argento costituiscono quelli che sono definiti superreticoli, vale a dire delle strutture ordinate tridimensionali, le cui proprietà scaturiscono dall'interazione collettiva dell'unità fondamentali del cristallo. In questa tesi sono stati sintetizzati aggregati, la cui formula molecolare è  $\text{Ag}_{44}(\text{SC}_6\text{H}_4\text{F})_{30}^{4-}$ , in presenza di quattro controioni (tetrafenilfosfonio  $(\text{C}_6\text{H}_5)_4\text{P}^+$ ). La risposta di questi cristalli a un campo elettrico esterno è stata studiata tramite l'impiego di misurazioni a due e a quattro terminali. La presenza di due stati conduttivi è stata verificata tramite misurazioni elettriche, oltre che da misure di diffrazione di singolo cristallo con raggi X, le quali hanno dimostrato l'esistenza di due strutture diverse, suggerendo la presenza di una transizione di fase indotta dal campo elettrico. Il cambiamento di proprietà è stato attribuito allo spostamento collettivo dei controioni, i quali a loro volta inducono uno spostamento di 3 dei 30 tioli che proteggono la superficie dell'agglomerato atomico. La conseguenza di questo spostamento è una ridistribuzione globale delle cariche all'interno del cristallo. Al meglio della nostra conoscenza, il lavoro svolto all'interno di questa tesi rappresenta la prima verifica sperimentale di una risposta collettiva di un cristallo di agglomerati, così come di un cristallo con più di 100 atomi.

Parole chiave: agglomerati,  $\text{Ag}_{44}$ , proprietà collettive, tioli, XRD, transizione di fase.





## Résumé

Les nanoclusters métalliques forment une famille de nouveaux matériaux avec des structures hybrides organiques/inorganiques atomiquement définies. Parmi ces matériaux, les clusters contenant 44 atomes d'argent ont émergé comme l'un des plus intéressants, en raison de leurs propriétés électroniques et optiques exceptionnelles. Récemment, les progrès en synthèse ont rendu possible leur cristallisation. Les cristaux de clusters  $\text{Ag}_{44}$  forment ce qui est défini comme un superréseau, une structure tridimensionnelle périodique, dont les propriétés devraient dépendre de l'interaction collective de ses constituants. Dans cette thèse, les clusters avec une formule moléculaire  $\text{Ag}_{44}(\text{SC}_6\text{H}_4\text{F})_{30}^{4-}$  ont été cristallisés en présence de quatre contre-ions tétraphényl phosphonium  $[(\text{C}_6\text{H}_5)_4\text{P}^+]$ . Ces cristaux ont été entièrement caractérisés. Leur réponse à un champ électrique externe a ensuite été testée dans une configuration à deux ou quatre bornes et montre la commutation de conductivité à haute tension entre une phase plus conductrice et moins conductrice. L'analyse de la diffraction des rayons X sur monocristal ont montré que chaque phase conductrice est caractérisée par une structure cristalline différente, ce qui indique une transition de phase induite par un champ électrique. La variation des propriétés est attribuée au déplacement collectif des contre-ions tétraphényl phosphonium, ce qui provoque un changement d'orientation de 3 des 30 thiols fluorophényl qui enrobent le cluster. Tous ces changements locaux conduisent à une redistribution globale des charges dans le cristal. Au meilleur de ma connaissance, ce travail présente la première observation expérimentale d'un phénomène dû à un comportement collectif dans un cristal de nanoclusters ainsi que dans un cristal avec plus de 1000 atomes dans la maille cristallographique.

Mots clefs : cluster,  $\text{Ag}_{44}$ , comportement collectif, superréseau, XRD, thiols, transition de phase.



# Contents

<b>Acknowledgements</b>	<b>i</b>
<b>Abstract (English/Italiano/Français)</b>	<b>iii</b>
<b>List of figures</b>	<b>xiii</b>
<b>List of tables</b>	<b>xv</b>
<b>Acronyms</b>	<b>xv</b>
<b>1 The Rise of Nanotechnology</b>	<b>1</b>
1.1 Thesis outline . . . . .	4
<b>2 Introduction</b>	<b>5</b>
2.1 Chapter outline . . . . .	5
2.2 Synthesis of noble metal nanoclusters . . . . .	5
2.2.1 Turkevich method . . . . .	5
2.2.2 Brust method . . . . .	6
2.2.3 Silver clusters synthesis . . . . .	8
2.3 Clusters stability: Jellium model and magic numbers . . . . .	9
2.3.1 The Jellium model . . . . .	9
2.3.2 Superatom theory and magic numbers . . . . .	10
2.4 Characterization . . . . .	12
2.4.1 Nuclear magnetic resonance . . . . .	12
2.4.2 Mass spectrometry . . . . .	12
2.4.3 Analytical ultracentrifugation . . . . .	13
2.4.4 Absorption spectroscopy . . . . .	13
2.4.5 Electron microscopies . . . . .	14
2.4.6 X-Ray . . . . .	14
2.5 Challenges . . . . .	14
2.5.1 Optical properties and circular dichroism . . . . .	15
2.5.2 Nanoclusters for catalysis . . . . .	15
2.5.3 Magnetic properties . . . . .	16
2.6 Collective properties . . . . .	16
	<b>ix</b>

## Contents

---

<b>3</b>	<b>Experimental section</b>	<b>19</b>
3.1	Chapter outline . . . . .	19
3.2	Synthesis . . . . .	20
3.3	Crystallisation of the silver nanoclusters . . . . .	21
3.3.1	Methods . . . . .	21
3.3.2	Results . . . . .	23
3.4	Characterization and fabrication . . . . .	25
3.4.1	Optical characterization . . . . .	25
3.4.2	X-ray diffraction . . . . .	26
3.4.3	Electron microscopy and elemental analysis . . . . .	28
3.4.4	Focused ion beam . . . . .	29
3.5	Electrical characterization . . . . .	31
3.5.1	Two-terminal IV curve . . . . .	31
3.5.2	Substrate fabrication and sample preparation . . . . .	34
3.5.3	Conductive AFM . . . . .	36
<b>4</b>	<b>Experimental results</b>	<b>37</b>
4.1	Chapter outline . . . . .	37
4.2	Optical properties . . . . .	37
4.2.1	Crystals microspectroscopy . . . . .	37
4.2.2	Polarised optical microscopy . . . . .	39
4.3	Electrical properties . . . . .	41
4.3.1	Two-terminal measurements . . . . .	41
4.3.2	Temperature dependence . . . . .	49
4.3.3	Mobility calculation . . . . .	53
4.3.4	Cluster versus crystal property . . . . .	55
4.4	Conductive AFM . . . . .	56
4.5	XRD . . . . .	59
4.5.1	Reproducibility . . . . .	62
4.6	A polymorph . . . . .	65
4.6.1	Electrical testing . . . . .	65
4.6.2	Polymorph XRD characterization . . . . .	67
<b>5</b>	<b>Discussion</b>	<b>69</b>
5.1	Chapter outline . . . . .	69
5.2	Analysis of the crystal conduction . . . . .	69
5.2.1	Schottky emission . . . . .	70
5.2.2	Hopping . . . . .	71
5.2.3	Tunnelling . . . . .	72
5.2.4	Summary . . . . .	77
5.3	Origin of the switching mechanism . . . . .	78
5.3.1	Similar phenomena . . . . .	78
5.3.2	Phase transition . . . . .	79

<b>6</b>	<b>Conclusion and perspectives</b>	<b>81</b>
<b>A</b>	<b>Microspectroscopy</b>	<b>83</b>
<b>B</b>	<b>Determining refractive index and complex dielectric function</b>	<b>85</b>
<b>C</b>	<b>Customized probe station</b>	<b>95</b>
<b>D</b>	<b>Conduction mechanism</b>	<b>97</b>
	D.1 Schottky emission . . . . .	97
	D.2 Poole-Frankel emission . . . . .	99
	D.3 Space charge limited current . . . . .	101
	D.4 Hopping . . . . .	101
	D.5 Tunnelling . . . . .	102
<b>E</b>	<b>Silver supercrystals simulations</b>	<b>105</b>
	<b>Curriculum Vitae</b>	<b>119</b>



# List of Figures

1.1	Cluster of $\text{Ag}_{44}$ . . . . .	2
1.2	Density of electronic states . . . . .	3
2.1	Single electron tunnelling . . . . .	6
2.2	First QSE appearance in Au clusters . . . . .	7
2.3	Absorption of $\text{Ag}_{44}$ -FTP silver clusters . . . . .	9
2.4	Ligand exchange reaction . . . . .	10
2.5	Shell closing numbers . . . . .	11
2.6	Structure of $\text{Na}_4\text{Ag}_{44}(\text{p-MBA})_{30}$ . . . . .	17
3.1	Resolved crystal structure of $\text{Ag}_{44}$ . . . . .	19
3.2	Examples of crystals . . . . .	22
3.3	Microscopy images of $\text{Ag}_{44}$ . . . . .	23
3.4	Crystallisation methods . . . . .	24
3.5	Film of $\text{Ag}_{44}(\text{FTP})_{30}$ . . . . .	24
3.6	Crystal UV-VIS spectrum . . . . .	26
3.7	X-rays scattering principles . . . . .	28
3.8	SEM of IBAN crystals . . . . .	30
3.9	Two-terminal configuration . . . . .	31
3.10	Schematic of the sample fabrication process . . . . .	34
3.11	SEM image of a device . . . . .	35
3.12	Damaged crystal during Pt deposition . . . . .	35
4.1	Crystal for microspectroscopy . . . . .	38
4.2	Complex refractive index . . . . .	39
4.3	POM of a crystal . . . . .	40
4.4	Crystal connection approach . . . . .	41
4.5	Crystal after contact . . . . .	42
4.6	Low voltage characteristic . . . . .	43
4.7	Current change . . . . .	43
4.8	Threshold voltage position . . . . .	44
4.9	Step-like increase in conductivity . . . . .	45
4.10	Length-width threshold appearance . . . . .	45
4.11	Switching off . . . . .	46

## List of Figures

---

4.12	Switching off features . . . . .	47
4.13	Comparison between different tips . . . . .	47
4.14	VHR mechanism . . . . .	49
4.15	Threshold voltage and temperature . . . . .	50
4.16	Jumps of conductivity . . . . .	50
4.17	VHR and activation energy . . . . .	51
4.18	Electron carrier mobility . . . . .	54
4.19	Pellet of clusters . . . . .	55
4.20	Conductive AFM . . . . .	57
4.21	AFM roughness of a measured crystal . . . . .	58
4.22	IV curves of crystal for XRD . . . . .	59
4.23	Crystals unit cells . . . . .	61
4.24	Overlay of crystal lattices . . . . .	63
4.25	Modification of the decorating motifs of $\text{Ag}_{44}(\text{FTP})_{30}$ . . . . .	64
4.26	Microscopy and SEM images of polymorph crystals . . . . .	65
4.27	Polymorph conductivity . . . . .	66
4.28	Comparison between polymorphs . . . . .	67
5.1	Schottky emission crystals fitting . . . . .	71
5.2	Hopping mechanism in 2D . . . . .	72
5.3	Direct and Fowler-Nordheim tunnelling mechanisms . . . . .	73
5.4	Transition between DT and FN mechanism . . . . .	74
5.5	DT-FN transition in molecular transistor . . . . .	74
5.6	RT and NDR schematic . . . . .	75
5.7	NDR in IBAN crystals . . . . .	76
5.8	Electrosatic potential for AgNC . . . . .	77
A.1	Modified microscope . . . . .	83
A.2	Beam size on ROI . . . . .	84
C.1	Glovebox setup . . . . .	96
D.1	Schottky field emission . . . . .	98
D.2	Schottky emission fitting . . . . .	99
D.3	Poole-Frenkel field emission . . . . .	100
D.4	Variable hopping range . . . . .	102
D.5	Tunnelling mechanisms . . . . .	103
E.1	Relaxed simulated structures . . . . .	106
E.2	HOMO-LUMO of the simulated structures . . . . .	106



# List of Tables

3.1	Beamline characteristics . . . . .	29
4.1	Compositional ratio of Ag-P, Ag-F and Ag-S . . . . .	42
4.2	Summary of switching mechanism . . . . .	48
4.3	Crystal data for $\text{Ag}_{44}(\text{FTP})_{30}$ . . . . .	60
4.4	Crystal data for $\text{Ag}_{44}(\text{FTP})_{30}$ polymorph . . . . .	68
E.1	Simulation cell sizes and geometry. . . . .	105
E.2	Band gaps . . . . .	105



# Acronyms

- 2NT** 2-naphthalenethiol. 16
- 4FTP** 4-fluorothiophenol. 8, 9, 20
- AFM** atomic force microscope. 1, 56
- Ag** silver. 3, 5
- AgNP** silver nanoparticle. 8
- Au** gold. 3, 5
- AUC** analytical ultracentrifugation. 13
- AuNP** gold nanoparticle. 3, 5
- DCM** dichloromethane. 20
- DFT** density functional theory. 17
- DMF** dimethylformamide. 8
- DOSY** diffusion-ordered NMR spectroscopy. 12
- DT** direct tunnel. 72
- DTNBA** dithiobisnitrobenzoic acid. 8
- EDX** energy-dispersive x-ray spectroscopy. 14, 29
- ESI** electrospray ionization. 12, 13
- FIB** focused ion beam. 30, 50
- FN** Fowler-Nordheim tunnel. 73
- HRTEM** high resolution transmission electron microscope. 14

## Acronyms

---

**IBAN** intensely and broadly absorbing nanoparticles. 8, 13, 25, 37

**KK** Kramers-Kronig relation. 86

**MALDI** matrix-assisted laser desorption ionization. 12

**MBA** mercaptobenzoic acid. 8

**MBDT** methyl dibenzothiophene. 8

**MBT** methylbenzothiophene. 8

**MNBA** mercaptonitrobenzoic acid. 8, 20

**MOS** metal-oxide-semiconductor. 76

**MPM** mercaptomethylphenylmethanol. 8

**MS** mass spectroscopy. 12, 14

**NC** nanocluster. 3–6

**NDR** negative differential resistance. 75

**NHR** nearest hopping range. 71

**NMR** nuclear magnetic resonance. 12

**NOESY** nuclear Overhauser effect NMR spectroscopy. 12

**PAGE** polyacrylamide gel-electrophoresis. 7

**QSE** quantum size effect. 3, 5–7

**ROI** region of interest. 83

**RT** resonant tunneling. 75

**RTD** resonant tunnelling diode. 72

**SCLC** space-charge limited current. 53, 101

**SEC** size exclusion chromatography. 7

**SEM** scanning electron microscope. 14, 29

**STM** scanning tunnelling microscope. 1, 6

**TBBT** 4-tert-butylbenzenethiolate. 15

**TEM** transmission electron microscope. 14

**TFL** trap-filled limit. 78

**TOF** time of flight. 12

**TPPB** tetraphenylphosphonium bromide. 8, 20

**VHR** variable hopping range. 49, 51, 71, 101

**XRD** x-ray diffraction. 14



# 1 The Rise of Nanotechnology

"There is plenty of room at the bottom" [1] . With this sentence Richard Feynman paved the way to what we nowadays call nanotechnology. In a talk to the American Physical Society held in Pasadena the 29th December 1959, he challenged scientist with a series of fascinating examples to pursue new frontiers of physics, and explore the smaller. For instance, he speculated [2] on the possibility of engraving the whole *Encyclopaedia Britannica* on the head of a pin, simply by miniaturizing each letter 25000 times, so small that we would have needed an electron microscope to read it. Since this first seminal talk, two others followed in 1983 and 1984 respectively, where again he described in detail how we could store all the books ever written, a number of which he approximated to be twenty five million: the letters of all the words could be written in a code of dots and dashes in a sequences of six or seven bits, and if each bit could be represented by a cube of five times five times five atoms, we would need  $10^{15}$  bits to represent all the words contained in the books. In term of cubes of atoms this is roughly equal to  $10^{18}$  atoms. Feynman concluded that "all of the information that man has carefully accumulated in all the books in the world can be written in this form, in a cube of material one two-hundredth of an inch wide, which is the barest piece of dust that can be made out by the human eye" [1]. Current technology, *i.e.* solid state memory, uses one million atoms per bit, still far from the 100 atoms hypothesized by Feynman, but two recent studies at EPFL pushed the limit of writing information down at a single atom level [3, 4], proving that Feynman was right in foreseeing the potential of making things small.

Feynman was capable of prophesying technologies that we currently use everyday in our laboratories: the electron microscope became widely available and, as he suggested, it was used to read and to write information below the diffraction limit of light [5]; atomic force (atomic force microscope (AFM)) [6] and scanning tunnelling microscopies (scanning tunnelling microscope (STM)) [7] have been invented and allowed to see single molecules and also move single atoms: scientists at IBM in California, by making use of these instruments, were able to realize the first ever made movie of an atom. This was realized stacking different frames of carbon oxide atoms moved with a STM.

It is worth to mention Feynman because he was not only able to predict the advent of the above

mentioned technologies, but in his seminal description of what we now call nanotechnology, he foresaw the potential of studying small objects. It is curious to notice that in his talk he did not mention the term "nanotechnology", which was later on coined by Japanese scientist Norio Taniguchi [8]. He used rather simple words such as "tiny machines", and he wondered "how small" machinery had to be so that physicists could ultimately help chemists in synthesizing new molecules, just by positioning one atom next to the other. As Feynman said: "As we go down and fiddle around with the atoms down there, we are working with different laws and we can expect to do different things. [...] We can use, not just circuits, but some system involving the quantized energy levels..." [1]. This thesis focuses on molecular assemblies (see Figure 1.1), constituted by a defined number of atoms, that match the definition of Feynman.

As we decrease the size of an object and we approach a characteristic dimension, the de Broglie wavelength of electron [9], classical laws are substituted by quantum physics laws, and we start dealing with the principle of indetermination and the particle-wave duality. For instance, one of the main differences between bulk metals and isolated metallic atoms is that the energy levels, as we shrink the size of matter, become discrete, quantized: electrons that in bulk metals are free to move in the so-called Fermi sea, become bound [10]. The free electrons model of Drude and Lorentz [11] describes successfully the electronic and optical properties of metals, but if we imagine decreasing the size of a metallic object down to an atom, we expect to observe a transition from a classical to a quantum behaving object, and those descriptions need

to be modified. In between bulk metals and single atoms there is a characteristic size that corresponds to a finite number of atoms where the density of electron states from continuous becomes discrete and the electrons are not free any more, but become localized (see Figure 1.2). At exactly this scale, that scale mentioned by Feynman in 1959, lies the subject of this thesis.

Kubo *et al.* [12] defined a criterion for when such transition, from continuous to discrete, occurs, *i.e.* when a system can be no longer considered classical. The electrons must be considered localized when the average energy distance between two levels is greater than their thermal energy. Considering the average spacing between two neighbouring energy levels, the transition occurs when:

$$\delta \approx \frac{E_F}{N} > k_B T \quad (1.1)$$

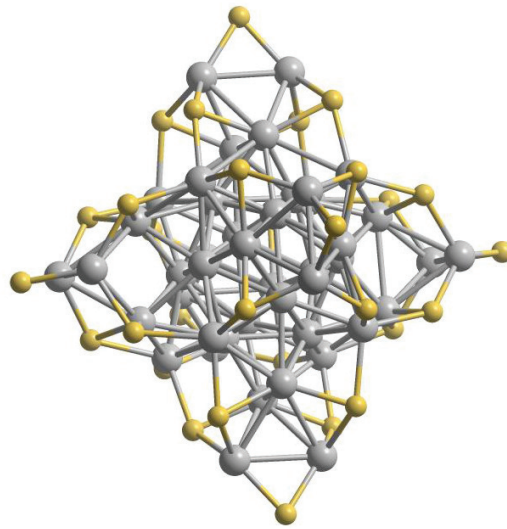


**Figure 1.1** – Cluster of  $Ag_{44}$ , composed by 44 silver atoms (grey balls) and 30 sulfur atoms (yellow balls)



where  $E_F$  is the Fermi energy,  $N$  is the number of valence electrons in the system,  $k_B$  is the Boltzmann constant and  $T$  is the temperature of the system. At room temperature  $k_B T = 25$  meV,  $E_F$  for a gold (Au) is 5.53 eV [13] and given that Au has mainly one valence atom coming from the  $6s^1$  shell, the transition occurs for  $N \approx 220$  atoms, that corresponds to a spherical gold nanoparticle (AuNP) of size smaller than 2 nm. An object of such dimension will be referred to as cluster or nanocluster (NC). This sub-2-nm range is of great interest because it embraces the field where thanks to "different laws we can expect to do different things" as Feynman said. The work of this thesis has been carried on a fluorinated silver (Ag) assembly composed of 44 Ag atoms, thus it has been entitled a cluster. As it will be shown, such cluster presents features characteristic of this group of nanomaterial.

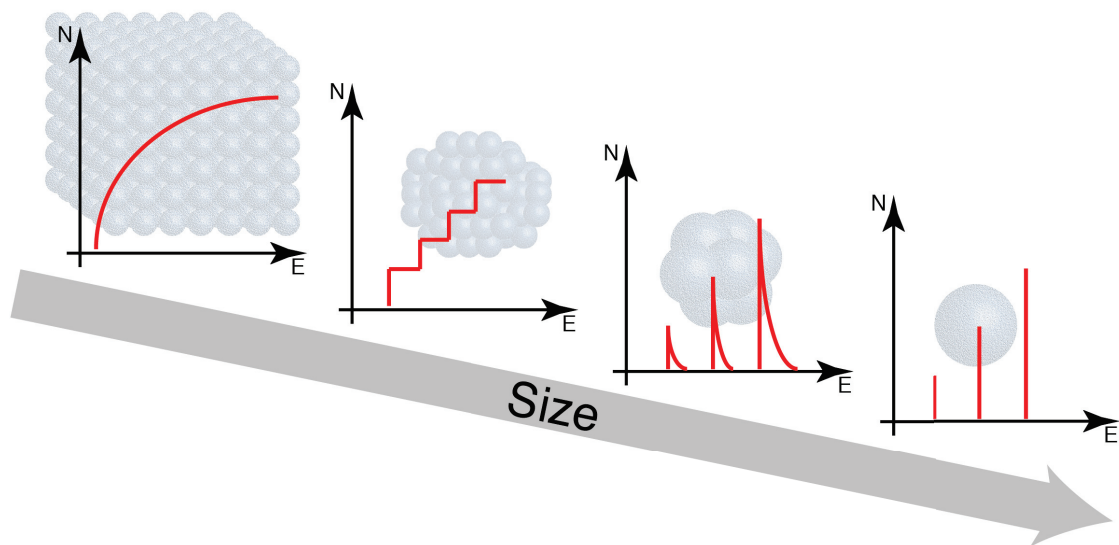


**Figure 1.2** – Density of states ( $N$ ) for bulk materials, nanoparticles, clusters or quantum dots, and single molecules. As the size shrinks, the density of states passes from being continuous to discrete, quantized. It is worth to mention that this is a continuous transition.

Already in 1997 Schaaff *et al.* [14] demonstrated that quantum size effects (quantum size effect (QSE)) come in play. The main challenge for observing these effects in metal clusters arises from the difficulty in controlling the growth of the clusters, the passivation of the surface and their size homogeneity. Schaaff and colleagues were able to isolated NC with a crystalline (or quasicrystalline) core of densely packed Au atoms [14], with size spanning from  $\approx 1.1$  nm ( $\approx 40$  atoms) to  $\approx 1.9$  nm ( $\approx 200$  atoms), protected by a monolayer of thiol adsorbates. In their work they summarised six characteristic properties of such NC: i) a crystalline (or quasicrystalline) core with near-ideal strength and no ductility-malleability; ii) stability at critical sizes corresponding to specific shell filling configurations, the so-called "magic numbers" [15]; iii) the highly reactive surface of the NC is passivated by a defined numbers of adsorbates without affecting the structure of the cluster itself; iv) discrete charge states; v) the conduction band being quantized; and lastly vi) the transport, optical, chemical and magnetic properties are different given the change in the electronic structure. Most of these properties will be

examined in details in this work in relation to the NC that this thesis deal with,  $\text{Ag}_{44}(\text{FTP})_{30}$ .

### 1.1 Thesis outline

This thesis is structured as follows:

- Chapter 2, firstly, introduces the reader to the field of metal nanoclusters, describing the synthetic progresses which led to the realisation of atomically precise and monodisperse NCs. The second part focuses on silver NCs and illustrates their most common characterisation techniques. An overview of the challenges and potential application is also illustrated.
- Chapter 3 describes the synthetic procedure for obtaining atomically precise  $\text{Ag}_{44}(\text{FTP})_{30}$  and how to crystallise this cluster. The second part deals with the characterisation method utilised in the course of this thesis, describing the techniques involved, the instruments used and the samples' fabrication.
- Chapter 4 illustrates the results obtained and is divided in three parts. The first part shows the optical properties of IBAN crystal; the second part presents the main findings of this thesis, which concern the electric properties of  $\text{Ag}_{44}(\text{FTP})_{30}$  crystals. The last part shows the single crystal XRD results obtained under different conditions, *i.e.* prior exposure to an electric field.
- Chapter 5 comments on the experimental observations made in Chapter 4 and provides an explanation.
- Chapter 6 contains the conclusions and illustrates the perspectives that this thesis hopes to have paved.

## 2 Introduction

### 2.1 Chapter outline

This chapter deals with the discovery of metal clusters and their synthetic progresses. The second part illustrates which are the theoretical approaches that describe the unique properties of metal NCs. The third part describes the characterization techniques employed in the study of this family of material. Lastly, an overview on the potential applications where metal NCs could be involved is presented.

### 2.2 Synthesis of noble metal nanoclusters

The reason why it took almost forty years [16] from the first talk of Feynman to observe QSE in metal NC was that all these non-classical effects fade away when the clusters are not homogeneous in size, or they disappear if their reactive surface is not protected, in other words if the clusters are not stable. In fact, due to their inherent instability Au nanoparticles and nanoclusters developed before Ag.

#### 2.2.1 Turkevich method

Historically, the first method used to synthesise AuNP was the so-called Turkevich method [17] utilizing phosphine ligand as a stabilizing agent [18–20]. Despite the limited stability due to weak Au-P bond [21], these were the only clusters with a size distribution narrow enough to show quantum effects. The preparation of such clusters was obtained through the reduction of diluted aqueous solution of  $\text{HAuCl}_4$  with citric acid ( $\text{C}_6\text{H}_8\text{O}_7$ ) or trisodium citrate ( $\text{Na}_3\text{C}_6\text{H}_5\text{O}_7$ ). The gold colloids obtained were stabilized with water soluble phosphine such as  $\text{P}(\text{m}-\text{C}_6\text{H}_4\text{SO}_3\text{Na}_3)_3$  [22]. The main drawback of using sulphonated phosphines is that they either hydrolyze in water or they are oxidized by air. Nonetheless with this method Chi *et al.* [18] were able to carry a first complete characterization of isolated 2.1 nm  $\text{Au}_{55}$  clusters. In order to form monolayer of this water soluble cluster, a substrate of atomically flat gold was

functionalized with cysteaminium chloride, making the gold surface positively charged. The substrate was then immersed in a solution of Milli-Q water and Au<sub>55</sub>, so that the negatively charged clusters could form a monolayer on the surface. STM measurements were carried out at room and low temperature (90 K). As can be seen in Figure 2.1 the current-voltage curves present a Coulomb staircase behavior, a trend which is more obvious at low temperature, indicating the presence of a single electron tunneling.

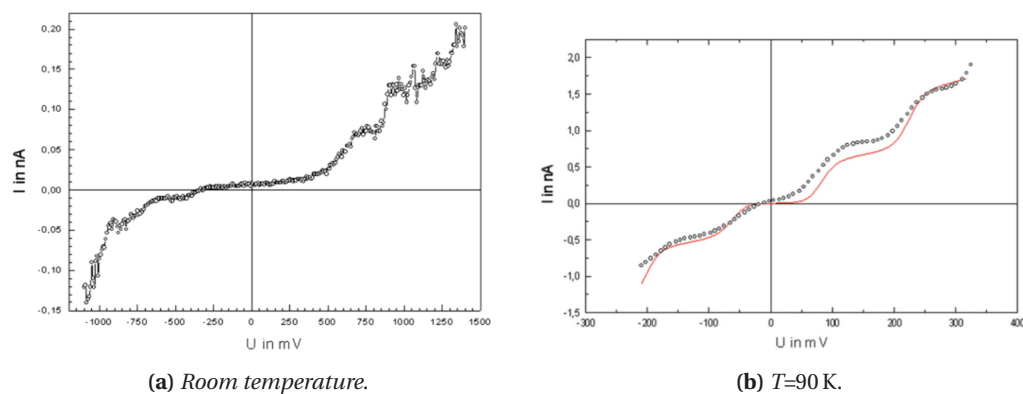


**Figure 2.1** – Examples of QSE in Au<sub>55</sub>: Single electron tunnelling at two different temperatures. Reprinted with permission from [18].

### 2.2.2 Brust method

In 1994 Brust *et al.* proposed an alternative method of NP/NC synthesis [23], substituting the weakly binding phosphine with thiolated groups. This method had at that time a great impact on the noble metal nanoparticle community, because it provided a facile route to the synthesis of highly stable NC. It consisted of a two-step synthesis: in the first step, Au<sup>+3</sup> was reduced to Au<sup>+1</sup> by a thiol ligand (HSR, where R indicates a generic functional group), in order to form an Au:SR polymer complex; subsequently, sodium borohydride (NaBH<sub>4</sub>) was added to reduce the polymer complex to Au<sup>0</sup> nanocrystals. The presence of the SR ligands had a double function: it halted the growth of the crystals and it prevented them from aggregating by providing a steric protection. Important parameters of the synthesis that also determined the final size of the NC were the Au to thiol ratio, the type of chemical functional group R, the temperature of the reaction and the amount of BH<sub>4</sub><sup>-</sup>. In their work Brust and colleagues chose a ratio BH<sub>4</sub><sup>-</sup> : Au : HSR = 3 : 2 : 0.2 and the synthesis was carried out at room temperature, leading to the formation of polydispersed >2 nm nanoparticles. In their following works the above mentioned parameters were tuned to produce a narrower distribution in size. On one hand this method provided for the first time stability to oxygen and temperature, reduced dispersity and controlled size, on the other hand though the nanocrystals were not small and monodisperse enough to exhibit QSE. The synthesis was modified by Schaaff [14], who was able to find the optimal BH<sub>4</sub><sup>-</sup>:Au:HSR ratio in order to obtain monodisperse clusters of different sizes. These NCs were obtained through fractional crystallisation and the use of mass spectrometry helped in discerning them: Schaaff found NCs with core masses of respectively

8k (1.1 nm,  $\approx 38$  atoms), 15k (1.3 nm,  $\approx 75$  atoms), 22k (1.5 nm,  $\approx 102$  atoms), and 29k (1.7 nm,  $\approx 144$  atoms), among which only the first serie showed QSE (see Figure 2.2).

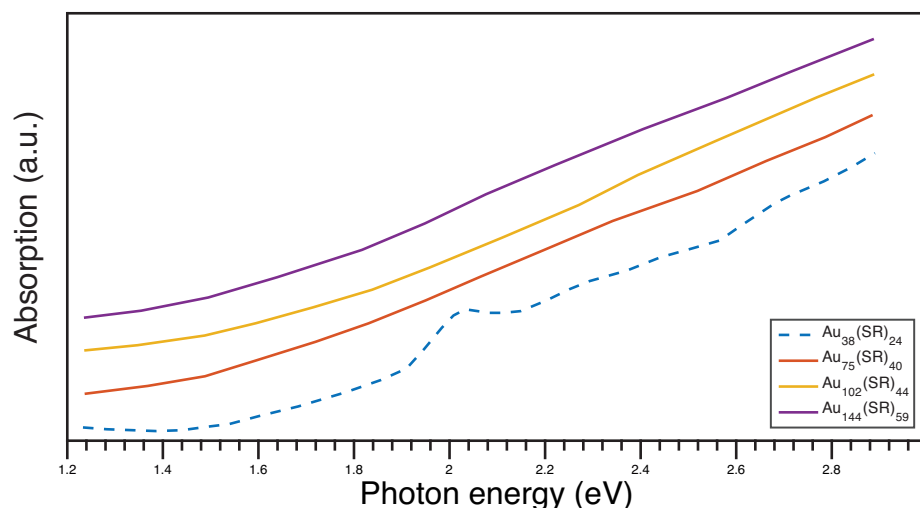


**Figure 2.2** – Absorption spectra of four different clusters isolated by Schaaff. The dotted line, corresponding to the smallest cluster, shows a characteristic quantum transition. Adapted with permission from [14].

Apart from the fractional crystallisation employed by Schaaf, other post-treatment methods have been successfully developed in order to obtain small NCs and with a narrow size distribution. For instance, Price [24] was able to separate a mixture of  $\text{Au}_{44}(\text{SR})_{28}$  and  $\text{Au}_{110}(\text{SR})_{62}$  because the former was more soluble in toluene than the latter; a second example of post-treatment is based on oxidative reduction or thiol etching [Tsunoyama:2009hb]: a mixture containing clusters of different sizes is heated with excess of thiols, which oxidatively etches large clusters breaking them down into smaller ones. Another successful separation method, although limited to water soluble NC, is represented by polyacrylamide gel-electrophoresis (PAGE) [25, 26], since the separation mechanism acts on both size and charge of the cluster. This technique separates the components of a mixture depending on their electrophoretic mobility. Since the optical properties of each cluster are dictated by its size, a small variation in the number of constituent atoms leads to a discernible variation in the absorption spectrum, so that in the typical ladder each component will be easily identified. An alternative method, demonstrated by Knoppe *et al.* in [27], is the so-called size exclusion chromatography (SEC), which separates mixture of species based on their size by passing them through a stationary phase. Knoppe in his work [27] used charge-neutral styrene divinylbenzene beads at low cross-linkage as stationary phase, in order to separate  $\text{Au}_{38}$  from  $\text{Au}_{40}$ : the latter species flows through the column more quickly than the former, so that in the elution  $\text{Au}_{38}$  has a longer retention time. The validity of this method has been verified by UV/VIS absorption and MALDI-MS [27].

### 2.2.3 Silver clusters synthesis

$\text{Ag}_{44}(\text{FTP})_{30}$  clusters represent the core of this thesis, so a wider section is now dedicated to their synthesis. In general, gold cluster chemistry does not differ too much from that of silver, so the above mentioned methodologies apply to silver as well. Nevertheless the reason why this field of research has opened up to silver only in the last ten years is that the aforementioned methods lacked in providing monodisperse and sufficiently small NCs. Preliminary work [28] made use of the Brust method to obtain Ag NC, even though they were not disperse. In 2009 for the first time Bakr [29] was able to synthesize monodisperse Ag NC. More precisely, he managed to isolate  $[\text{Ag}_{44}(\text{SR})_{30}]^{-4}$ : these clusters showed eight distinct and strongly absorbing peaks in the ultraviolet and visible spectrum, a peculiar characteristic for which they have been named intensely and broadly absorbing nanoparticles (IBAN).

Silver nitrate ( $\text{AgNO}_3$ ) or silver trifluoroacetate ( $\text{CF}_3\text{CO}_2\text{Ag}$ ) was dissolved in dimethylformamide (DMF), then 4-fluorothiophenol (4FTP), as primary choice of thioled ligand, was added, followed by the addition of the second solution of DMF and  $\text{NaBH}_4$ . At this point, the mixture turned brown and got darker as time goes, indicating the formation of silver silver nanoparticle (AgNP). After stirring, the solution turned yellow indicating that the AgNP had been oxidatively reduced into clusters, Milli-Q water was added and the reaction vessel was then moved to a freezer, where the NCs formed in a period of time comprised between three to seven days [29]. Different ligands were tested by Bakr in order to show that the charge density of sulfur affects the molecular orbits: the already mentioned 4FTP, but also 2-Fluorothiophenol, 3-Fluorothiophenol, mercaptobenzoic acid (MBA), methylthiophenol (MBDT), methylbenzothiophene (MBT) and mercaptomethylphenylmethanol (MPM). The absorption spectrum arising of 4FTP AgNC can be seen in Figure 2.3.

This synthesis procedure has been further refined and improved in [30], where  $\text{Ag}_{44}\text{MNBA}_{30}$  (mercaptanitrobenzoic acid (MNBA)) NCs were obtained atomically monodisperse, highly stable and in a high yield. The synthesis proceeds as follows: the disulfide bond of dithionitrobenzoic acid (DTNBA) is cleaved in an aqueous solution of  $\text{NaOH}$  resulting in MNBA. An aqueous solution of silver nitrate is added and the change in colour obtained has to be attributed to the formation of Ag-S complex. The mixture is subsequently reduced through the introduction of  $\text{NaBH}_4$ . The solution is repeatedly purified by precipitation with methanol. Moreover, Prof. Bakr's group was able to perform a complete ligand exchange, substituting MNBA with 4FTP [31]. The substitution is done by adding the desired thiol, together with tetraphenylphosphonium bromide (TPPB). The ligand exchange occurs within seconds and it involves more than 94% (molar ratio) of the original Ag clusters (see Figure 2.4).

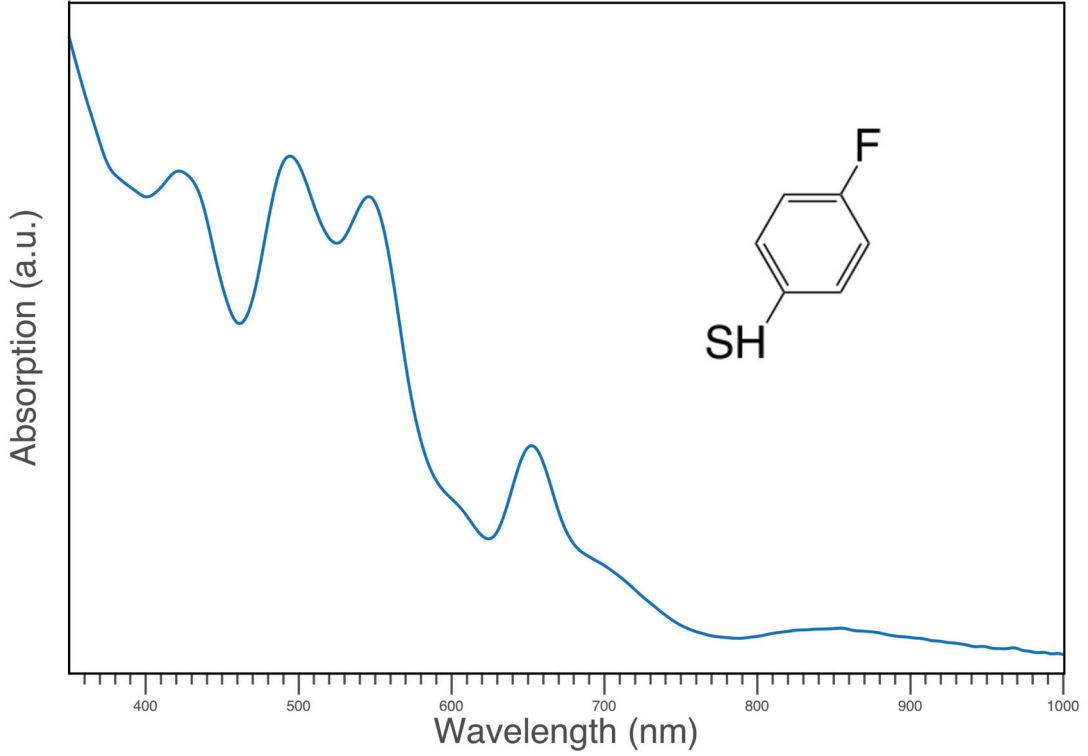


**Figure 2.3** – Absorption spectrum of silver NC protected with 4FTP and its characteristic absorption peaks.

## 2.3 Clusters stability: Jellium model and magic numbers

### 2.3.1 The Jellium model

As mentioned above, the electronic and optical properties of metal nanoparticles are described by the Drude-Lorenz and Mie theories, but they fail when the size of the metallic object approaches the quantum limit. A quantum model that has encountered success in describing the physical properties of metal NC, is the so-called Jellium model, or uniform electron gas model [15, 32, 33]. This many-body problem model treats the electron-electron interaction rigorously, and considers the positive atoms as uniformly distributed in space [34]. The hamiltonian of such system is thus composed of three terms: one for the electrons, one for the positive background and one for the interaction of the electrons with the background:

$$\hat{H} = \hat{H}_{el} + \hat{H}_{back} + \hat{H}_{el+back} \quad (2.1)$$

where  $\hat{H}_{el}$  contains a kinetic and an interacting electron term,  $\hat{H}_{back}$  is the electrostatic interaction of the positive atoms between themselves, and  $\hat{H}_{el+back}$  is the electron-atom interaction. The substitution of the detailed ionic structure with a positive background does not affect the properties of the NCs. This approximation leads to an easier calculation of the

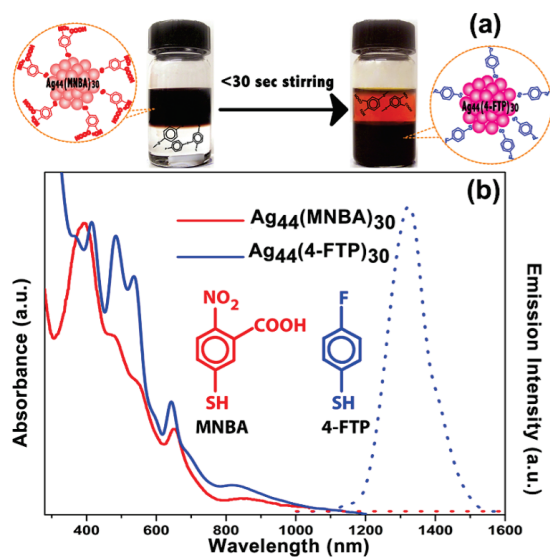


Figure 2.4 – Ligand exchange procedure. Reprinted with permission of [31]

electronic structure, which can be done in a classical way, *i.e.* self-consistently [34], using a spherically symmetric Jellium potential that yields the right shell closing numbers in most cases (see Figure 2.5), or by using semiempirical parameters that account for the deformation of the single particle potential [35]. The former is largely sufficient to explain the stability of fully closed shell clusters. A spherically symmetric potential gives origin to a spherical shell structure because of its symmetry, where the valence electrons fill the degenerate energy levels starting from the lowest. When the electron filling is such that a shell is closed, the cluster exhibits an exceptional stability. As de Heer calculated in the case of sodium [35], when an extra atom is added, the cluster valence electron will occupy a state considerably higher in energy, and hence the stability of the cluster is reduced [36].

### 2.3.2 Superatom theory and magic numbers

The superatom electronic theory [35] tries to find an explanation for the stability of a discrete set of NCs. Analogously to noble gases, which according to the atomic theory are stable and chemically inert because of their closed electronic shell, valence electrons can be transferred to thiolated ligands or phosphine groups, restoring the noble-gas electronic configuration in metal nanoparticles and NCs. This octet-atom analogy has been successful in predicting the stability [37] and chemical nature of metal NCs, explaining the mass abundance of uncoordinated metallic clusters [15], metallic and gaseous metallic clusters coordinated to a small number of bonds [38–40], and metalloid gallium based clusters [41]. In this analogy, NCs can be seen as atoms, whose free electrons ( $5s$  for Ag and  $6s$  for Au) are localized and follow the same filling rule of atoms, the aufbau principle, *i.e.* electrons must fill the lowest energy level. Using the azimuthal quantum numbers to fill the superatomic orbitals, Häkkinen [35] found the shell filling for ligands protected NC to be  $1s^2 | 1p^6 | 1d^{10} | 2s^2 1f^{14} | 2p^6 1g^{18} | 2d^{10} 3s^2 1h^{22}$ ,



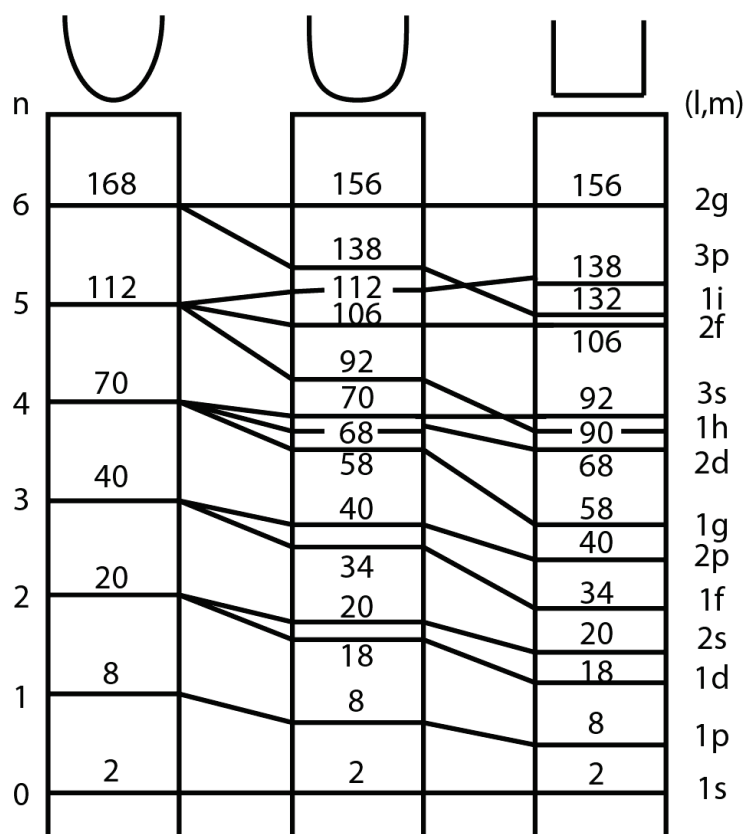


**Figure 2.5** – Shell closing numbers for three different mean field potentials. Reprinted figure with permission from Walt A de Heer, Reviews of Modern Physics, 65, 611–676, 1993. Copyright (2016) by the American Physical Society.

where  $s$ ,  $p$ ,  $d$ ,  $f$ ,  $g$  and  $h$  denote the angular-momentum quantum number. These delocalized orbitals are derived from the  $6s$  atomic orbitals [42, 43] for Au ( $5s$  for Ag). Exceptional stability is found for a total number of electron count of  $n^* = 2, 8, 18, 34, 58, 92, 138 \dots$  corresponding to the number of electrons needed for full shell closure in an anharmonic mean-field potential (depending on the mean-field potential, 20 and 40 electrons can also account for a stable cluster [15], see Figure 2.5). These numbers originate from the presence of the stabilizing ligands, which can withdraw or localize electron in a covalent bond, or may be attached as weak Lewis (L) base. For instance, for an arylthiolated AgNC expressed as  $[\text{Ag}_N\text{X}_M\text{L}_S]^z$ , the requirement for full shell closure is:

$$n^* = Nv_a - M - z \quad (2.2)$$

where  $n^*$  is the electron count for the superatom complex,  $N$  is the number of metal atoms,  $v_a$  is the valence of the metal atoms (one electron for Ag or Au),  $M$  is the number of ligands, and  $z$  is the overall charge. If we take  $[\text{Ag}_{44}(\text{SR})_{30}]^{-4}$  as an example, we find out that it has  $Nv_a - M - z = 44 - 30 - (-4) = 18$  electrons, showing that this NC has the electronic shell fully closed, which is the reason for its extraordinary stability. The same rule applies to

$\text{Au}_{102}(\text{p-MBA})_{44}$ , electron count of 58, and to  $[\text{Au}_{25}(\text{SR})_{18}]^{-1}$ , with a total valence of 8.

## 2.4 Characterization

As we have already seen, cluster properties strongly depend upon the homogeneity and dimension of the clusters themselves. Being able to properly characterize them is thus crucial for our understanding of the parameters that need to be controlled or changed in order to obtain the desired properties. A review of the main techniques is presented here.

### 2.4.1 Nuclear magnetic resonance

Among the other characterisation tools, nuclear magnetic resonance (NMR) provides insights into the metal ligands interface and the surrounding environment of the clusters. For instance, in the work of Abdul Halim [30], by comparing the NMR spectra of the bare ligands, namely MNBA, and those of the NC, they were able to determine the occurrence of a successful anchorage via the upfield shift of the ligand peaks, that occurred because of the different chemical environment. Additionally, it has been shown [44] that the number of peaks for the R group relates to the number of symmetry environments of the sulfur group. Further analysis by the group of Prof. Martins [45], made use of diffusion-ordered NMR spectroscopy (DOSY) and nuclear Overhauser effect NMR spectroscopy (NOESY), two dimensional NMR spectra, to discriminate between anchored ligands from free ligands.

### 2.4.2 Mass spectrometry

For many years mass spectrometry (MS) has represented the main characterization tool for NC. This analytical technique [46] is based on the ionization of chemical species and on the following collection based on their mass to charge ratio. This separation is realized in three components of the instrument [47]: i) an ionizer, which generates sample ions; ii) an analyzer, which sorts the ions based on their mass to charge ratio; and lastly iii) a detector, which measures the quantity of each ion present. The ionization can be realized in different ways, among which the so-called soft-ionization techniques, such as matrix-assisted laser desorption ionization (MALDI) and electrospray ionization (ESI), have extend the field of use of MS to soft and less stable materials, such as proteins, peptides and also NC, without causing degradation. In MALDI the sample is mixed in a matrix of crystallised low molecular weight molecules, strongly absorbing the wavelength of the pulsed laser that is used to irradiated the matrix and to trigger the ionization. The choice of the matrix is thus crucial for the outcome of the experiment. Frequently MALDI MS are used in conjunction with a time of flight (TOF) mass spectrometer, where ions are accelerated in a tube, they can be reflected by a reflectron in order to double their path, and finally they hit on a sensor, which measures their time of flight, determining their masses and abundances. MALDI-TOF has been successfully applied to determine the size of  $\text{Au}_{25}$  [48] and of  $\text{Au}_{38}$  [49], where they demonstrated by successive

thiol etching steps the sharpening of the peak corresponding to the mentioned cluster.

The other MS configuration that has been widely used is the ESI, where a solution containing the analyte to be studied is dispersed through electrospray. This is realized by applying high voltage to the solution, turning into an aerosol. In the work of Harkness *et al.* [50], ESI-MS was used to discern two different IBANs as monodisperse NCs of  $\text{Ag}_{44}(\text{SR})_{30}^{4-}$ . The main advantage of this MS tool is that it reduces the fragmentation of clusters because the ionization occurs in solution. The optimization of the ESI-MS parameters, *i.e.* collisional energy, extraction cone voltage and sampling cone voltage, has led this technique to be the best MS candidate for clusters determination, especially for AgNC, where fragmentation is a big limitation for MALDI [51–53].

### 2.4.3 Analytical ultracentrifugation

Another well established technique for nanoparticles size separation [54] is analytical ultracentrifugation (AUC). It allows a complete characterization of size, density and molecular weight of the species dissolved in a solution. In AUC a high speed centrifuge is equipped with one or more optical detection elements (UV/VIS) that during the fractionation measure the concentration profile with respect to radial distance from the centre of the rotor. In a following step this concentration value is modelled to retrieve information upon the sedimentation and diffusion coefficient distribution. In the field of NC, AUC has been used both as a post treatment tool to reduce the size distribution of the synthesized clusters, and as a characterization method to determine sizes, dispersion and molecular weight [29, 30, 50]. Some precautions is needed in the preparation of samples. For instance, density gradient should be used, as demonstrated in the work of Bakr [29], in order to stabilize the solution against the detrimental effect of remixing due to convection.

### 2.4.4 Absorption spectroscopy

The optical properties of metal nano-objects, considering together clusters and nanoparticles, depend on their sizes. The optical absorption of spherical metallic objects was derived by Mie in 1908 [55] as a solution of the Maxwell equations. A detailed treatment was later carried on by Van Hulst [56], where the optical response of noble metal nanoparticles was attributed to charge oscillations, known as localized surface plasmons. When the size of these metal nanoparticles further decreases, this classical treatment fails and the absorption is ruled by the modification of the energetic landscape of the cluster. The transition from plasmon-like to molecular-like absorption has been calculated and verified in the work of Aikens, where the spectral evolution of AgNCs is studied as it changes with increasing number of silver atoms  $\text{Ag}_n$  [57]. In general, the UV/VIS absorption of atomically precise superatoms can provide preliminary information about the size composition, as confirmed by Dass and colleagues [Dass:2011cs]. The work of Bakr [29] was the first to report the presence of non-plasmonic peaks in the absorption spectra of silver NCs.

### 2.4.5 Electron microscopies

Electron microscopies techniques are employed in transmission electron microscope (TEM) and scanning electron microscope (SEM) as powerful tools for the characterization of nanomaterials. In the nanoparticle field, the high resolution transmission electron microscope (HRTEM) is a standard for NP size determination, but unfortunately in the case of NC this technique cannot be used, because the high energy electron beam damages the organic ligands and degrades the clusters [58]. Moreover, the low contrast of the smaller clusters introduces error in the statistics of size determination. Nonetheless others [Tsunoyama:2009hb, 30, 44, 48] have previously made use of TEM as complementary technique to MS to estimate the dispersion of size in a sample. Mainly however, SEM has been used to visualize crystals of those clusters that can be crystallised and to determine the composition when used in conjunction with energy-dispersive x-ray spectroscopy (EDX) [59].

### 2.4.6 X-Ray

The most precise technique for cluster characterization is x-ray diffraction (XRD), more specifically single crystal XRD: it allows a precise determination of the clusters chemical composition, it displays how ligands arrange on the metal atoms and how they cap the clusters. Unfortunately XRD is limited to those clusters that can be crystallised and such a process requires highly monodispersed and clean samples. The group of Kornberg [60] in 2007 was able to crystallise and determine the exact structure of  $\text{Au}_{102}(\text{p-MBA})_{44}$ . In this work information on the structure of the nanocluster was given with a resolution of 1.1 Å and the proof of the existence of  $\text{Au}_{102}(\text{p-MBA})_{44}$  was important in confirming all the hypotheses on cluster composition and geometry that molecular dynamics simulation had predicted [61, 62]. Later on  $\text{Au}_{25}(\text{SR})_{18}$  was fully resolved by the group of Murray [63] and Jin [64]. The complete determination of a silver cluster took longer, because as described above, the synthesis for obtaining atomically dispersed silver clusters was harder to achieve and the final product less stable than its gold counterpart. It was not until 2013, that the group of Prof. Zheng [65] crystallised  $\text{Ag}_{44}(\text{SR})_{30}$  and  $\text{Au}_{12}\text{Ag}_{32}(\text{SR})_{30}$ , while Prof. Bigioni [66] succeeded in the crystallisation of  $\text{Ag}_{44}(\text{p-MBA})_{32}$ . The knowledge of the exact position of each atom of the cluster provides, as demonstrated in [66] and in [67], an ideal platform for molecular dynamic and *ab-initio* simulations, because it gives realistic initial conditions that better allow to explore the novel properties of these materials and rationalize the observed behaviors.

## 2.5 Challenges

Nowadays we have at disposal a plethora of nanoclusters, but despite the progress made in synthesis of monodisperse and clean samples, little has been done in terms of application or usability of these clusters. The understanding of this family of new materials has really progressed, but the capability of processing them is still very limited. This section deals with the main properties that can be encountered and controlled in NC and how they can be exploited

for sensors, catalysis and other applications.

### 2.5.1 Optical properties and circular dichroism

The optical properties of NCs are dictated by their size and formation of discrete energy levels, and they can be controlled by an appropriate choice of metal atoms, number of atoms, but also by a careful selection stabilizing ligands. Another possibility for controlling the optical properties comes from the fact that, while single constituents are achiral, the NCs can be intrinsically chiral [68–70] or the chirality can be transferred from the ligand to the metal core [71, 72]. This property arises from the assembly in three dimensions of the metal atoms into "asymmetric superatoms" or "superatom complexes" [68, 73, 74]. Knoppe and colleagues were able to isolate the enantiomers of  $\text{Au}_{38}(\text{2-PET})_{24}$ , that together with  $\text{Au}_{40}(\text{SR})_{24}$ , represents one of the intrinsically chiral NCs, although being racemic. In his work he showed how the introduction of a chiral ligand led to a stabilization of one of the two diastereomers. Similarly, the same group showed that it is also possible to preserve the chiral properties of the metal core, again  $\text{Au}_{38}(\text{SR})_{24}$ , even with achiral ligands [75]. As described in the work of Guerrero [69], the origin of chirality at the nanoscale can arise for different reasons: the NC or NP can be intrinsically chiral as in the case of the NCs of Knoppe [68]; otherwise chiral ligands, if chosen properly, can induce optical activity in achiral cores, through vicinal effects or through a chiral electrostatic field; lastly, an originally achiral core can modify and deform its surface in the process of adsorbing a chiral ligand, resulting in a chiral footprint [70, 76]. An example of the second case is represented by the work of Zeng [72], where  $\text{Au}_{28}(\text{TBBT})_{20}$  (4-tert-butylbenzenethiolate (TBBT)) was crystallised and the unit cell of such crystal contained a pair of enantiomers. Lastly, the group of Prof. Bürgi in 2009 induced chirality in  $\text{Au}_{25}$  [76] through a ligand exchange process that only partially substituted the original ligand shell, still presenting chiral response, even in smaller clusters [77].

The development and characterization of chiral AgNCs is delayed compared to their gold counterpart. Much effort has been made, but at the moment, to our knowledge, no atomically dispersed silver cluster has been found showing chiral properties. However there exist several publications of unidentified silver NC, which demonstrate a chiral response [78–81]. Noticeably the last two works [80, 81] have made use of DNA to stabilize the clusters and transfer the chiral information into the metallic core, but none of them was able to isolate and identify a monodisperse silver cluster.

### 2.5.2 Nanoclusters for catalysis

Another field where NCs have attracted interest is catalysis. The difficulties in using metal NCs as catalyst consist in the right choice of ligands, since they must hinder the aggregation of NCs yet allow small molecules or enzymes to reach the surface and trigger reactions [82]. The attention they have attracted arises also from the fact that the ligands play a role as selective elements in catalysis [83–85]. There are two major classes of catalyst: it can either

be homogeneous or heterogeneous. While the former is in the same phase as the reactants, the latter is a two-phase system. In this respect NCs establish a convergence of these two approaches, because the solid NC phase is actually a colloidal phase of the same size as the reactants [86]. Different examples of NCs as catalysts have been demonstrated, both for gold [82, 84–88] and silver [89–91]. Among all these publications there is a common underlying principle that has driven research and that represents a starting point for the design of new NCs catalysts, which is related to the NC and the ligand sizes: as the size of the NC decreases, the surface-to-volume ratio increases for smaller particles, and as a result it tilts the stabilizing ligands apart, opening access points for the reactants or enzymes. Similarly, bulky ligands will not pack as efficiently as smaller ligands, leaving behind access points that would not be available in the case of densely packed small ligands. This has been shown both for gold [85] and for silver [90]. In the first case, three different size clusters were synthesized and stabilized with calix[4]arene ligands. The researchers measured the surface that remains accessible through a chemisorbed probe molecule, 2-naphthalenethiol (2NT). Unbound 2NT molecules fluoresce, but the fluorescence is quenched when bound to a gold cluster. A decrease in fluorescence therefore showed a successful binding event on the gold surface. For the smallest clusters  $\text{Au}_{11}$  25% of the surface was accessible for the 2NT molecules, a much larger value compared to 6.3% and 1.2% for the 1.1 nm and 1.9 nm clusters respectively. In the case of silver NCs, Lu and colleagues [90] showed that  $\text{Ag}_7$  0.7 nm clusters exhibit a better electrocatalytic activity than larger AgNCs.

### 2.5.3 Magnetic properties

Gold and silver are known to be diamagnetic in bulk form because, despite the paramagnetism of the conduction electrons, the orbital and ionic diamagnetic contributions prevail [92, 93]. Surprisingly though, when these atoms are grouped into clusters, they can be magnetic [93, 94]. Several others publications [95–98] have demonstrated that Au and AgNCs can possess permanent magnetization, which arises either because of symmetry reasons [94] or from surface effects, where the spin polarization mechanism is given by the charge transfer from the organic capping layer of the NC and the metal core [95, 96]. In both cases, the opportunity offered by making use of magnetic properties in this family of new materials would be beneficial in many different ways, from magnetic separation of cells to therapeutic drug delivery, from hyperthermic treatment of tumoral cells to new contrast enhancement agents for magnetic resonance imaging.

## 2.6 Collective properties

Collective properties is the reason why NCs are considered to be among the most interesting materials in nanotechnology. It is related to their molecular-framework characteristics. In two recent works, the groups of Prof. Landmann and Prof. Bigioni were able to crystallise for the first time silver NCs [66], namely  $\text{Na}_4\text{Ag}_{44}(\text{p-MBA})_{30}$ , the structure of which was fully

determined by single crystal X-ray. This result was impressive because of the complexity of the resulting unit cell that contained an outstanding number of atoms. The monolayer protected silver NC was resolved and was found to be a keplerate solid composed of a empty icosahedron of silver atoms  $\text{Ag}_{12}$ , enclosed within a silver dodecahedron cage  $\text{Ag}_{20}$ . The cage was then capped with six  $\text{Ag}_2\text{S}_5$  motifs that stabilize the overall clusters (see Figure 2.6)

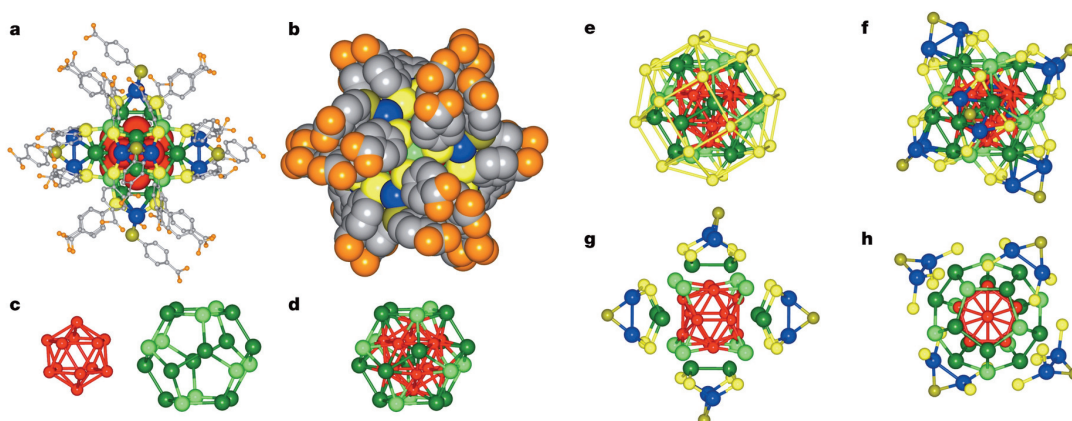


**Figure 2.6** – **a**, Complete cluster structure showing silver core and p-MBA ligands. **b**, Space-filling view down a three-fold axis. **c**, The  $\text{Ag}_{32}$  excavated-dodecahedral core consists of an inner 12-atom (hollow) icosahedron (red) whose atoms do not contact sulphur, encapsulated by a 20-atom dodecahedron (green). **d**, The complete  $\text{Ag}_{32}$  excavated-dodecahedral core. **e**, Sulphur atoms (yellow) are arranged in a slightly distorted rhombicuboctahedron with S atoms in the triangular faces coordinating to the light-green Ag atoms of the 20-atom dodecahedron. **f**, Six faces of the rhombicuboctahedron are capped with an  $\text{Ag}_2\text{S}$  unit. **g**, Two Ag atoms (dark green) on each face could be excised from the cluster to create  $\text{Ag}_4\text{S}_5$  capping mount structures, leaving a cubic  $\text{Ag}_{20}^{2+}$  core. **h**, An alternative  $\text{Ag}_2\text{S}_5$  capping structure. Colour scheme: grey, carbon; orange, oxygen; blue, exterior silver atoms in the mounts; gold, bridging sulphur atoms in the mounts. Adapted with permission from [66].

This result was crucial in determining the optical and electronic properties of this cluster from density functional theory (DFT) calculations, because knowing the exact position of each atom allows for a more precise prediction of the above mentioned properties. In a follow up work [67], they made use of the resolved structure of  $\text{Ag}_{44}$  to calculate the molecular level mechanical response of the crystal to compressive stimuli. The outcome was a complex molecular solid, where the building blocks, *i.e.* the  $\text{Ag}_{44}$  clusters, are held together by a network of hydrogen bonds that act as structure directing synthons [99], and that show a cooperative response to external stimuli. They observed that when compressed, the material showed softening and the NCs underwent chiral rotations, exactly like gears, or chiral honeycomb [100], where the bent p-MBA ligands act as torque-transfer relays and the hydrogen bonds as "molecular hinges" [67]. The novelty of this work consists in having found that these molecular materials show tunable collective behaviours, that have their origin in the coupling between their constituents. This is particularly interesting for the work developed in this thesis where the electric properties investigated seem to have similar origin, or at least, similar collective behaviours.





## 3 Experimental section

### 3.1 Chapter outline

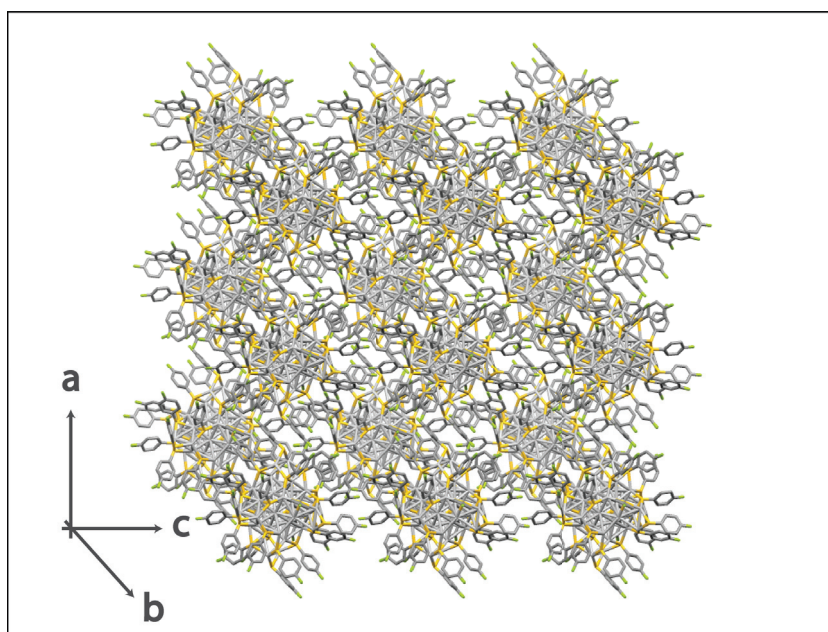


**Figure 3.1** – Resolved XRD crystal structure of Ag<sub>44</sub>(FTP)<sub>30</sub>

In this chapter I discuss in detail the synthetic routes and the crystallisation procedure followed in the course of this work in order to obtain high quality crystals. In Section 3.2, the reasons behind non-triviality of synthesis and crystallisation are discussed: material complexity, stability and size dispersion.

This chapter provides the recipes used and the procedures that led to formation of Ag<sub>44</sub>(FTP)<sub>30</sub> crystals, which possess a triclinic unit cell composed of an astounding number of 588 atoms. Single crystal XRD results are also reported. The second part of this chapter deals with the characterization techniques that have been employed for studying the Ag NCs.

### 3.2 Synthesis

The experiments were performed primarily on crystals of  $\text{Ag}_{44}(\text{FTP})_{30}$ . This cluster was first synthesized by Osman Bakr in 2009 [29] and since then the synthesis procedure has been improved [31], resulting in better yield and longer stability. Two synthesis procedures were employed for the crystallisation of  $\text{Ag}_{44}(\text{FTP})_{30}$  and both led to the same level of purity and uniform dispersity, fundamental prerequisites for the realization of high quality crystals.

**Synthetic route 1** The first synthetic route consists in a modified one-phase Brust-Schiffin method [30, 101, 102] followed by a ligand exchange procedure [31]. The first part is composed of two steps, the preparation of the capping ligand, MNBA, and the reduction of silver salt. For the former DTNBA (9.91 mg, 25 mmol) was stirred in aq. NaOH (20 mL, 1 mol). This reaction leads to the cleavage of the disulfide bond and the change in colour of the solution, from orange to dark yellow, indicates the formation of the desired MNBA. The second step of the first part was realized by adding the obtained MNBA to an aqueous solution of  $\text{AgNO}_3$  (8.5 mg, 50 mmol, 5 mL) to form Ag–S complexes. The new mixture looked greenish yellow and was reduced by adding a fresh solution of 2 mL  $\text{NaBH}_4$  (1 mg). The mixture was stirred for four hours and changed colour from dark brown to dark red. The final solution, containing  $\text{Ag}_{44}(\text{MNBA})_{30}$ , was purified by iterative precipitation with a solution of methanol and water (1:1), followed by centrifugation (9 krpm) and decantation of the supernatant. The purified  $\text{Ag}_{44}(\text{MNBA})_{30}$  were redispersed in NaOH at a concentration of  $4.57 \text{ mg mL}^{-1}$ . The ligand exchange was performed by adding 1 mL of the obtained cluster solution to dichloromethane (DCM) (1 mL) and ethanol (1 mL) containing 4FTP (0.013 mmol) and TPPB (0.007 mmol). The solution turned dark, indicating the occurrence of the phase transfer, while aqueous phase changed into clear yellow indicating the presence of free MNBA ligands. The phase-exchanged solution was decanted and purified by centrifugation with the addition of ethanol. After having iterated the cleaning procedure five times, the NCs were left to dry under vacuum overnight and would be redispersed in DCM or acetone at the high concentration of  $10 \text{ mg mL}^{-1}$  and then used for crystallisation.

**Synthetic route 2** The second synthesis was taken from the work of Yang [65], where six different silver and silver-alloy clusters were synthesized, crystallised and their structures were determined through single crystal X-ray experiments. As opposed to synthetic technique 1, this is a two-phase method. Silver nitrate  $\text{AgNO}_3$  (10 mg) was dissolved in a solution of methanol and DCM. The mixture was then cooled and kept at  $0^\circ\text{C}$  and  $10 \mu\text{g}$  of 4FTP, followed by the addition of the counterions 12 mg of TPPB. The solution was stirred for twenty minutes, after which 1 mL aq  $\text{NaBH}_4$  ( $45 \text{ mg mL}^{-1}$ ) was added together with  $50 \mu\text{L}$  of triethylamine ( $\text{N}(\text{CH}_2\text{CH}_3)_3$ ) under vigorous stirring. The solution was then kept for twelve hours at  $0^\circ\text{C}$ , then the aqueous phase was removed and the obtained solution washed several times.

## 3.3 Crystallisation of the silver nanoclusters

Since the first successful synthesis [29],  $\text{Ag}_{44}(\text{FTP})_{30}$  appeared immediately as a promising candidate for the realization of devices based on the properties that only metal clusters exhibit, such as semiconducting behaviour, remarkable broadband and multi-peak absorption [29, 50] and light harvesting due to their long lived charge-separated states [103]. Unfortunately long term stability represented an obstacle to the development of applications. The crystallisation of this and other silver NCs [65, 66] has rekindled the interest for this material. This section describes the crystallisation techniques employed to yield high quality crystals of  $\text{Ag}_{44}(\text{FTP})_{30}$ .

### 3.3.1 Methods

Key factors for the crystallisation of silver NCs are the cleanliness and monodispersity of the starting solution. Both the synthesis procedure mentioned above are capable of delivering clean and monodisperse solution of  $\text{Ag}_{44}(\text{FTP})_{30}$ , as demonstrated by MS and other techniques [31, 50, 65]. Starting from a dry powder of  $\text{Ag}_{44}(\text{FTP})_{30}$ , a saturated solution was obtained dissolving the NCs in DCM. Concentration ranging from 5 to 10  $\text{mg mL}^{-1}$  yielded similar results. Crystallisation is kinetically hindered, thus optimal conditions are found when the solution is supersaturated [104, 105]. In this study NC crystals were obtained following two techniques, and while both led to high quality crystals, the final size of the crystals and their environmental stability changed depending on which technique was used.

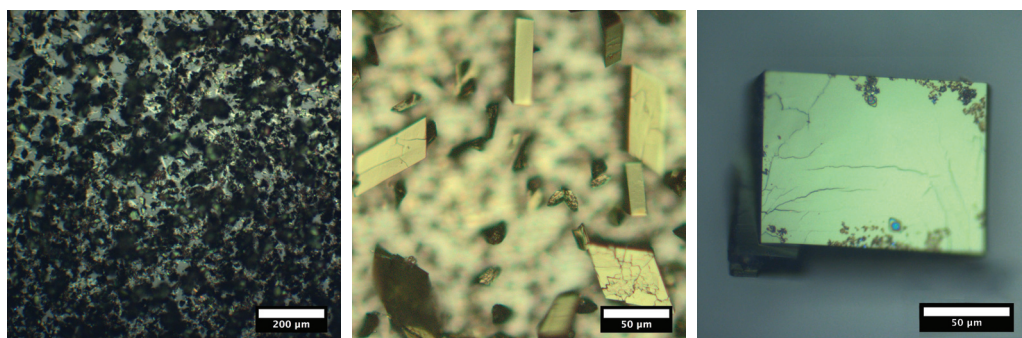
#### Vapour-vapour diffusion

Crystals of  $\text{Ag}_{44}(\text{FTP})_{30}$  were obtained through a vapour-vapour diffusion method [106], where two solvents are required, one that dissolves the clusters and the other, the so-called antisolvent, that does not. Among the possible solvent-antisolvent couples dichloromethane-hexane and acetone-hexane have been chosen and used. The crystallisation of the clusters solution occurred on top of a glass or silicon surface.

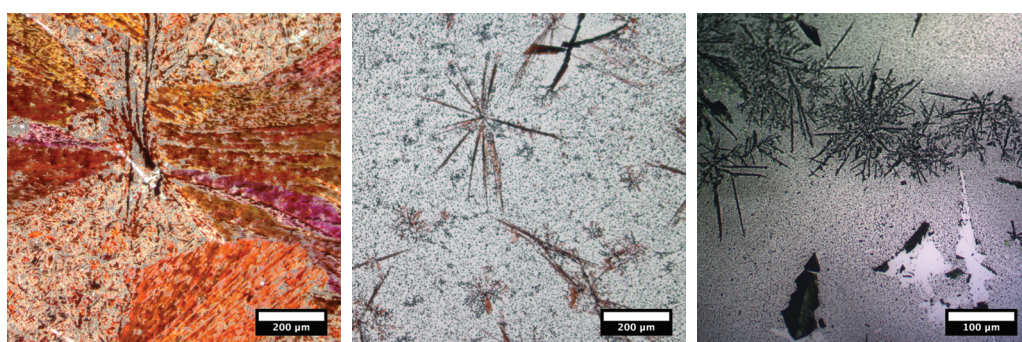
**Substrate preparation** Substrates were cut from a four inch Float glass wafer purchased from Guinchart (Optical glass, Switzerland. Composition:  $\text{SiO}_2$  70.8%,  $\text{Na}_2\text{O}$  13.9%,  $\text{K}_2\text{O}$  0.4%,  $\text{CaO}$  8.4%,  $\text{MgO}$  4.4%,  $\text{Al}_2\text{O}_3$  1.5%,  $\text{Fe}_2\text{O}_3$  0.08%,  $\text{SO}_3$  0.3%) into squares of  $12 \times 12 \text{ mm}^2$ . Subsequently, the squares were rinsed with acetone, dried, ozone cleaned for ten minutes and rinsed again in acetone in order to remove any organic contaminants. Each square was wiped with a residue-free wipe, then rinsed and sonicated five minutes in acetone, ethanol and isopropyl alcohol successively. At each step the squares were nitrogen blow dried. Lastly, prior to dispersion of the solution, each substrate was exposed to  $\text{O}_2$  plasma.

**Crystals preparation 1** 100  $\mu\text{L}$  of saturated  $\text{Ag}_{44}(\text{FTP})_{30}$  solution was drop-casted on the clean glass substrate placed on top of a teflon cube in a 25 mL vial. Subsequently, 30 to 50  $\mu\text{L}$  of

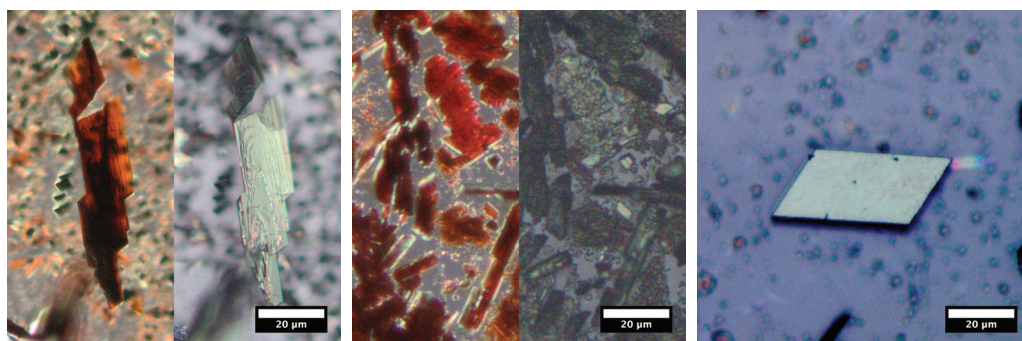
### Chapter 3. Experimental section



(a) Uncrystallised sample with small crystals (b) Example of cracked and good crystals (c) Example of acetone-hexane crystallisation



(d) Example of a film-like crystalline formation (e) Dendritic formation of different thickness (f) Dendritic and geminated crystalline structures



(g) Epi and diascopic image of a crystal (h) Epi and diascopic image of crystals and aggregates (i) Example of an ideal crystal produced from DCM-hexane

**Figure 3.2** – Different examples of possible crystallisation outcomes. For these images I used an Olympus BX-61 with either diascopic or episcopic illumination. The microscope was modified in order to perform microspectroscopy (see Appendix A)

antisolvent were added to the bottom of the teflon cube and the vial was closed and sealed with parafilm. The crystallisation occurred overnight in an environment free of vibrations which would otherwise be detrimental for the formation of the crystals (see figure 3.3b). Compared to crystal preparation 2 (see below), this technique produced smaller crystals. Since the amount of solubilizing solvent was small compared the to volume of the sealed environment,

### 3.3. Crystallisation of the silver nanoclusters

it evaporated so quickly that it prevented the crystals from growing larger. As it can be seen in Figure 3.3, the purity of the starting solution determined the quality and cleanliness of the final product: a clean starting solution resulted in a free of residue crystal, while some impurity caused the accumulation and aggregation of uncrystallised product.

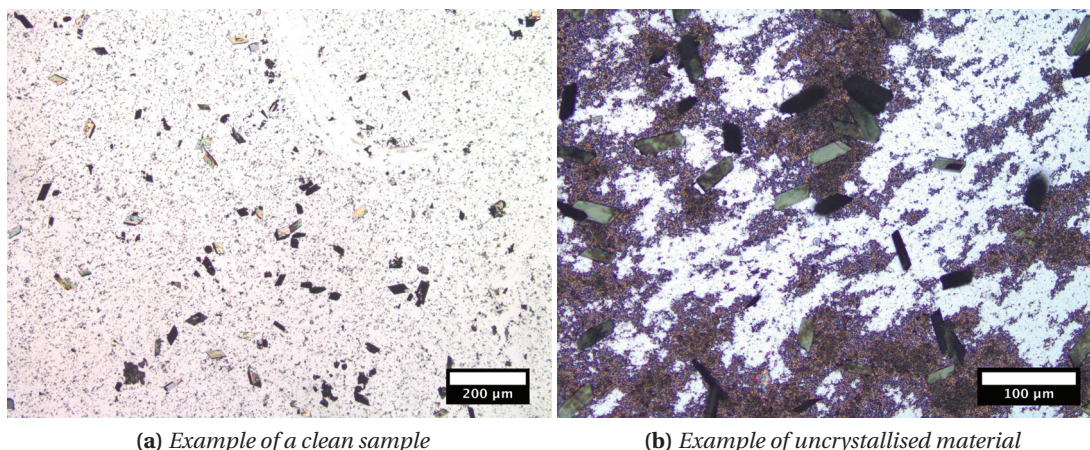


**Figure 3.3** – Two microscopy images of crystals of  $\text{Ag}_{44}$  clusters.

#### Liquid-liquid diffusion

The second method employed for the crystallisation was also realized with a binary system of solvents, DCM-hexane or acetone-hexane.  $\text{Ag}_{44}(\text{FTP})_{30}$  were solubilized at a concentration of  $10 \text{ mg mL}^{-1}$ . Instead of a flat substrate, a high aspect ratio receptacle was used, such as a NMR tube or a glass tube.

**Crystals preparation 2** Firstly, the solution was poured in the receptacle at the given concentration. Then the precipitant was added in a ratio of 4:1 or 5:1 and the vial was sealed and left in an environment free of vibrations. After one day the first crystals started to form at the interface of the two solvents and grew for four to seven days.

#### 3.3.2 Results

The two methods described above produced similar results, despite the fact that the liquid-liquid diffusion can yield to larger size crystals, because the growing process continues over time. For practical use though, the first method was preferred as it produced crystals ready to be used. In case of the second method, they needed to be transferred out of their solvent. This operation was normally done using a pipette and the crystals were then transferred on a flat surface simply by drop casting, which caused aggregation. After this operation the crystals needed to be separated in order to be characterized and used for experiments. Another serious issue linked to this technique was related to the fast evaporation of the solvent

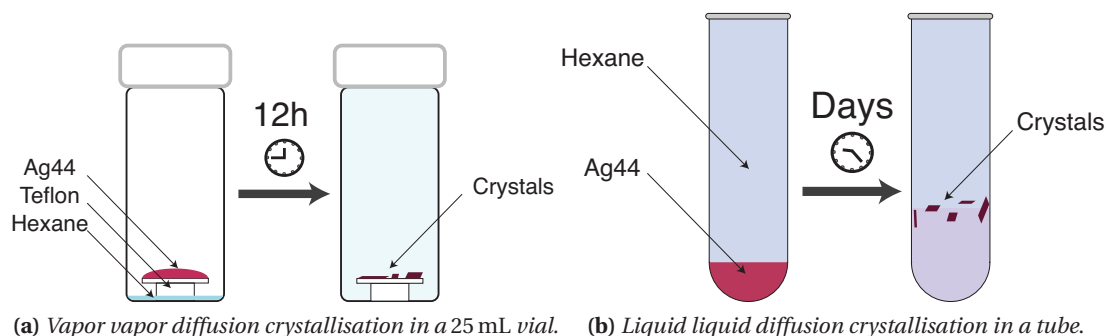


**Figure 3.4** – Schematic of the crystallisation techniques used. In both cases, the binary solvent-antisolvent combination used were DCM-hexane or acetone-ethanol.

from the crystals that caused cracking and resulted in final products that were more brittle. Crystallisations done via the first technique needed to be optimised before giving good single crystal. The parameter that was identified to play a crucial role was the crystallisation rate growth, which could be changed for instance by lowering the temperature, by diminishing the amount of antisolvent or by mixing the binary system of solvents used. In the process of finding the optimal parameters, film-like structures have been produced (figure 3.2d), where the crystallinity could be verified by polarization optical microscopy (figure 3.5). These 2D-like crystalline structures are very promising from an application point of view, because if their growth conditions could be better understood and reproduced, they could be integrated in a transistor, proving the semiconducting behaviour of the clusters or in photovoltaic as light harvesting materials. Dendritic structures, resulting from growth instabilities [107], were also

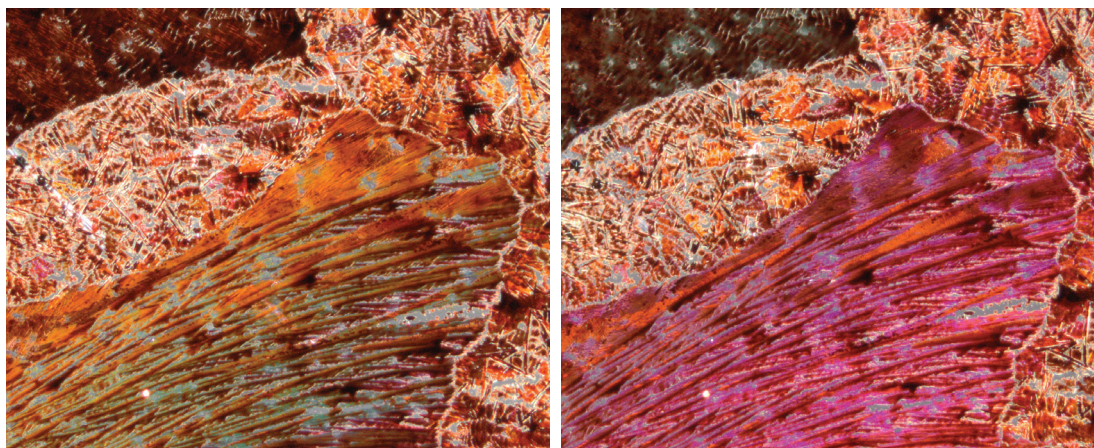


**Figure 3.5** – Film of  $\text{Ag}_{44}(\text{FTP})_{30}$  under polarized optical microscope. The change in colour indicates birefringence, thus crystallinity of the film-like formation.

observed (figure 3.2e and 3.2f). Previous work by Fang [108] demonstrated that supersaturated solutions of silver NPs lead to an anisotropic growth when the solid liquid interface is not at equilibrium. In this case the growth rate is controlled by the diffusion rate of Ag NCs in solution to the interface. When the growth was too fast the resulting crystals were small and

aggregated (figure 3.2a).

Good crystals, an example of which can be seen in figure 3.2i, were obtained when the important parameters such as nucleation sites on the surface, temperature, concentration and purity of the solution were controlled and optimised at best. The structure was determined through single crystal XRD with a synchrotron source (PSI-Villigen). The triclinic unit cell of the resolved structure belonged to the space group  $P\bar{1}$  and contained the astounding number of 588 atoms. The parameters of this crystal are summarized in table 4.3.

#### Aging

Crystals were found to be stable for about a year, stored in the dark, under ambient conditions. Passed this amount of time, the top surface of the crystals was not any more shiny, but started tarnishing, assuming a greenish to pale blue colour.

### 3.4 Characterization and fabrication

In this section are presented the main techniques employed for the characterization of the  $Ag_{44}(FTP)_{30}$  crystals. We can divide these techniques into three main categories, based on the properties they are meant to investigate:

- optical - spectroscopy and polarized microscopy;
- compositional and structural - single crystal and powder XRD, EDX;
- morphological - XRD and SEM;
- electrical - two-terminal measurements, resistivity and mobility calculation.

#### 3.4.1 Optical characterization

When  $Ag_{44}(FTP)_{30}$  were first synthesized [29], they were termed IBAN because of their peculiar optical footprint, showing eight distinct absorption peaks, narrow if compared to the typical broadband plasmonic absorption of silver nanoparticles. A characteristic feature of crystals is that they preserve the same optical behaviour, same absorption, of their constituent components. Given the relatively small size of the crystals, all measurements were carried out using a customized optical microscope (Olympus BX 61), where an optical fiber would be inserted in the beam path to direct the absorbed light into an Ocean Optics QE65000 spectrometer. The combination of the fiber core size and optical magnification would determine the spot size of the region of interest. It was possible to perform microspectroscopy on region as small as 2  $\mu\text{m}$ . For more details please refer to Appendix A. The advantage of this technique consisted in the ability to combine features of a standard optical microscope together with a UV-VIS spectrometer. On one hand this integration led to the optical investigation of small objects,

even just parts of a crystal, on the other side it was limited by the optics of the microscopes itself, *e.g.* the absorption could only be studied in the 400 to 900 nm range, because of the cut on of the beam splitter. The second limitation, inherent to the strongly absorbing nature of IBAN, was that thick crystals would have saturated the instrument, so this measurement was used only in the case of thin crystals. An example of a spectrum measured with the microspectroscopy setup can be seen in figure 3.6 together with a diascopic image containing three crystals of different thicknesses.

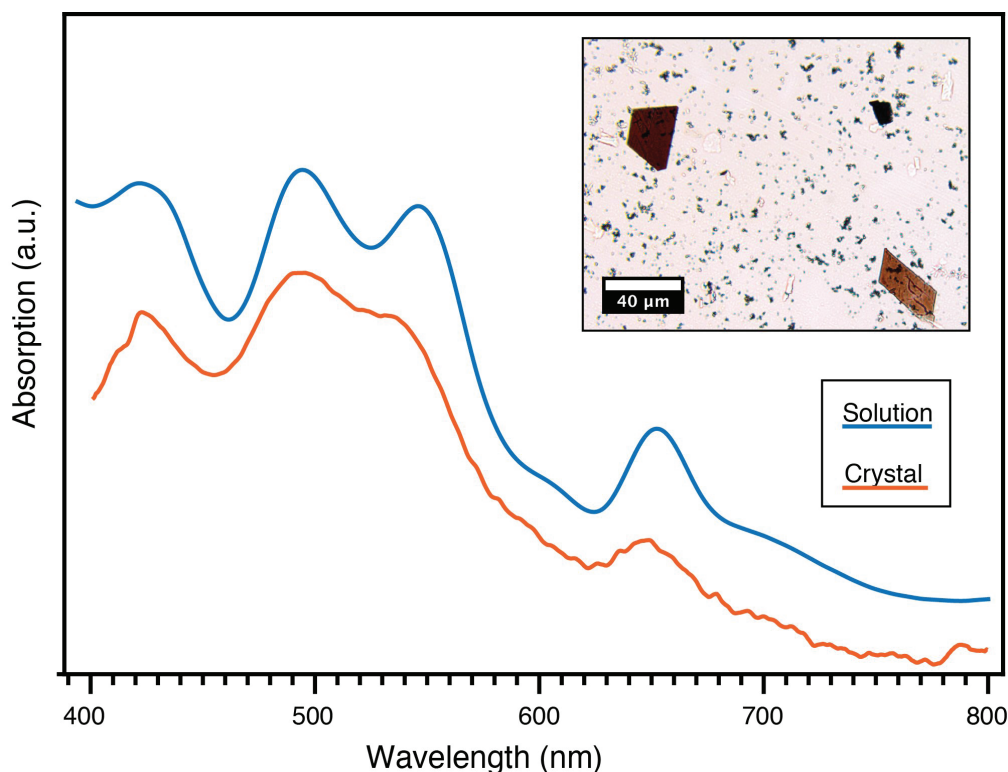


**Figure 3.6** – UV-VIS microspectroscopy of a crystal of  $\text{Ag}_{44}(\text{FTP})_{30}$ . On the left two spectra of solid (orange) and solution (blue) IBAN are shown. On the right an example of three crystals of different thickness: while those on the opposite corners are thin enough to be measured, that in the top right corner being too thick absorbs all the light that passes through and may saturate the absorption of the instrument.

### 3.4.2 X-ray diffraction

While the electron microscopy is extremely useful for direct imaging of  $\text{Ag}_{44}(\text{FTP})_{30}$  crystal. Nevertheless it is not possible to determine the structure of a material by imaging of the real space. Structural determination can be obtained by probing the reciprocal lattice with diffraction experiments, which are greatly sensitive to the periodic nature of solid's atomic structure [109]. X-ray diffraction is a powerful technique that gives insight on the structure of a crystal, as X-rays are scattered by atoms in a crystal lattice. Being electromagnetic waves, the scattering of X-rays is mainly due to electrons. When atoms are placed in a regular



manner, the result of this elastic scattering is such that if certain conditions are satisfied the secondary waves cancel each other out almost entirely. However along specific directions, they constructively interfere and add up when the difference in path length is an integer multiple of the wavelength [110]. This relationship is known as Bragg's law:

$$2d \sin \theta = m\lambda \quad (3.1)$$

where  $d$  is the spacing of lattice planes in real space,  $\theta$  is the angle between the incident beam and the lattice plane,  $m = 1, 2, 3 \dots$  is the order of peak and  $\lambda$  is the wavelength of the incident beam. Structural periodicity can be investigated by variation of wavelength (Laue method) or scattering angles (Scherrer method, angular dependent scattering). A regular array of objects, such as a crystal, can be represented as  $\mathbf{R} = n_1 \mathbf{a}_1 + n_2 \mathbf{a}_2 + n_3 \mathbf{a}_3$ , where  $n_i$  are integers and  $\mathbf{a}_i$  are the primitive vectors of the Bravais lattice. This lattice consists of the infinite set of discrete points generated by the operation of translating  $\mathbf{R}$  [13]. Waves at position  $\mathbf{r}$  are defined as  $\rho_k(\mathbf{r}) = \rho_0 e^{i\mathbf{k}\cdot\mathbf{r}}$ . Among all the wavevectors, those  $\mathbf{k}$  that have the same periodicity as the Bravais lattice are defined as

$$\rho_k(\mathbf{r}) = \rho_0 e^{i\mathbf{k}\cdot\mathbf{r}} = \rho_0 e^{i\mathbf{k}\cdot(\mathbf{r}+\mathbf{R})} = \rho_0 \left( e^{i\mathbf{k}\cdot\mathbf{r}} \cdot e^{i\mathbf{k}\cdot\mathbf{R}} \right) \quad (3.2)$$

Thus,

$$e^{i\mathbf{k}\cdot\mathbf{R}} = 1 \quad (3.3)$$

This has to be valid for all  $\mathbf{R}$ , so that it is possible to define a reciprocal lattice vector  $\mathbf{G} = h\mathbf{b}_1 + k\mathbf{b}_2 + l\mathbf{b}_3$  for which  $e^{i\mathbf{k}\cdot\mathbf{R}} = e^{i\mathbf{G}\cdot\mathbf{r}}$ . The modulus of  $\mathbf{G}$  is given by  $G = \frac{2\pi}{d_{hkl}}$ . For every real lattice there is a corresponding and unambiguously defined reciprocal lattice and the link between the two lattices is given by

$$\mathbf{b}_i \cdot \mathbf{a}_j = 2\pi \delta_{ij} \quad (3.4)$$

As it can be seen in figure 3.7, constructive interference occurs for  $\rho_0 e^{i\mathbf{q}\cdot\mathbf{r}} = \rho_0 e^{i(\mathbf{k}_{out}-\mathbf{k}_{in})\cdot\mathbf{r}} = 1$ , and with Bragg's law:

$$\mathbf{q} = \mathbf{k}_{out} - \mathbf{k}_{in} = \mathbf{G}(h, k, l) = \frac{4\pi \sin \theta}{\lambda} \quad (3.5)$$

The last expression implies that the scattered wave  $\mathbf{q}$  behaves as if it was reflected from the lattice plane  $(hkl)$ . The three reciprocal indices define symmetry planes in the lattice that show themselves in characteristic reflection peaks. Another important aspect that affects the scattered intensity of the reflections, apart from the spatial dimension and finite size of a crystal, is the composition of a unit cell. The so-called structure factor accounts for this, by describing the interference between waves scattered from the different atoms within the unit

cell [109]. Before concluding this part, it is worth to mention that shape and dimension of the unit cell are deduced by the position of the Bragg reflections, while the composition of the unit cell is to be determined by the intensity of the reflections.

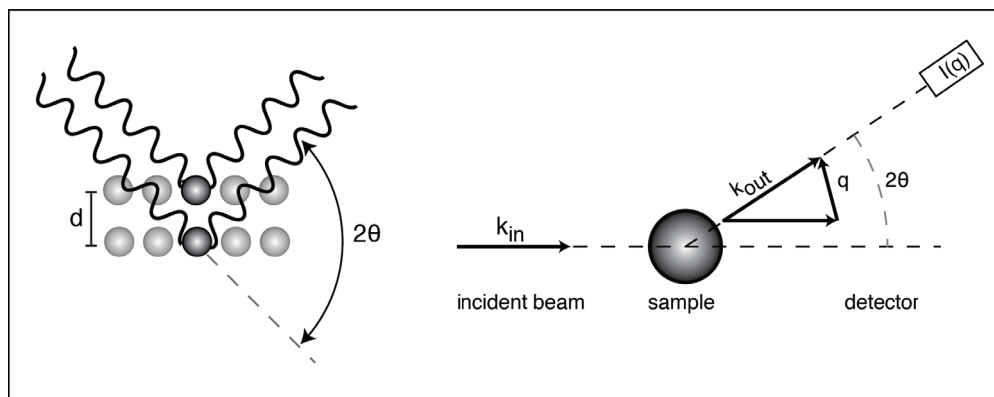


**Figure 3.7** – Principles of X-ray scattering techniques. According to Bragg's law, X-rays interfere constructively when the difference in path length  $2d \sin(\theta)$  is a multiple of the wavelength. On the right a schematic of a diffraction experiment.

### Powder XRD

In a preliminary test, before sending the  $\text{Ag}_{44}(\text{FTP})_{30}$  crystals to a synchrotron facility, the ability of our crystals to diffract was verified with a PANalytical Empirean system (theta-theta 240 mm) equipped with a PIXcel-1D detector, Bragg-Brentano beam optics and parallel beam optics.

### Single crystal XRD

Single crystal XRD experiment were carried at the Paul Scherrer institute (Villigen, Switzerland) at the Swiss Light Source (SLS), a third-generation synchrotron light source (2.4 GeV) in the X06DA (PXIII) macromolecular beamline. This beamline receives light from a 2.9 T superbend magnet. The optics focus the beam down to a spot of  $80 \times 45 \mu\text{m}$ . The detector used was a Dectris PILATUS 2M-F. Details of the performances of this beamline are reported in table 3.1.

## 3.4.3 Electron microscopy and elemental analysis

### Scanning electron microscopy

Crystals were imaged with a SEM, Zeiss Merlin equipped with a GEMINI II column. The diverse operational modes of this powerful tool allowed us to gain different information on the samples' topography and composition. High resolution images of sample surfaces were obtained from the detection of electrons that are generated by inelastic scattering, the secondary electrons. These electrons possess low energy ( $<30 \text{ keV}$ ) so that the interaction

**Table 3.1** – Beamline characteristics of X06DA (PXIII)

Wavelength range	0.71 – 2.07 Å
Spectral range	6.0 – 17.5 keV
Energy resolution	$1.4 \times 10^{-4}$ keV
Flux at 12.4 keV at 400 mA	$5 \times 10^{11} \text{ s}^{-1}$
Focused spot size	80 $\mu\text{m}$ $\times$ 45 $\mu\text{m}$
Detector	PILATUS 2M-F

volume from where they are generated is limited to tens of nanometers. As a consequence only electrons generated close to the surface are able to reach the detector. Among the different detection techniques available, I made use of the so-called In-Lens mode (or annular detector), which is placed above the objective lens and collects the secondary electrons that are scattered along the beam path. A second detection mode is the so-called HE-SE2 (or Everhart-Thornley detector), that is sensitive both to secondary electrons as well as backscattered electrons. The latter are generated by quasi-elastic scattering of primary electrons with atoms in the sample. The scattering cross section increases for heavier atoms, so that the backscattered electrons bring compositional information. Possessing higher energy than secondary electrons, their interaction volume extends underneath the surface. The collected electrons are sent through scintillators and photomultipliers and finally converted to a map of pixels with different intensities. In the course of this work, small accelerating voltages have been applied to the electron beam (<5 keV) in order not to damage the crystals. Examples of SEM images are shown in Figure 3.8.

#### Energy dispersive X-rays analysis

The same SEM was employed for elemental analysis of the crystals. EDX is a compositional analysis technique, based on the collection of the X-rays generated by the relaxation of high energy shell electrons, that fill the vacancies left by electron ejected by the high energy electron beam. The X-rays that originated from such transition are specific of each atom, so by scanning the electron beam it is possible to reconstruct a spatially resolved map of the chemical composition of an object.

#### 3.4.4 Focused ion beam

Another tool utilized in the course of this work is the focused ion beam (FIB), a dual instrument composed of a SEM and a second part that uses ions rather than electrons. Typically FIBs [111] use gallium ( $\text{Ga}^+$ ) ions that come from a liquid metal ion source: metal Ga is heated and then placed in contact with a tungsten needle, so that the latter would be wet by the former. High voltages are applied to the tungsten needle that cause the ionization of gallium. The

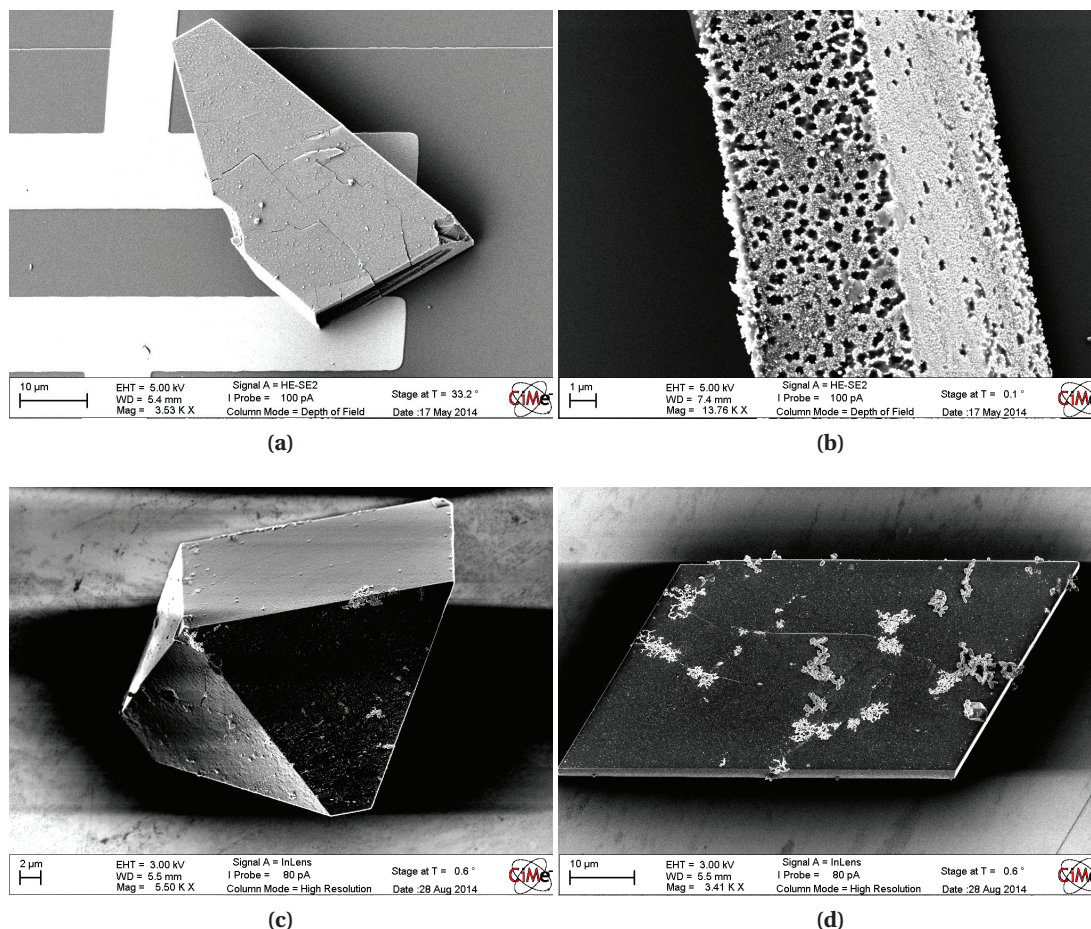


**Figure 3.8** – SEM images of different IBAN crystals. Figure 3.8a) shows a hollow crystal. Figure 3.8b) exhibits porosity and small agglomerations on the surface. Figure 3.8c) shows crystal with a smooth top surface. Figure 3.8d) represents a crystal of average size.

ions are further accelerated and focused with onto the sample by electrostatic lenses, similar to those of a SEM. A FIB can operate mainly in three modes: firstly, it can act as imaging system. Exactly as an electron beam in a SEM,  $\text{Ga}^+$  ions are scanned over the sample and secondary particles, like neutral atoms, ions and electrons, are ejected from the surface. These species are then collected by a detector that generate an image. The main disadvantage of this imaging technique, and more in general for FIB, is that gallium ions are implanted in the sample. Additional consequences of this implantation are lattice defects and amorphisation of the surface, while the displacement of atoms causes local heating, thus damaging of the sample. Secondly, the FIB can operate in a sputtering-milling mode. The kinetic energy of the accelerated ions is high enough atoms of the targeted material can be removed through elastic and inelastic collisions causing. Lastly, FIB can be used to deposit Pt pattern through ion-beam assisted chemical vapour deposition. Ion beam induced deposition is a chemical vapor deposition technique, based on the introduction of trimethyl platinum,  $\text{C}_9\text{H}_{16}\text{Pt}$ , that is dissociated by the ion beam into its volatile and non-volatile component [112], Pt, that

remains on the surface as deposition. The volatile part is then pumped away through the vacuum system of the FIB.

## 3.5 Electrical characterization

The electrical characterization constituted an important part for the development of this thesis. The aim of most of the work done was to understand the electrical behaviour of IBANs, which have been so far neglected for the simple reason that there was no availability of solid-phase material that would not deteriorate upon air exposure. The enticing findings that we came across have paved the way for the first use of this material in real applications. This part of thesis describes in details the methodology used for electrical characterization, the variety of techniques and instruments involved, as well as the samples fabrication.

### 3.5.1 Two-terminal IV curve

Unfortunately, crystal of IBAN are soluble in most of the common solvent used in standard fabrication polymeric photoresist so that microfabrication was not a viable solution for the realization of metallic contacts that would have worked as electrodes. This was the reason why crystals were directly contacted with metallic probes (see figure 3.9). Micromanipulators that allowed fine control on the probes positioning were used in order to approach, move, rotate and contact the crystals. This approach is called the two-terminal configuration, meaning that the force and sense of a parameter analyzer were realized along the same wiring pathway.

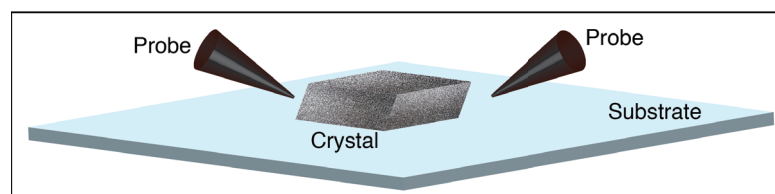


**Figure 3.9** – Two-terminal configuration where the crystal is handled and directly put in electrical contact with metallic probes (copper, beryllium-copper or tungsten).

The metallic probe used varied in material composition and in tip radius. The choice of the radius was constrained by the crystal size, which limited the use to small radius ( $<10\mu\text{m}$ ). Concerning the material composition, probes of different metals have been employed because each of those responded to diverse needs, from mechanical stiffness to charge injection properties. It is important to clarify that by the word probe I identify all the contacts that act as electrodes for the crystals, so the conductive silver paste and gallium-indium eutectic have been here called probes. I refer to tip when the contact was realized through a conically shaped metallic probe. The following list contains a detailed description of the probes employed for the electrical contacts of IBAN crystals.

List of tip probes used:

### Chapter 3. Experimental section

---

- Tungsten tips are the most common choice for electrical connection of microfabricated devices. The good electrical and thermal conductivity together with its hardness and resistance to fatigue are among the reason why these tips provide consistently repeatable contact force. Tips radius varied from 10  $\mu\text{m}$  to 0.5  $\mu\text{m}$ . Tips were purchased from Cascade Microtech (USA) and Microworld (France).
- Beryllium-Copper tips have been tested to verify that the properties that  $\text{Ag}_{44}(\text{FTP})_{30}$  crystal exhibited did not depend on the material contacts. Compared to tungsten tip, BeCu is softer, and thus causes less damage to crystal surface, and it has a lower contact resistance than tungsten. On the other side though, it is less resistant to fatigue and it had to be replaced more often. Tips' radius varied from 2  $\mu\text{m}$  to 5  $\mu\text{m}$  and were purchased from Cascade Microtech(USA).

List of other probes used:

- Silver paste, purchased from Ted Pella, was spread with the help of a needle or a cut optical fiber next to a crystal, which was subsequently pushed towards the drop of Ag paste, just before it had completely dried. I limited the use of this substance because despite the ease of use and handling, it contained solvent that could have damaged the crystals.
- Gallium-Indium eutectic is a conductive metal fluid, composed of 75.5% Ga and 24.5% In by weight, purchased from Sigma Aldrich. The low viscosity liquid is easily moldable and poorly interacting with crystal. The main disadvantage of this material was that it did not wet the crystal as well as the substrate, so it was not easy to handle.
- Platinum pads were chemically vapor deposited on the crystal with an assisted ion beam from a platinum precursor. The big advantage of this technique was that the contact leads were microscopically placed on top of the crystal's surface.

Crystals were measured with two different electrical setups: one was employed for measurements done under atmospheric conditions, while the other was used for testing the same quantities in a inert environment.

**Atmospheric conditions** The setup used was a commercial Summit Semi-automated probe station from Cascade Microtech. The substrate holder could hold big wafer and with an external controller it was possible to set a desired temperature. The holder was automatized and controlled with a joystick that allowed a fine movement of 5  $\mu\text{m}$ . Crystals were handled and put in electrical contact with micromanipulators, DPP 210 and DPP 305. The metallic tip probe were inserted at the end of a suspended arm of the manipulators, so the mechanical stability of the last one was an important requirement in order to damp vibrations coming from the environment, which could have caused a loose crystal-probe contact. The micromanipulators were connected to the measuring device with low noise triaxial cables. The

### 3.5. Electrical characterization

---

electrical measurements of the crystals in this setup were performed with a Keysight 4156C Precision Semiconductor Parameter Analyzer that allowed to apply 0 V to 100 V while measuring currents with an accuracy of  $\pm 100$  fA.

**Inert atmospheric conditions** In order to understand whether oxygen and water played a role in the electrical response of  $\text{Ag}_{44}(\text{FTP})_{30}$  crystal, the experiments were also carried in a glove box filled with Argon Ar. The setup was homebuilt (for details see Appendix C), but it consisted of a sample holder stage that could be manually rotated and moved along  $x$ ,  $y$  and  $z$ . The micromanipulators used in the glove box were model DPP 105 from Cascade Microtech. The choice of the manipulators was limited because of the space limitations of the glove box, and this resulted in the huge disadvantage of tip probes being significantly more affected by vibrations. The tip probes were connect with the parameter analyser through triaxial cables. For this setup a Keithley SCS 4200 that allowed to apply voltages in a broader range, 0 V to 210 V, with measured current accuracy of  $\pm 100$  fA was used.

### 3.5.2 Substrate fabrication and sample preparation

Substrates were prepared in the CMi cleanroom facility at the EPLF. Four inches wafers, 525  $\mu\text{m}$  thick, with 500 nm oxide layer, were soft baked at 120  $^{\circ}\text{C}$ , before being coated with a double layer of photoresist (positive tone AZ1512-HS and LOR 5A, 0.48  $\mu\text{m}$  and 1.1  $\mu\text{m}$  in thickness respectively).

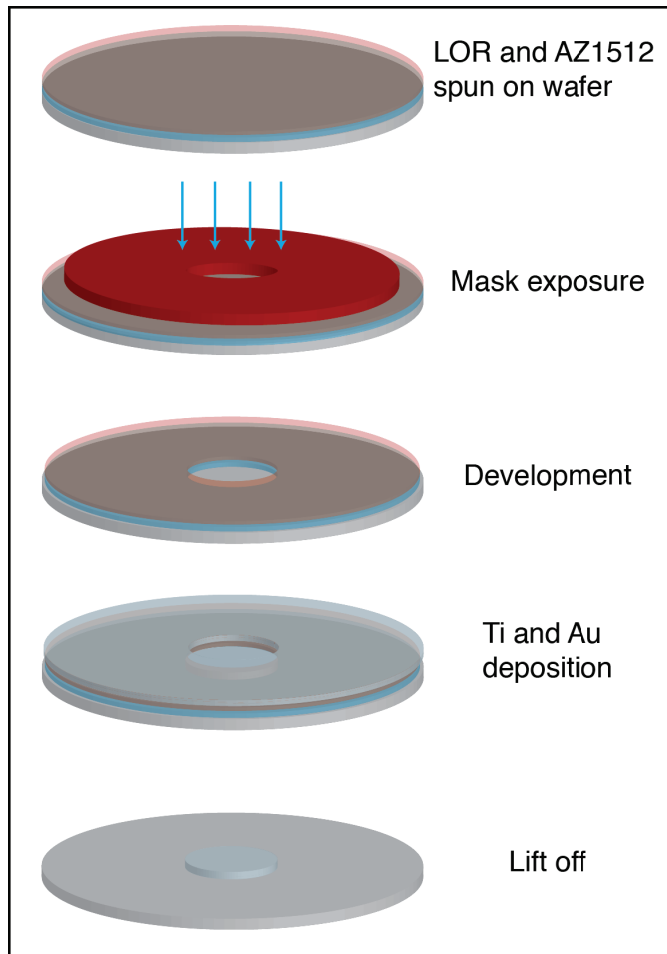


**Figure 3.10** – Fabrication steps of the substrates use for FIB deposition.

risk of cracking of the deposited Pt leads, due to the steep height difference. Additionally, the glue formed an insulating barrier on the sides of the samples preventing that Pt was deposited on it or under it, which might have resulted in current leakage. Once the glue had dried trenches of about 100 nm in depth were etched by FIB milling on the exposed sample surface where the Pt leads wanted to be deposited. The reason for this cleaning procedure was to improve the interface of the crystal with the Pt contacts, by lowering the contact resistance. Then Pt leads were deposited using ion beam at 30 keV with current density of 6  $\text{pA cm}^{-2}$  to 20  $\text{pA cm}^{-2}$  to reduce the carbon content in the deposit. Typical dimension fo the Pt contacts

After UV light exposure and development, an adhesion thin layer of titanium 5 nm was deposited, followed by 200 nm of platinum. This metal was preferred over gold because of the strong affinity between gold and thiols[Love:2005dk]: FTP could have migrated from  $\text{Ag}_{44}(\text{FTP})_{30}$  crystals to the metal Au electrode. The wafer was then immersed in a solvent bath in order to lift off the electrodes surrounding the metal, but leaving behind the desired geometries. One important step consisted of placing a small drop of epoxy glue (EPO-TEK 301) that would embed the crystal protecting it from the possible formation of a carbon sheet, contained in the platinum precursor, that would act as halo resistance [113, 114]. This embedding step was also important because the solidified epoxy created a slope that gradually reduced the edge jump between the top surface of the sample and the metal contacts of the chip. The solution helped also in reducing the



were  $5\ \mu\text{m}$  to  $20\ \mu\text{m}$  wide and  $0.2\ \mu\text{m}$  to  $1\ \mu\text{m}$  thick. Lastly, a final etching step would also be performed in between the deposited electrodes to clean the surface and avoid short halo effect.

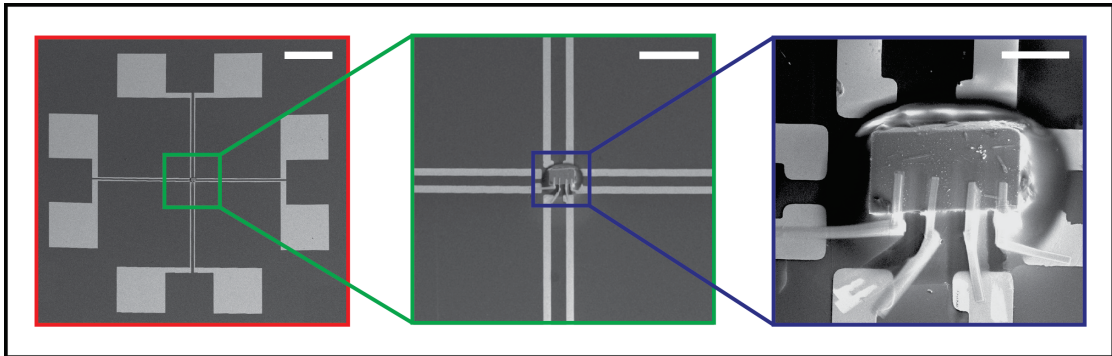


**Figure 3.11** – Picture in the red square is of a whole device (scale bar  $500\ \mu\text{m}$ ). In the central image it is possible to see how four of the eight available substrate electrodes have been connected (scale bar  $100\ \mu\text{m}$ ). In the blue box a zoom of the connected crystal shows a more clear area among the deposited electrodes on the crystal surface that correspond to the etched area (scale bar  $20\ \mu\text{m}$ ).

The final result is showed in 3.11, where a crystal is connected to the substrates electrodes through ion assisted pad of platinum. The ion beam current was an important parameter to be controlled during the platinum deposition: too high currents destroyed the crystals, melting the clusters and causing the formation of a superficial layer of metallic silver. As it can be seen in figure 3.12, the top surface of the crystal melted and changed contrast. This SEM image shows all the difficulties linked to the use of FIB: an incorrect calibration of the current and acceleration voltage setting could cause the damage of the top surface of the crystal, degrading the IBAN into metallic silver. Similarly to the carbon sheet originated from the Pt deposition, this damaged surface acted as a shunt resistance. Typical Voltage current measurements of these kind of crystals showed currents of the order of microampere, *i.e.* three order of magnitude higher than a not damaged crystal.

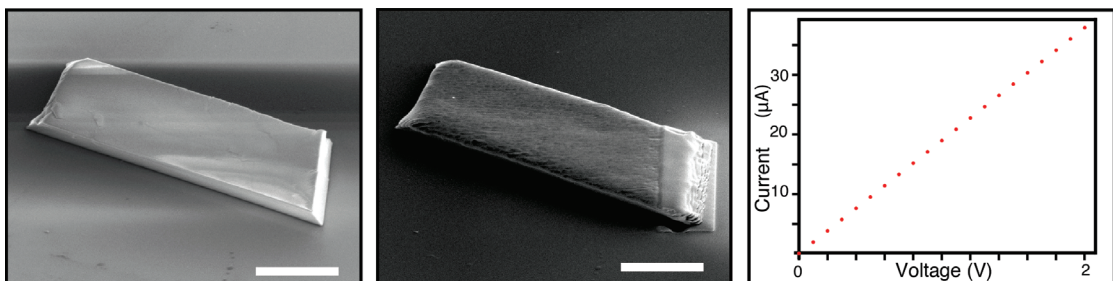


**Figure 3.12** – The two images clearly show a change in contrast of the crystal top surface. The linear ohmic characteristic indicates a metallic behaviour. Scale bars are  $5\ \mu\text{m}$ .

### 3.5.3 Conductive AFM

Conductive AFM was performed using the ORCA module of a Cypher-S AFM (Oxford Instruments Asylum Research, Santa Barbara, CA, USA). The crystals were attached with silver paste on a highly doped silicon wafer, which was then glued with conductive epoxy on a stainless steel disk (SPI supplies, West Chester, PA, USA). The electrical connections between the metallic disk and the voltage supply were placed using tools and procedures as described by the AFM provider. Conductive AFM tips (ASYELEC-01, Asylum Research, Santa Barbara, CA, USA) were mounted on the ORCA cantilever holder. The voltage offset was corrected by measuring the tip-sample bias at no applied voltage with a multimeter and the electrical connections tested by closing the circuit with a known resistance. The sample was thus engaged in contact mode and the surface scanned with a velocity of either 1 Hz or 0.5 Hz, depending on the scan size. Generally the set-point had to be kept relatively low (between 100 mV to 300 mV with a  $0 \pm 10$  mV initial value of deflection) and the integral gain quite high (around 100) to compensate for the high surface roughness. This is the reason why, occasionally, a feedback-induced ringing can appear in the images. Nevertheless with these scanning parameters a reliable and consistent tracking of the surface was possible. Image analysis was performed either with the inbuilt software of the AFM (Igor-Pro, Wavemetrics, <https://www.wavemetrics.com>) or with gwyddion (<http://gwyddion.net/>).

# 4 Experimental results

## 4.1 Chapter outline

The main results achieved in the course of this thesis are reported in this chapter. Emphasis is given to the electrical characterization of  $\text{Ag}_{44}(\text{FTP})_{30}$  crystals. The first part of this chapter deals with the characterization of the optical properties of crystals. This part is fundamental in retrieving values, such as the relative permittivity of the material, which has been later used to determine the electrical mobility of crystals. The second part, which corresponds to core of the work, consists of the characterization, in air as well as in inert environment, of electrical properties of IBAN crystals. A change in conductivity is observed for increasing and decreasing voltage sweeps, together with a relaxation mechanism that brings the crystals to their low conductive state. Both of these processes present interesting features, summarized in Table 4.2, such as step-like and size dependent conductivity changes.

## 4.2 Optical properties

The name IBAN originates from the peculiar property of the NCs being an intensely absorbing material [29]. Its absorption does not come from collective charge oscillation, more commonly called plasmons, as it happens for silver NPs [115], but rather from their size that dictates the discrete nature of the energy levels [Dass:2011cs]. As anticipated in the previous chapter, crystals of IBAN preserve the optical properties of their constituent, exhibiting the characteristic broadband absorption.

### 4.2.1 Crystals microspectroscopy

The light-matter interaction of  $\text{Ag}_{44}(\text{FTP})_{30}$  crystals was studied with the a customized Olympus BX-61 microscope (see Appendix A for details). Crystals' absorption was studied using diasopic illumination, with the light crossing the glass substrate before the sample under investigation. Given the highly absorbing nature of IBAN, too thick crystals could not be

## Chapter 4. Experimental results

---

measured, as insufficient light passed through. In Figure 4.1 a crystal was positioned in the centre of the optical beam, that coincides with the spot projected on the conjugate plane of the optical fiber, thus of the spectrometer, and its spectrum recorded.

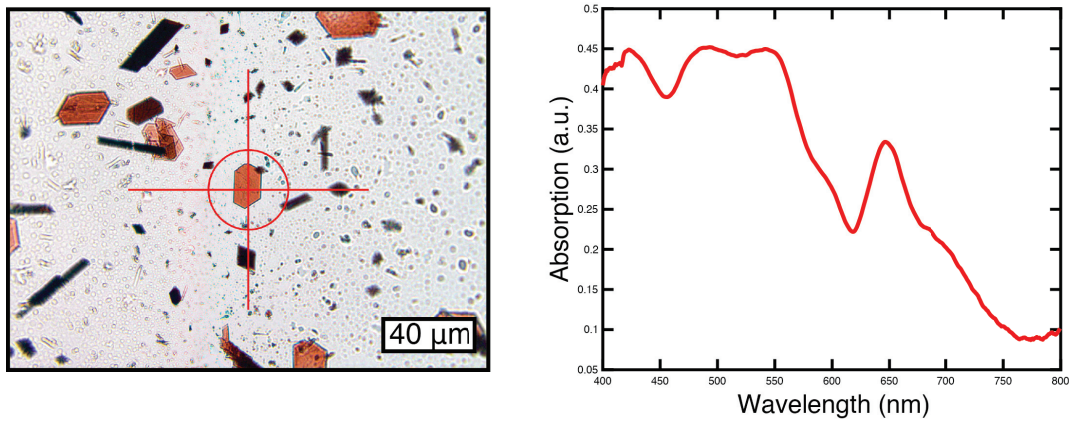


**Figure 4.1** – An example of crystal targeted for microspectroscopy and its UV VIS spectrum

Spectra of IBANs were used to find important physical properties such as refractive index and permittivity. The detailed explanation of the methodology used is presented in Appendix B. To summarise, it was possible to determine the extinction coefficient  $k$ , or negative part of the imaginary refractive index, through the measured absorbance of a crystal knowing its thickness. Once the extinction coefficient was determined, being the complex refractive index an analytical function in the upper half plane of frequencies, the real part  $n$  was determined thanks to Kramers-Kronig relationships [116–118].

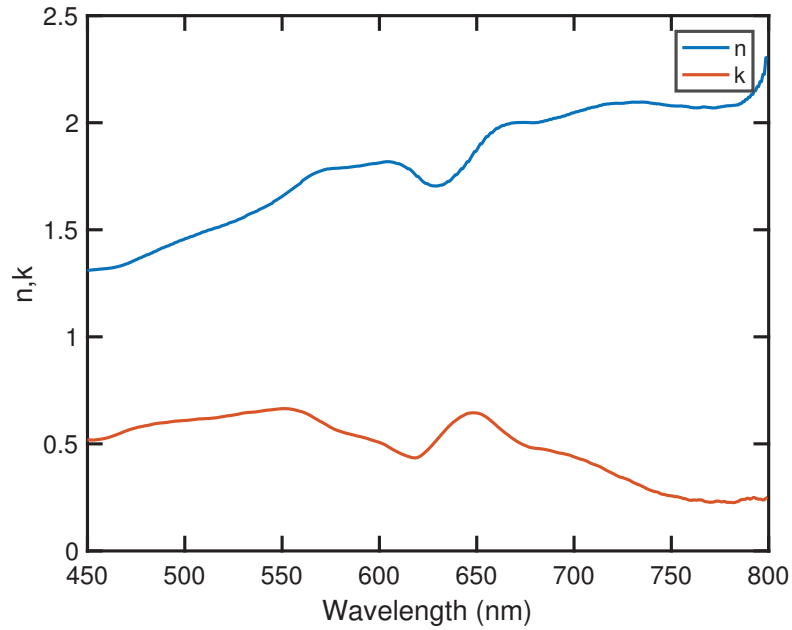


**Figure 4.2** – Real,  $n$ , and negative,  $k$ , parts of the refractive index from a measured UV-VIS crystal absorption spectrum.

Once the real and imaginary parts were known (see Figure 4.2), it was straightforward to determine the complex permittivity for each wavelength. The real and imaginary components of the complex permittivity provide insight respectively into the stored energy and the dissipation/loss of energy within the material [119]. The quantity  $\epsilon_i/\epsilon_r$  represents the ratio of conduction current and displacement (polarization) current contributions [120, 121] since:

$$J_{tot} = J + \frac{\partial D}{\partial t} = \sigma E + i\omega\epsilon_r E = i\omega\epsilon E \quad (4.1)$$

where  $\epsilon = \epsilon_r + i\epsilon_i = \epsilon_r + \frac{\sigma}{i\omega}$ . Therefore the ratio, also called the loss tangent, since it is given by the tangent of the angle formed by the complex components of the dielectric function, establishes a border between dielectrics and conductors. Materials that are good conductors and exhibit high loss to electric field propagation have a ratio  $\gg 1$ , while dielectrics that show poor conductivity and exhibit low loss, have a ratio  $\ll 1$ . In our case, thin crystals of IBAN proved to behave as poor conductive material, having a ratio that spanned from 1 to 10.

#### 4.2.2 Polarised optical microscopy

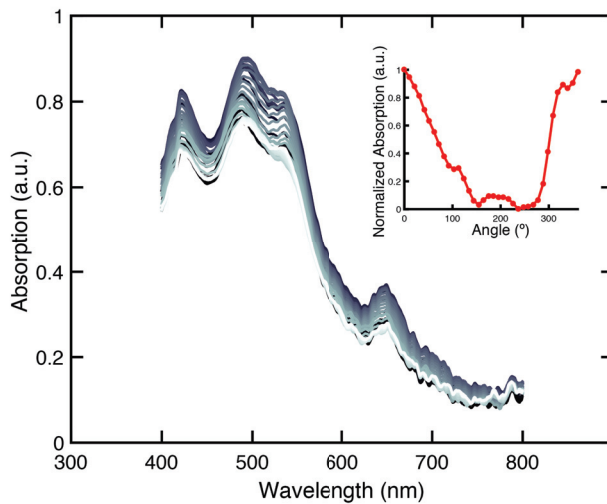
Polarised optical microscopy measurements allowed us to determine the birefringent properties of the crystal. Crystals were positioned on a rotating stage in between two polarization filters, called polariser and analyser. Diascopic illumination was passed through the first filter in order to polarise light. Light passing through the crystal imparted a rotation to the light, or produced two wave components, named ordinary and extraordinary waves, that became

## Chapter 4. Experimental results

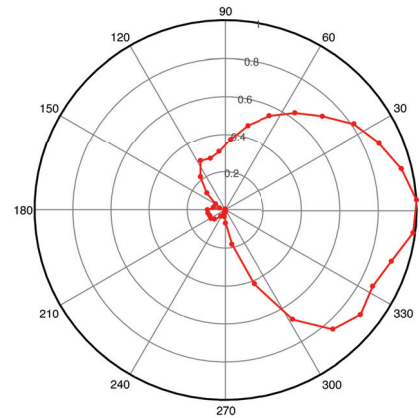
out of phase once they exited the crystal. The second polariser made these two components to interfere constructively or destructively. The optical path difference  $\delta$  of the two waves calculated with a Michel-Levy chart and defined as

$$\delta = \Delta n \times t \quad (4.2)$$

where  $\Delta n$  is the birefringence and  $t$  is the thickness of the samples, was found to be very small resulting in a weak birefringence ( $\Delta n < 0.005$ ). This small birefringence can be seen in Figure 4.3, where a crystal was measured while turning the rotational stage by steps of  $10^\circ$ . The absorption was measured at each angle and the normalized intensity of the main absorbing peak at 490 nm was plotted as a function of the stage position angle. This absorption peak varied within 0-17%, without fully extinguishing the light transmission.



(a) Absorption spectra of a crystal at different angles .



(b) Polar plot of the normalized absorption at 490 nm.

**Figure 4.3** – Absorption spectra of a crystal under polarised optical microscopy. The onset shows the normalized intensity absorption of the 490 nm peak at the different angles.

### 4.3 Electrical properties

Despite the fact that the optical and electronic properties of IBAN have been widely studied [29, 65, 66, 103, 122, 123] together with its mechanical properties and response to external stimuli [66, 67], very little has been done to characterize the electrical properties of these clusters. The main reason for this slow development is that the material has been only recently crystallised and its processing it is still limited by the fragility of the crystals and by the fact that common solvents used in microfabrication dissolve the crystals. Here are presented the strategies adopted to circumvent these problems and the main enticing findings of this work.

#### 4.3.1 Two-terminal measurements

These experiments were performed with the probe stations described in Section 3.5. Crystals were positioned under the microscope and approached by the metallic tips, W or BeCu, of the micromanipulator. Based on the result obtained from single crystal XRD measurements, from thermodynamics calculations we have estimated that the majority of the crystals exhibited the face corresponding to the [001] plane parallel to the substrate surface (see Figure 4.4), so that approaching from the convex angle formed by [100] face would have helped in lifting the crystal from the substrate. This operation, as it can be seen in Figure 4.5, caused some

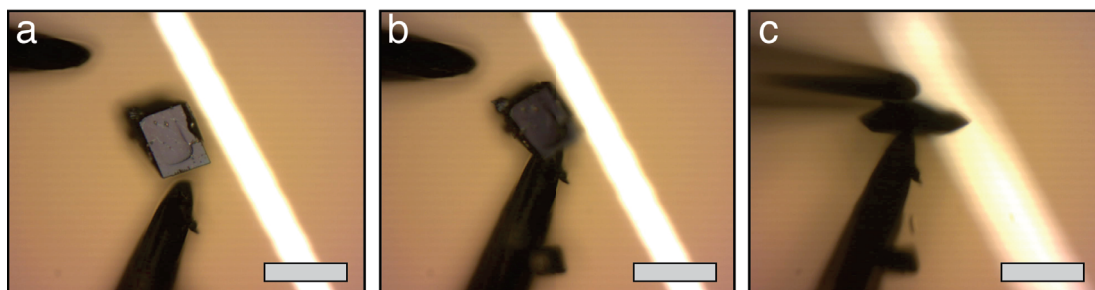


**Figure 4.4** – Crystal approached by two tungsten tips. The crystal face parallel to the substrate is that corresponding to the [001] plane that forms with [100] a convex angle, from where it is easy to insert the tip to lift the crystal (b). Once the crystal has been lifted, the other tip is gently approached and put in contact on the opposite face of the crystal (c). Scale bars 30  $\mu\text{m}$ .

uncountable damage to the crystal, but nonetheless even for successive testings the results were consistent. Even after the electrical measurements, the chemical composition of the surface did not change as shown by EDX. The ratio of silver to fluorine and silver to sulfur did not change before and after the electric field was applied, confirming the stability of the crystal.

The first consideration that arises from the observation of Figure 4.6 is that the crystal of  $\text{Ag}_{44}(\text{FTP})_{30}$  did not behave as good conductors: at low voltages, smaller than 1 V, the current measured was of the order of a few picoamperes. As it has been mentioned in Chapter 1, silver clusters do not behave as bulk silver, and the good quadratic fitting ( $R$ -square=0.98) proved the deviation from ohmic behaviours, *i.e.* metal-like, of this material at low voltages. Linearisation

## Chapter 4. Experimental results

**Table 4.1** – Comparison between exact and calculated compositional ratio of Ag-P, Ag-F and Ag-S from EDX spectrum

	Real	EDX
Ag-S	1.466	1.461
Ag-F	1.466	1.458
Ag-P	11	8.9

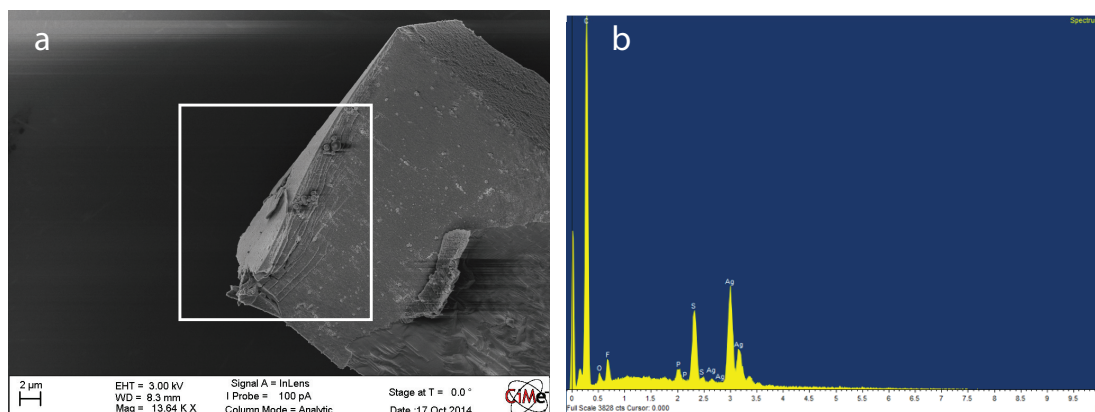


**Figure 4.5** – a) SEM image of a crystal after being contacted with tungsten tip. The white box encloses some visible cracks. b) EDX spectrum of an area within the white box. The calculated ratio of silver-sulfur and silver-fluorine for  $\text{Ag}_{44}(\text{FTP})_{30}$  after IV test was in excellent agreement with that real ratio (see table 4.1).

of the fitting curve led to a resistance of the crystal of  $R=905 \pm 15 \text{ G}\Omega$ . The origin of deviation from ohmic behaviour at low voltages may be due to the nonlinear Schottky barrier formed at the probe-crystal interface.

### Switching mechanism

These first experiments were conducted in ambient atmosphere, so in presence of oxygen and water. Despite the risk of oxidizing the crystal surface, voltages were increased up to point of observing the presence of a voltage threshold after which the crystal, still remaining poorly conducting, would show an increase in conductivity up to several order of magnitude. This can clearly be seen in Figure 4.7, where at about 26 V the current of the onward sweep increases dramatically by four orders of magnitude and remain as such during the return sweep.

This switching mechanism suggested the adoption of a terminology borrowed from logical memory technology: a poorly conducting crystal would have been referred to as switched-off or erase, while a crystal that exhibited higher conductivity would have been called switched-on. Once crystals were switched-on, they remained so as long as they were measured, that is as long as energy was provided. Eventually they underwent a reversible process that brought them back to their initial switched-off state. It was not easy to estimate the lifetime of the



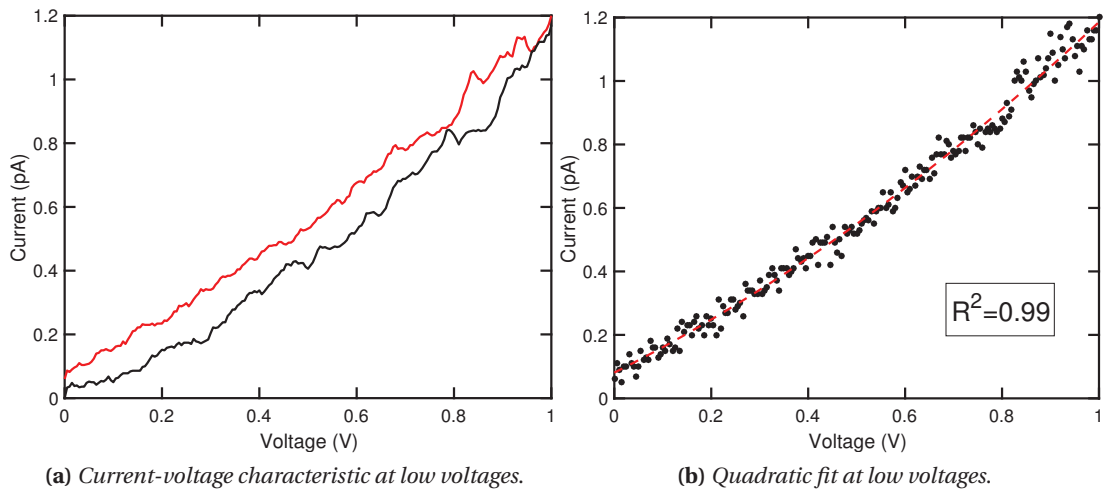


**Figure 4.6** – The two graphs show the nonlinear behaviour of  $\text{Ag}_{44}(\text{FTP})_{30}$  crystals for low voltages. On the left the red curve represents the onward sweep 0V to 1V, while the black the return sweep 1V to 0V. Some hysteresis is present in the measurement. The image on the right shows a quadratic fit with  $R$ -square=0.99, from which it is possible, after linearization at small voltages, to determine the resistance of the crystals to be  $R=905\pm 15\ \text{G}\Omega$ .

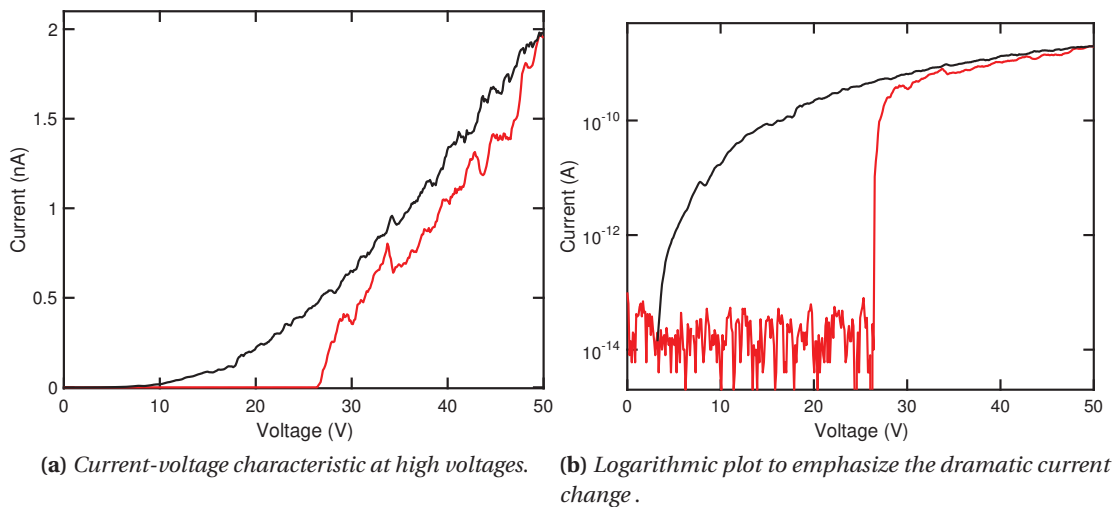


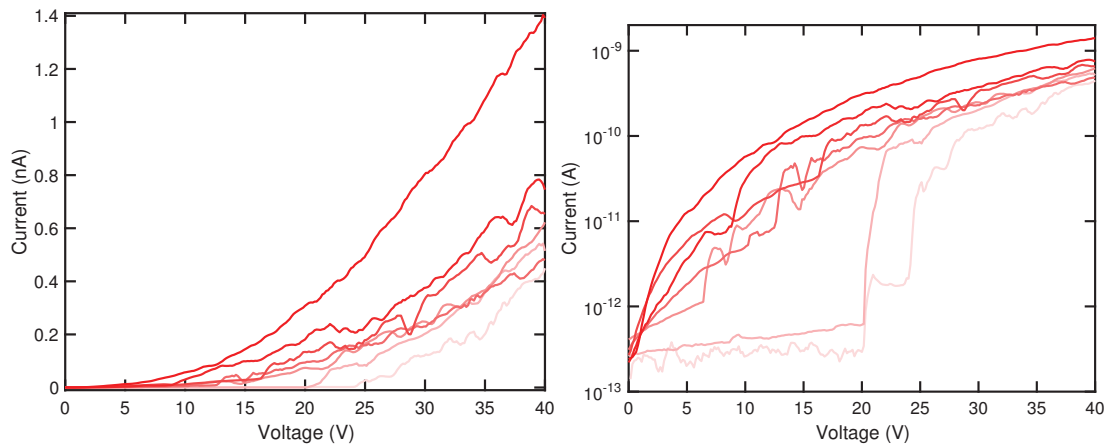
**Figure 4.7** – Typical occurrence of a switching mechanism. In Figure4.7a a first voltage sweep (red curved) was applied to the crystal. At  $V_{th}=27\ \text{V}$  the current dramatically increased by four orders of magnitude. This change can be better appreciated in Figure4.7b.

higher conductivity state, since it varied significantly from crystal to crystal.

Successive measurements on electrically relaxed crystals showed a decrease in the position of the threshold voltage, suggesting that in consecutive measurements less energy was required to obtain a conductive crystal. In Figure 4.8 seven consecutive measurements were taken on the same crystal, each one after a fifteen minute waiting time. It is possible to observe that firstly the threshold voltage lowered its position as a function of the number of the

## Chapter 4. Experimental results

measurements (transparent to opaque curve). Secondly, there was a tendency for the current to increase as the voltage threshold decreased.



(a) Threshold voltage position for consecutive measurements.

(b) Logarithmic plot of threshold voltage position.

**Figure 4.8** – Threshold voltage position for consecutive measurements, the first measurement being represented by the most transparent trace and last one by the fully opaque. Additionally, as the threshold voltage decreases, the measured current value increases for successive measurements.

This switching mechanism could have been more or less pronounced, that is the change in conductivity could have been more or less steep. Moreover this behaviour was not displayed uniquely, in the sense that it could also appear as a step-like increase, involving different incremental steps as can be seen in Figure 4.9, where the current jumped to a higher value at 172 V, 175 V and 192 V. The change in conductivity, more rarely, occurred also for decreasing voltage, that is the voltage was swept from low to high values, without observing any change, and then while it was swept back, a sudden current change would have showed. This can be observed in the last two images of Figure 4.9.

Another interesting feature of the switching mechanism of IBAN crystals was the position of the threshold when the electric field was applied across different crystal faces. Despite the longer size, crystals showed consistently a lower threshold when contacted lengthwise rather than widthwise, as it can be seen in Figure 4.10. Regarding the other dimension, *i.e.* depth, when the crystal would have been connected across the two faces parallel to the substrate, the threshold voltage would have been even lower, but rarely depth was comparable in terms of size to length and width, being much thinner.

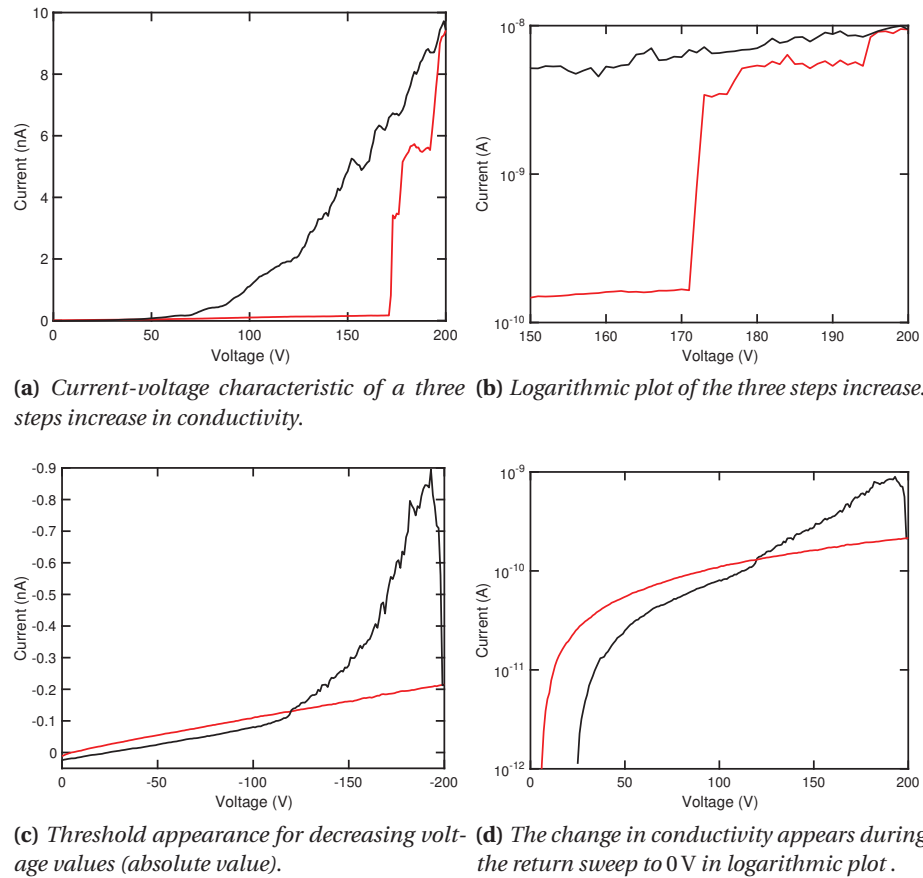


Figure 4.9 – Step-like increase in conductivity.

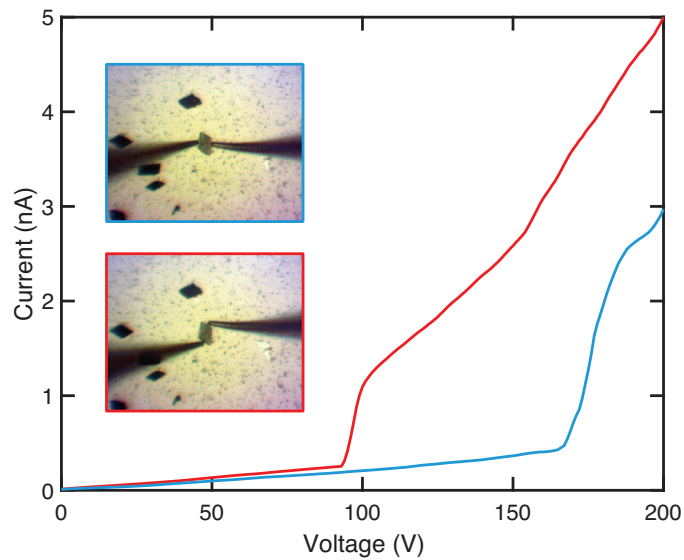
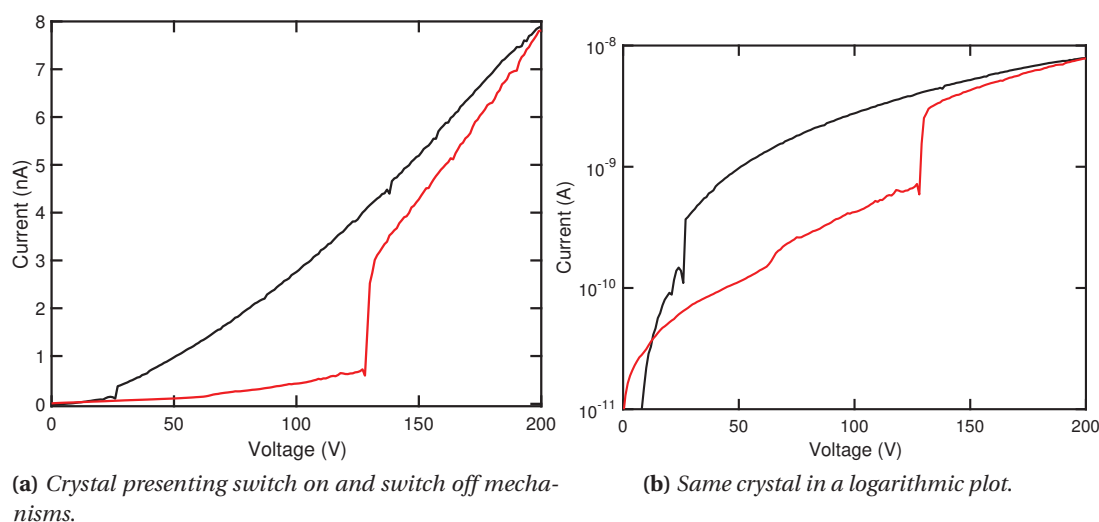


Figure 4.10 – In the blue box a crystal connected widthwise, while in the red box the same crystal connected lengthwise. The switching occurred to a lower voltage, despite the longer length, when the crystal was connected lengthwise.

## Chapter 4. Experimental results

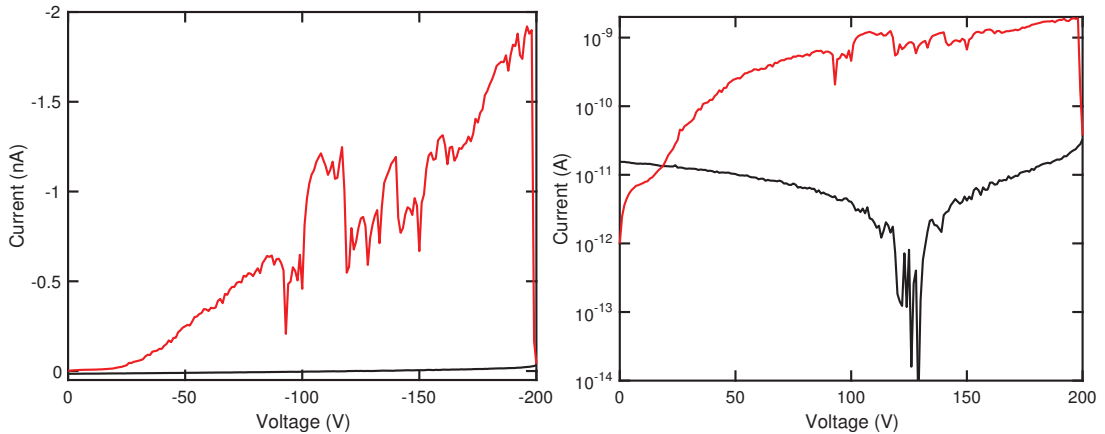
More interestingly the change in conductivity was found to be a reversible mechanism: other than returning to their original conductive state when left for all the relaxation mechanisms to occur, crystals of IBAN exhibited opposite jumps to those that brought the crystal to a higher conductivity, bringing them to lower values of conductivity. It is worth to mention that the voltage of this opposite process did not match that of a switch-on, but instead it very frequently appeared at lower voltages, as it can be seen in 4.11.



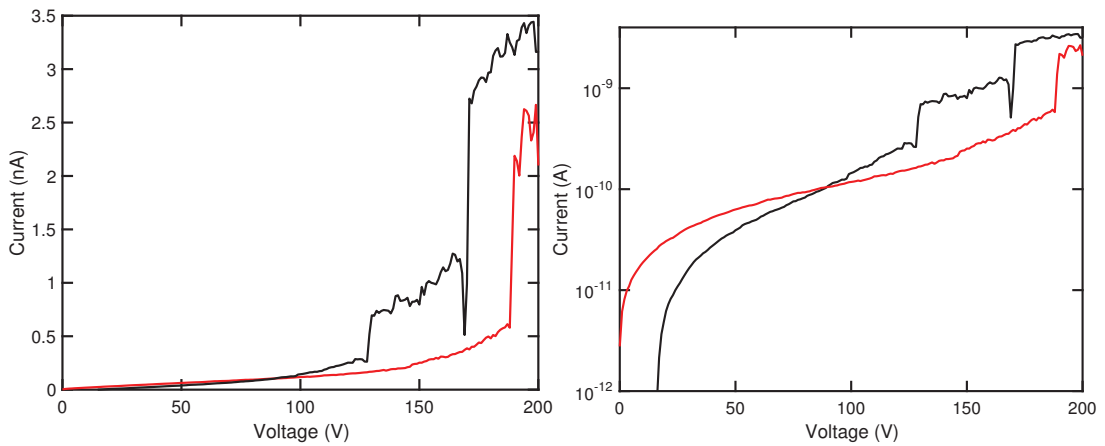
**Figure 4.11** – Several examples of switching off mechanism. In 4.11a a crystal had been switched on during a voltage sweep from 0 V to 200 V (red curve), then during the return sweep (black curve) at approximately 25 V the current dropped down.

All the features that have appeared in the increase in conductivity are also present for this opposite mechanism. In some case the reverse switching mechanism happened in increasing as well as decreasing voltage values (Figure 4.12a), and it also occurred through discrete jumps to low current values (see Figure 4.12c).

Both these mechanisms, switch-on and switch-off, have been extensively studied and reproduced under different conditions. In order to demonstrate that the properties investigated did not depend on the contact resistance of the crystal-tip system [124], different probes have been tested, more specifically tungsten and beryllium-copper (see Section 3.5). Figure 4.13 shows two current-voltage plot measured on the same crystal with the aforementioned materials. As it can be seen, the two curves are almost identical since both material have a very high working function [125, 126]. Identical results have been obtained for crystal measured in inert atmosphere, Ar glovebox with  $[O_2] < 5$  ppm and  $[H_2O] < 2$  ppm, where also no differences have been observed.



(a) Conductivity drop for increasing voltage values. (b) Same crystal in logarithmic plot.  $x$  and  $y$  axis report absolute value of voltages and currents.



(c) Crystal presenting two steps lowering of conductivity. (d) Same crystal in a logarithmic plot.

**Figure 4.12** – In 4.12a a conductive crystal switched off at high voltage (red curve) and remained as such (black curve). In 4.12c a crystal had been turned on (red curve) and it exhibited two decremental current steps while sweeping voltage back to 0 V (black curve).

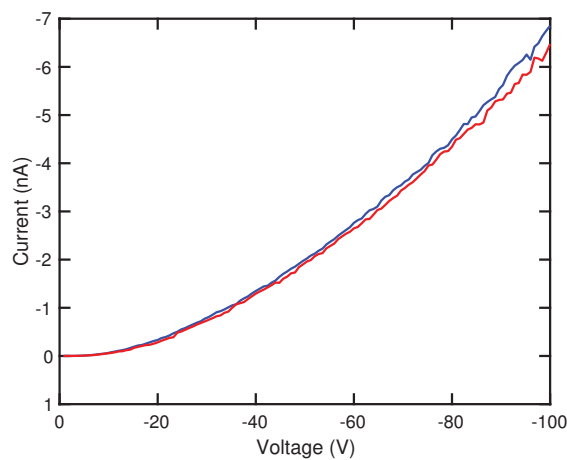


**Figure 4.13** – Comparison between the I-V characteristic of the same crystal measured with tungsten tip (blue curve) and beryllium-copper (red curve). No appreciable difference is observed.

## Chapter 4. Experimental results

**Table 4.2** – This table summarizes the switching mechanism for  $\text{Ag}_{44}(\text{FTP})_{30}$  crystals

Property	Appearance	Description	Example
Switch-on	Single change in conductivity	Most of the crystals that exhibited a sudden change in conductivity during voltage sweep remained for consecutive measurements in this high conductive state	4.7
	Lowering of threshold voltage	After relaxation, the crystals exhibited a lower voltage threshold	4.8
	Double change in conductivity	The same crystal changed to a high conductivity through a discrete number of jumps	4.9a
	Increase in conductivity for $V \rightarrow 0\text{V}$	The increase in conductivity occurred also during return sweep, that is $V \rightarrow 0\text{V}$	4.9c
	Dependence on the connection configuration	Crystals exhibited a lower threshold voltage when connected lengthwise rather than widthwise	4.10
Switch-off	Single drop in conductivity	Crystals, which had previously turned on, showed an inverse change in conductivity	4.11
	Double change in conductivity	The same crystal switched off through a discrete number of jumps	4.12c
	Voltage sweep dependence	Crystals went back to their initial state both for increasing and decreasing sweep voltages	4.12a

### 4.3.2 Temperature dependence

Experiments with varying temperature have also been conducted with the aim of elucidating the origin and nature of electron transport. The setups used to perform the electrical measurements were equipped either with a chuck that could be heated and cooled or with a peltier cell that had the same function. The temperature range in which the electrical properties could be studied was restricted to the stability of the crystals: above 70 °C either the organic ligands or the counterions were degraded and as result the crystal started to tarnish. As a result temperature was spanned in range from 15 °C to 60 °C. Most of the crystals showed a general trend of increased current for increasing temperatures, as shown in Figure 4.14, which is a typical signature of both variable hopping range (VHR) [127–130] and thermionic, field emission and trap-assisted tunnelling processes [18, 131, 132]. A detailed treatment of these mechanisms is presented in Appendix D.

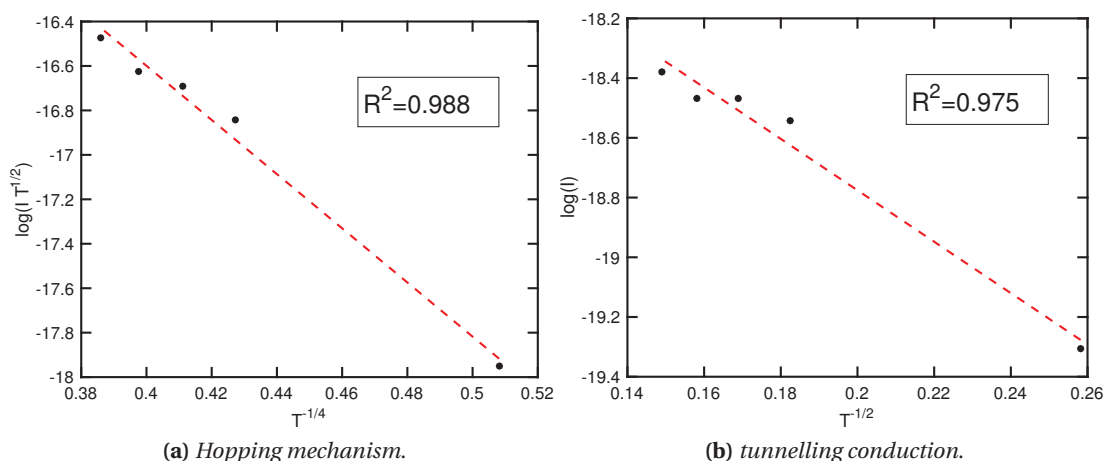


**Figure 4.14** – Fitting of the conductivity data of IBAN crystals with two different conduction mechanisms as in [133]: on the left a plot of  $\log(IT^{1/2})$  versus  $T^{-1/4}$ , based on hopping mechanism; on the right a plot of  $\log(I)$  versus  $T^{-1/2}$ , based on the field emission conduction mechanism. The lack of points is due to inconsistency of the temperature control reader.

Among all the crystals tested for varying temperature values, only three showed a repetitive switching mechanism. Before applying any voltage the crystals were left to thermalize and if they showed a jump in the current characteristic I waited ten minutes before proceeding with the measurement. The voltage threshold at which the current would drastically change seemed to lower for increasing temperature (Figure 4.15a), but consecutive tests on the same crystal had the effect of lowering the threshold, as previously seen in Section 4.3.1. Care has to be taken when interpreting the role of temperature in the switching mechanism, it is possible to assert that when the temperature was increased the threshold voltage diminished significantly more if compared to the effect consecutive measurements (see Figure 4.15a and 4.15b).

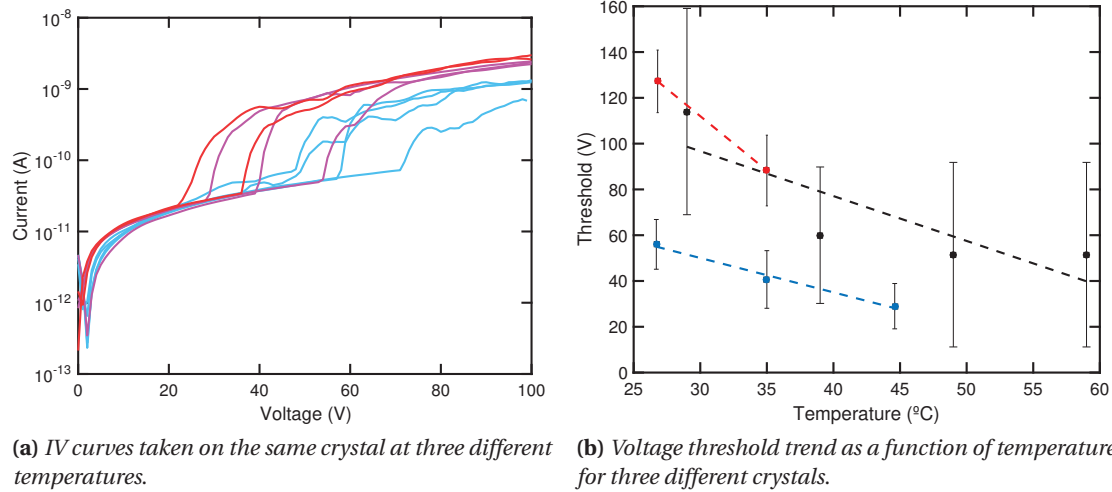


**Figure 4.15** – Figure 4.15a shows the position at which the same crystal exhibited a jump in conductivity. Curves of the same colour represent measurements done at the same temperature, being these temperatures: 27  $^{\circ}$ C, light blue, 35  $^{\circ}$ C, pink and 45  $^{\circ}$ C, red. The voltage values have been then averaged for the same crystal and the trend plot (Figure 4.15b) as a function of temperature for three different crystals. Error bars denote the standard deviation.

#### Four-terminal experiments

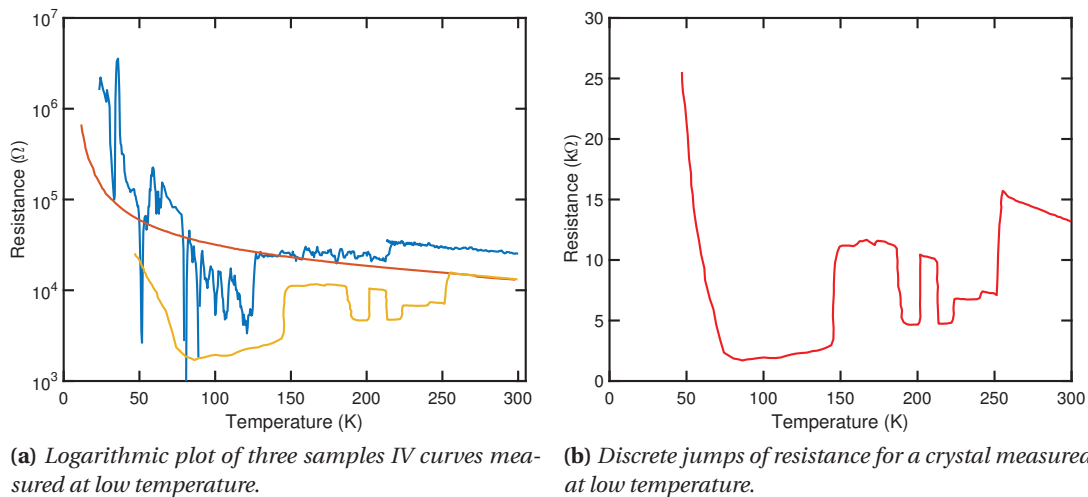


**Figure 4.16** – Figure 4.16a shows resistance curves for three different samples, that displayed discrete jumps of conductivity.

Four-terminal experimental have also been conducted on IBAN crystals. Given the reduced size, electrodes were nanofabricated with a FIB as described in 3.5.2. The four platinum leads were wire bonded to the electric circuit of the experimental apparatus, which was then cooled down to 10 K in a cryostat. Current was forced into the samples through two outermost platinum leads and the voltage measured through the two innermost. The calculated resistance



$R = \frac{V}{I}$  was then plotted as a function of varying temperature. Once again the main feature of the crystal, the switching mechanism, was present and appeared through discrete and sudden changes of resistance, as shown in Figure 4.16b. All crystals exhibited a general trend of lowered conductivity for lowering temperature (see Figure 4.16a), a signature typical of hopping and tunnelling. Despite their common trend with varying temperature, these two mechanisms are profoundly different [134]. Hopping is a thermally activated process. While electrons hop from one site to the other, they lose information about their phase, so hopping is an incoherent process and its probability depends exponentially only on the energy barrier between neighbouring sites [127, 128, 135]. In order to discern between the two transport mechanisms, we fitted our results as in 4.14. The VHR model proposed by Mott and Davis [136] found better agreement with our results. The dependence of resistance from temperature can also be expressed as  $R \approx \exp \frac{T_0}{T}^{-(d+1)}$ , where  $T_0$  is a temperature and  $d$  is the dimensionality of the transport. Figure 4.17a shows plots of  $\ln(R)$  versus  $T^{-\frac{1}{4}}$  ( $d=3$ ),  $T^{-\frac{1}{3}}$  ( $d=2$ ), and  $T^{-\frac{1}{2}}$  ( $d=1$ ) have  $R^2$  coefficients of 0.993, 0.997, and 0.994, respectively, suggesting that the electron transport in IBAN crystals is consistent with a 2D hopping mechanism. VHR fitting and the Arrhenius plot are shown in Figure 4.17.

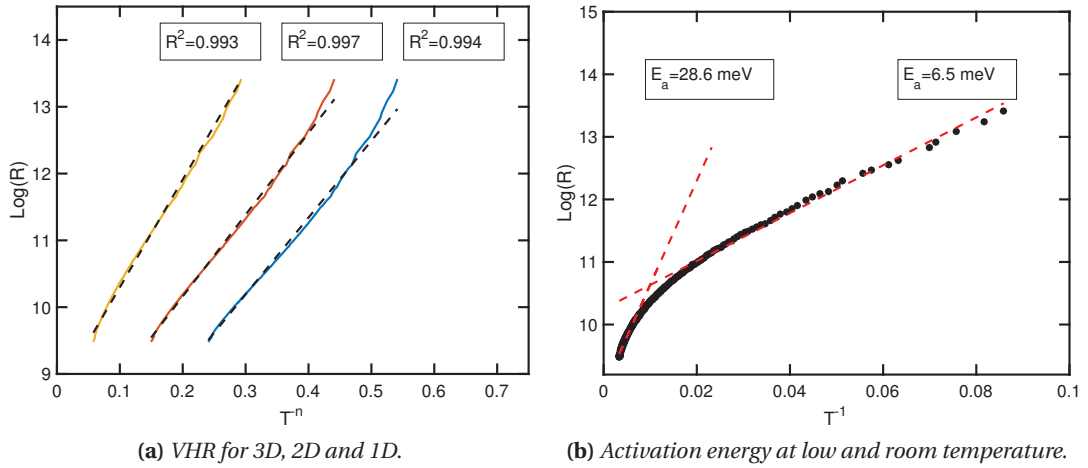


**Figure 4.17** – Figure 4.17a shows plots of  $\ln(R)$  versus  $T^{-\frac{1}{4}}$  ( $d=3$ , yellow curve),  $T^{-\frac{1}{3}}$  ( $d=2$ , orange curve), and  $T^{-\frac{1}{2}}$  ( $d=1$ , blue curve) have  $R^2$  coefficients of 0.993, 0.997, and 0.994 respectively, suggesting that the electron transport in IBAN crystals is consistent with a 2D hopping. The Arrhenius plot in 4.17b allowed us to determine the activation energy for transport. The presence of two activation energies suggests that the crystal behaves as an intrinsic material at high temperature, thus the charge carrier density is completely controlled by thermally activated carriers; at low temperature, this intrinsic contribution to the total charge carrier concentration is negligible, and it is overcome by carriers generated from impurities, which would explain the very low activation energy 6.5 meV, [137, 138].

Two activation energies were found,  $E_{a1}=28.6$  meV and  $E_{a2}=6.5$  meV at high and low temperature. This can be explained at high temperature by treating the crystal as an intrinsic material and the charge carrier density is completely controlled by thermally activated carriers; at low temperature the intrinsic contribution to the total charge carrier concentration is negligible,

## **Chapter 4. Experimental results**

---

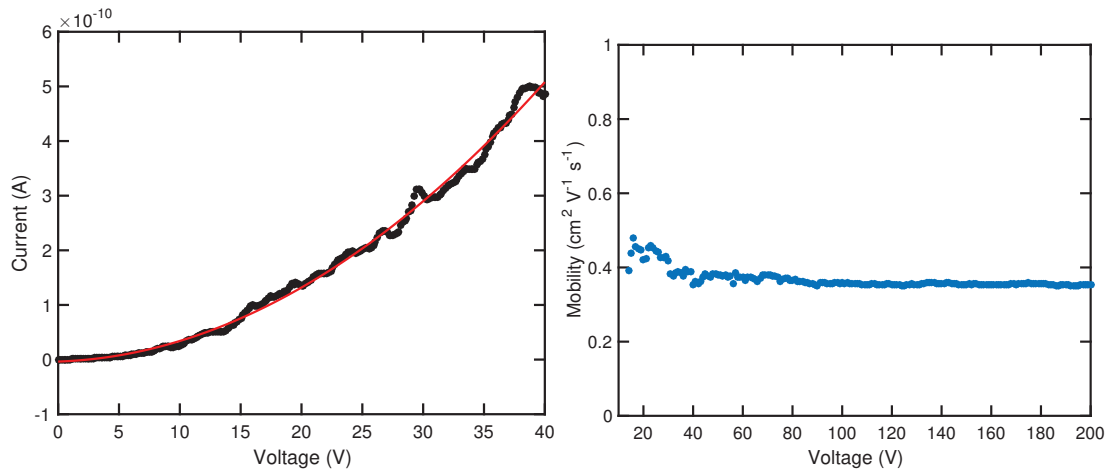
and it is overcome by carriers generated from impurities, which would explain the very low activation energy [137, 138].

### 4.3.3 Mobility calculation

The performances of semiconductors and organic semiconductors are very often evaluated in term of mobility. At a first glance, the mobility indicates how fast an electron or a charge particle moves when pulled by the electric field, as it links the drift velocity to the applied external electric field. In the field of organic electronic and organic solar cells, the mobility of amorphous silicon is often regarded as a benchmark for determining the electric performance of the molecule under examination: an organic semiconductor that presents a mobility higher than  $1 \text{ cm}^2 \text{ V}^{-1} \text{ s}^{-1}$ , that is the mobility of amorphous silicon [139, 140], is a good candidate for the realization of an electronic device [141]. The determination of charge carrier mobility has proven challenging [142, 143] and it is normally inferred by the current measured in the linear or saturation regime of a field effect transistor or using the Hall effect. Under certain circumstances [144] though, *i.e.* when the material current exhibits a quadratic dependence on the applied electric field, it is possible to extract the charge carrier mobility from a two-terminal experiment. Braga *et al.* [144] have demonstrated that it is possible to determine the charge carrier mobility of a bulk crystal for low conductive material by means of the space-charge limited current (SCLC) theory. This model, developed by Lampert [145], adapts well to poorly conducting material with localized electron trapping. In our case, assuming a contact area given by  $\pi R^2$ , where  $R$  is the tip radius, we observed that the current density  $J$  varied with the voltage squared, as shown in Figure 4.18a, so the relationship presented in [144] could be applied. It states that:

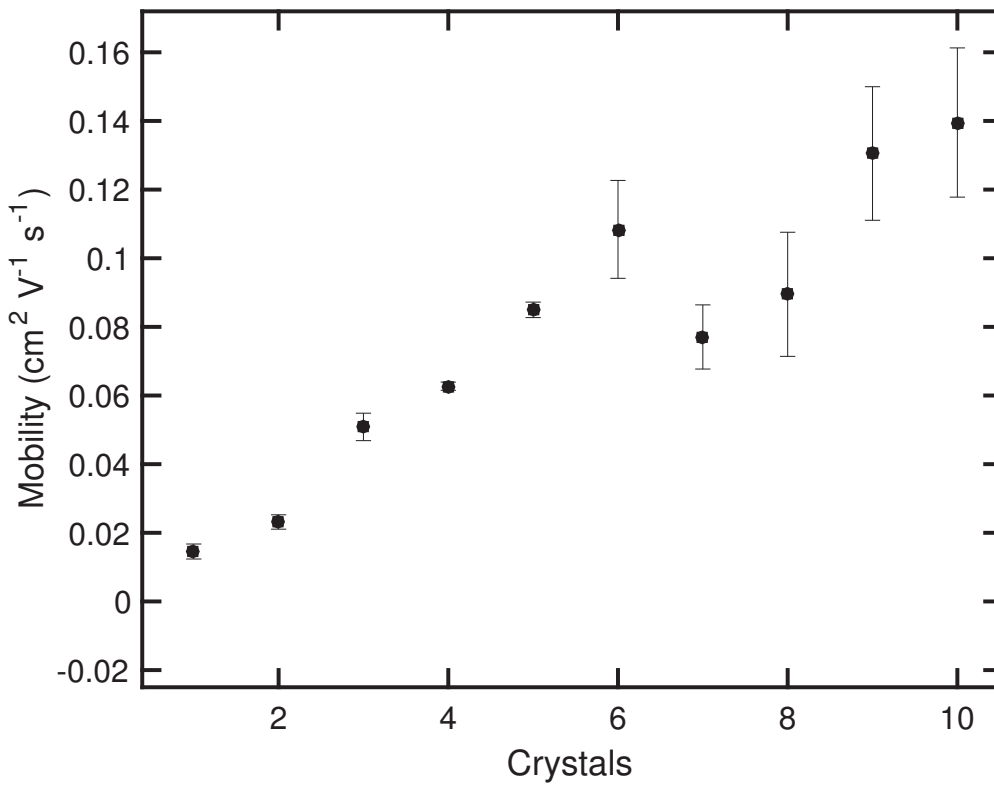
$$I \frac{L^2}{W} = \frac{9}{8} \epsilon_0 \epsilon_r \mu \frac{h}{L} V^2 \quad (4.3)$$

where  $L$  is the distance among the electrodes, the product  $W \times h$  is our contact area, so  $\pi R^2$ ;  $\epsilon_0$  and  $\epsilon_r$  are the vacuum and relative permittivity ( $\epsilon_r=2.83$  as measured in Appendix B);  $\mu$  is the magnetic permeability assumed to be equal to 1, and  $I$  and  $V$  are the measured current and applied voltage. Most of the crystals presented in their conductive state (see Figure 4.18a) a quadratic dependence on the applied voltage (equation 4.3). For each pair of data ( $I, V$ ) that satisfied the above mentioned relationship, the average mobility was calculated. The discrepancy from quadratic behaviour (see Figure 4.18b) appeared in the mobility calculation as deviation from a constant value. This spreading was taken into account as standard deviation of the mean value and plotted as error bars of the in Figure 4.18c. Typical values of mobility at room temperature ranged from  $10^{-2} \text{ cm}^2 \text{ V}^{-1} \text{ s}^{-1}$  to  $10^{-1} \text{ cm}^2 \text{ V}^{-1} \text{ s}^{-1}$ . In conclusion IBAN crystals possess a mobility, whose values are similar to those reported in literature for organic [143, 146]. Further investigation is required to establish whether processing improvements could lead to higher values of mobility.



(a) Quadratic fit for IV curve.

(b) Calculated mobility value for a crystal at high temperature.



(c) Mobility values for ten different samples.

**Figure 4.18** – Figure 4.18a shows an excellent quadratic fit of an IV curve of a conductive crystal. In case the quality of the fitting was good enough, the model presented by Braga [144] was applied to determine the mobility of the measured crystal, as shown in 4.18b. The mobility of ten good samples, with a small deviation from the quadratic behaviour are presented in Figure 4.18c.

#### 4.3.4 Cluster versus crystal property

The electric properties shown in Section 4.3.1 raised a series of questions on the origin of both the conduction mechanism and the switching mechanism. We were interested in understanding whether the observed behaviours were distinctive properties of the  $\text{Ag}_{44}(\text{FTP})_{30}$  cluster itself or rather of the crystal of clusters. For this reason we fragmented the crystals and we pressed the resulting crystalline powder to obtain a pellet of polycrystalline  $\text{Ag}_{44}(\text{FTP})_{30}$  clusters. We then chose pellets of sizes comparable to those of the measured crystals (see Figure 4.19a) and we tested them by sweeping a voltage across. The result showed that none of the features previously observed for IBAN crystals could be found in the pellet version of the cluster, neither the switching mechanism nor the same resistance trend (see Figure 4.19b). This experiment, repeated also on pellet obtained from uncrystallised IBAN and that led to similar results, showed us that dimensional ordering of the cluster is a requirement for the observation of the above mentioned characteristics, which resulted to be properties of the crystal rather than the clusters themselves.

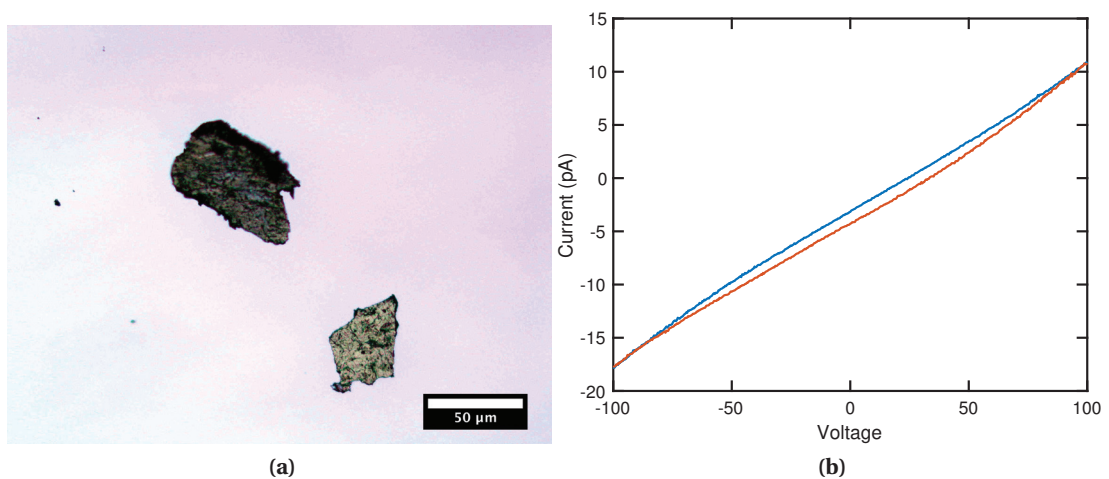


**Figure 4.19** – Pellet of clusters. In 4.19a a microscope image of two pellets from fragmented crystals of IBAN, with size comparable to those of crystals. In 4.19b a current-voltage relationship for a pellet, displaying currents significantly smaller than those of crystals.

### 4.4 Conductive AFM

In order to better understand what happened to the crystals at the nanoscale, we have conducted an *in situ* topographical analysis of crystals subjected to the application of an external electric field. These experiments have been realized with a conductive AFM (as described in Section 3.5.3), which was demonstrated [147–149] to be a powerful technique in studying the transport mechanism, the local surface, and the chemical modification of a material. Despite the potential offered by such technique, we could not exploit all its capability because of certain limitations. In our specific case the main limiting aspect was the range of voltages that could have been applied to the sample, which due to instrumental limitations was restricted to  $-10\text{ V}$  to  $10\text{ V}$ , very often too small to observe a change in conductivity of our crystals. Nonetheless we were able to observe in a very limited number of crystals the peculiar characteristics of IBAN crystals. Samples were prepared by gluing a crystal to a conductive substrate which acted as the positive or varying voltage electrode. The conductive iridium coated silicon tips were grounded, so the applied electric field was directed through the crystal from the substrate to the tip. The standard experimental routine was repeated as follows: firstly, a relatively smooth (typical roughness value was  $r_{RMS}=8.5\text{ nm}$ )  $2\text{ }\mu\text{m}^2 \times 2\text{ }\mu\text{m}^2$  area was chosen and its topography scanned (1 Hz) in AC tapping mode in order to cause the least damage to the crystal surface; then the tip was placed in contact with a specific position of the scanned area, a sweeping bias was applied from the substrate, at the tip of which the generated current was measured. If during the voltage sweep a change in current was observed then the same area would be scanned again, otherwise the tip would be moved to a new position. In Figure 4.20 we report sequential AFM scans of the same area prior to the application of a bias (green square) and after (red squares) having observed a change in conductivity. These scans represent a selection of forty consecutive scans taken over seven hours. It is evident from this image that the topography of the crystal surface changed not only underneath the position that corresponds to the point where the current measurement occurred (orange dot), but also in the area radially distributed around this position, and that it plateaued after ninety minutes. This effect can be observed by plotting the calculated roughness for each scan, after masking the lower part of the scan, versus time, as seen in Figure 4.21. After a drastic initial change the roughness stopped growing and reached a stationary value after ninety minutes.

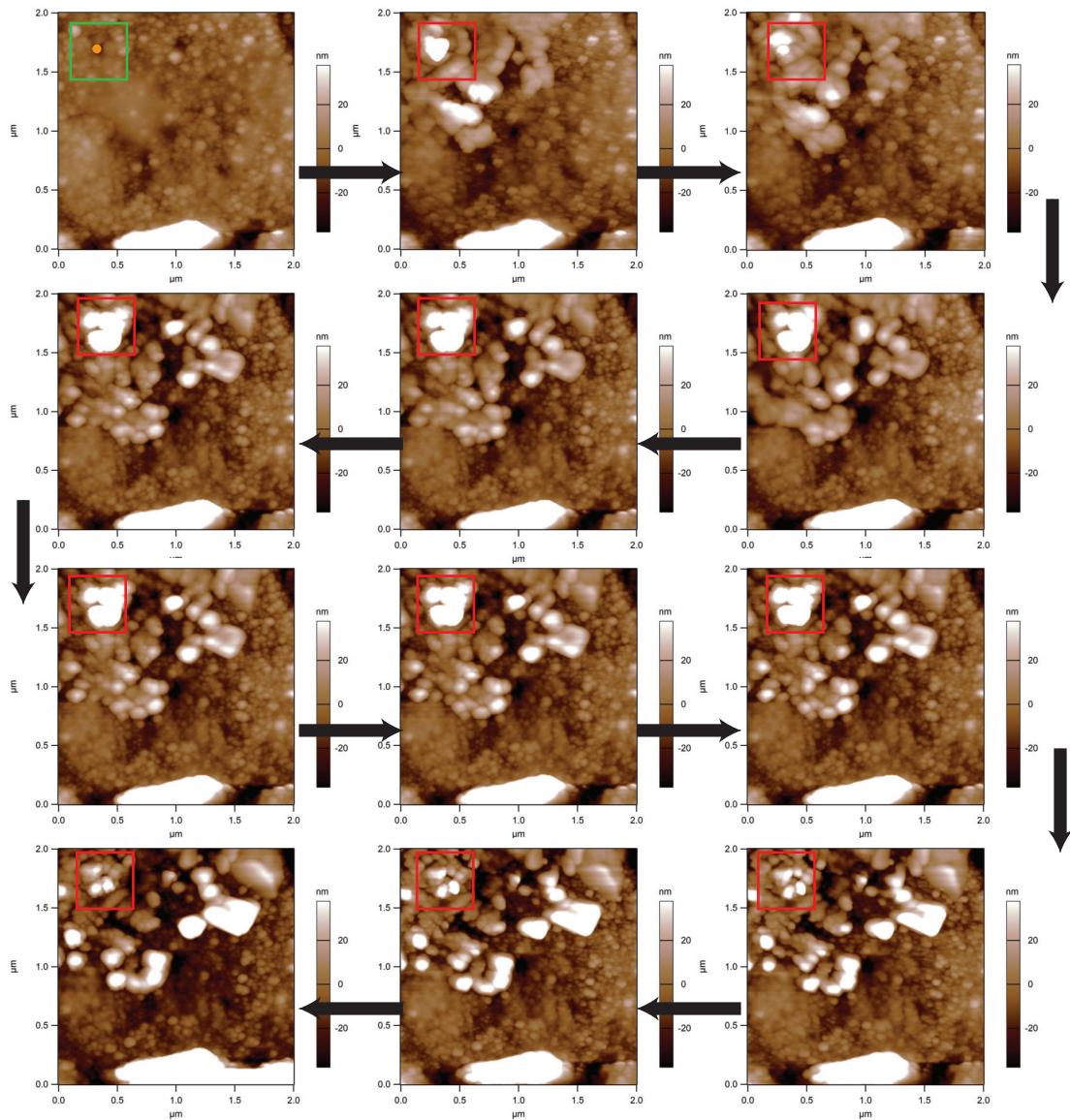


**Figure 4.20** – Sequential AFM non-contact scans over the same area prior to the application of a bias (green square) and after (red squares) having observed a change in conductivity. These scans represent a selection of forty consecutive scans taken over seven hours. Black arrows indicate the scan flow.

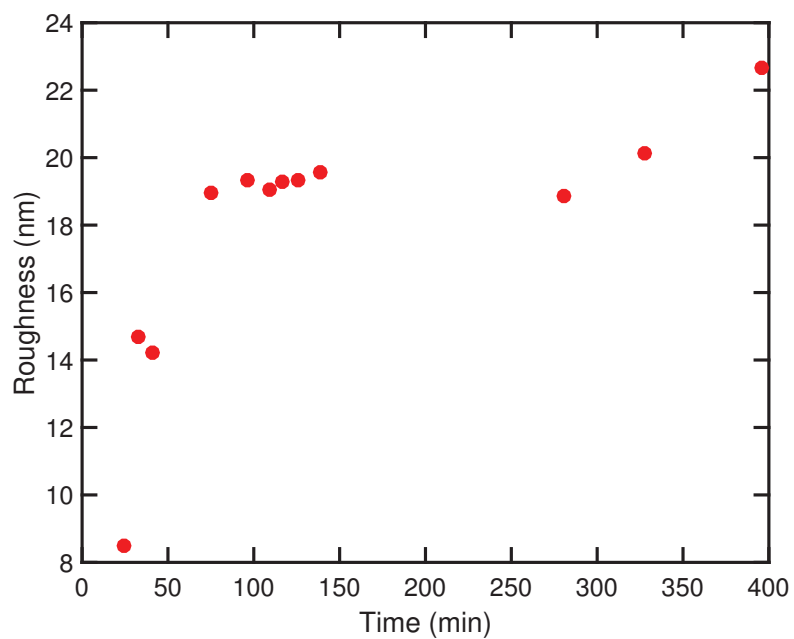


**Figure 4.21** – AFM roughness of a measured crystal over time. The initial roughness drastically changes before plateauing after 90 min.



## 4.5 XRD

The investigation of the change in conductivity needed a more profound understanding of the crystal structure. Although the full structure of  $\text{Ag}_{44}(\text{FTP})_{30}$  had been already reported by Yang [65], we wanted to study whether it was possible to attribute the change in conductivity to a modification of the IBAN crystal structure. For this purpose two similar crystals were taken from the same crystallisation batch: one was brought under the microscope, contacted with tungsten tips and sweeping high voltages were applied five times, in order to be sure that the crystal showed a higher conductivity (see Figure 4.22); the crystal was then disconnected, picked up with a cryoloop and quenched in liquid nitrogen. The other crystal was directly picked up and quenched, without its electrical properties to be tested. The samples were sent to PSI (Paul Scherrer Institute, Villigen, Switzerland) and the single crystal X-Ray diffraction patterns were measured at the X06DA (PXIII) macromolecular beamline, as described in section 3.4.2. The reflections of the two datasets were analyzed with SHELX and the structure refined with OLEX2 [150–152]. The refinement was carried out by Horst Puschmann (OlexSys Ltd, Chemistry Department, Durham University). The crystallographic data for the two solved structures are reported in table 4.3.

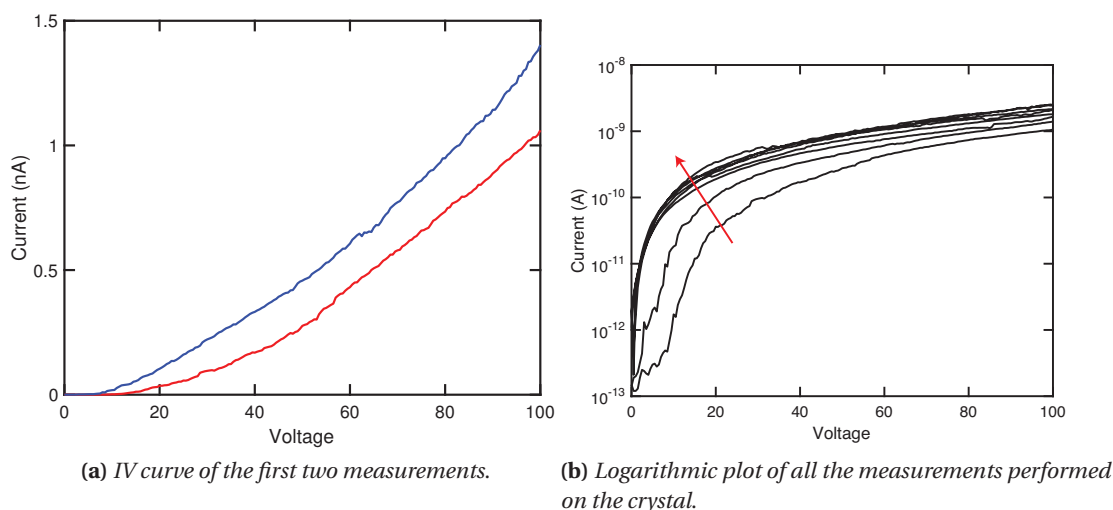


**Figure 4.22** – IV curves of consecutive measurements of a crystal prior to its characterization by single crystal XRD

**Unperturbed crystal** The resulting diffraction for the unperturbed crystal was calculated from three sets of unrelated frames, all not as strong as those for the crystal subjected to the external potential. Choosing the strongest run, a triclinic cell was found with 30% of the reflections fitting this cell. Concerning the quality of the reflection, the resulting data were weak ( $\frac{I}{\sigma} = 6.0$ ), and the internal R factor was found to be 10.45%. The completeness of the reflections at  $\lambda=0.79 \text{ \AA}$  was of 89%. The normalized structure factor  $E^2 = \frac{F^2}{\langle F^2 \rangle}$  determined a  $\langle |E^2 - 1| \rangle = 0.993$  resulted in a  $\text{P}\bar{1}$  space group, thus centrosymmetric. The asymmetric unit contained half  $\text{Ag}_{44}(\text{FTP})_{30}$  NC as well as two counterions (TPPB) and extensive disorder with

## Chapter 4. Experimental results

**Table 4.3** – This table summarizes the crystal data for  $\text{Ag}_{44}(\text{FTP})_{30}$

	<b>Crystal OFF</b>	<b>Crystal ON</b>
Formula	$\text{C}_{276}\text{H}_{200}\text{Ag}_{44}\text{F}_{30}\text{P}_4\text{S}_{30}$	$\text{C}_{276}\text{H}_{200}\text{Ag}_{44}\text{F}_{30}\text{P}_4\text{S}_{30}$
Density	$2.281 \text{ g cm}^{-3}$	$2.284 \text{ g cm}^{-3}$
$\mu$	$3.212 \text{ mm}^{-1}$	$3.423 \text{ mm}^{-1}$
Formula weight	9918.31	9918.31
Crystal system	triclinic	triclinic
Space group	$\text{P}\bar{1}$	$\text{P}\bar{1}$
a	20.4051 Å	20.82755 Å
b	20.8665 Å	22.60275 Å
c	21.9791 Å	30.95765 Å
$\alpha$	114.9564°	95.21730°
$\beta$	93.7561°	90.2599°
$\gamma$	116.4233°	96.4093°
Volume	$7219.0 \text{ \AA}^3$	$14420.94 \text{ \AA}^3$
Z	1	2
Z'	0.5	1
$\Theta_{min}$	1.773°	1.495°
$\Theta_{max}$	26.499°	27.500°
Measured refl.	90329	334938
Independent refl.	26749	56152
Reflections used	17338	47344
$R_{int}$	0.1045	0.0491
Parameters	2245	3457
Restraints	1728	0
Largest Peak	1.539	3.319
Deepest Hole	-1.711	-1.553
GooF	0.821	1.079
wR2 (all data)	0.2455	0.1436
wR2	0.2106	0.1390
R1 (all data)	0.1049	0.0507
R1	0.0686	0.0420

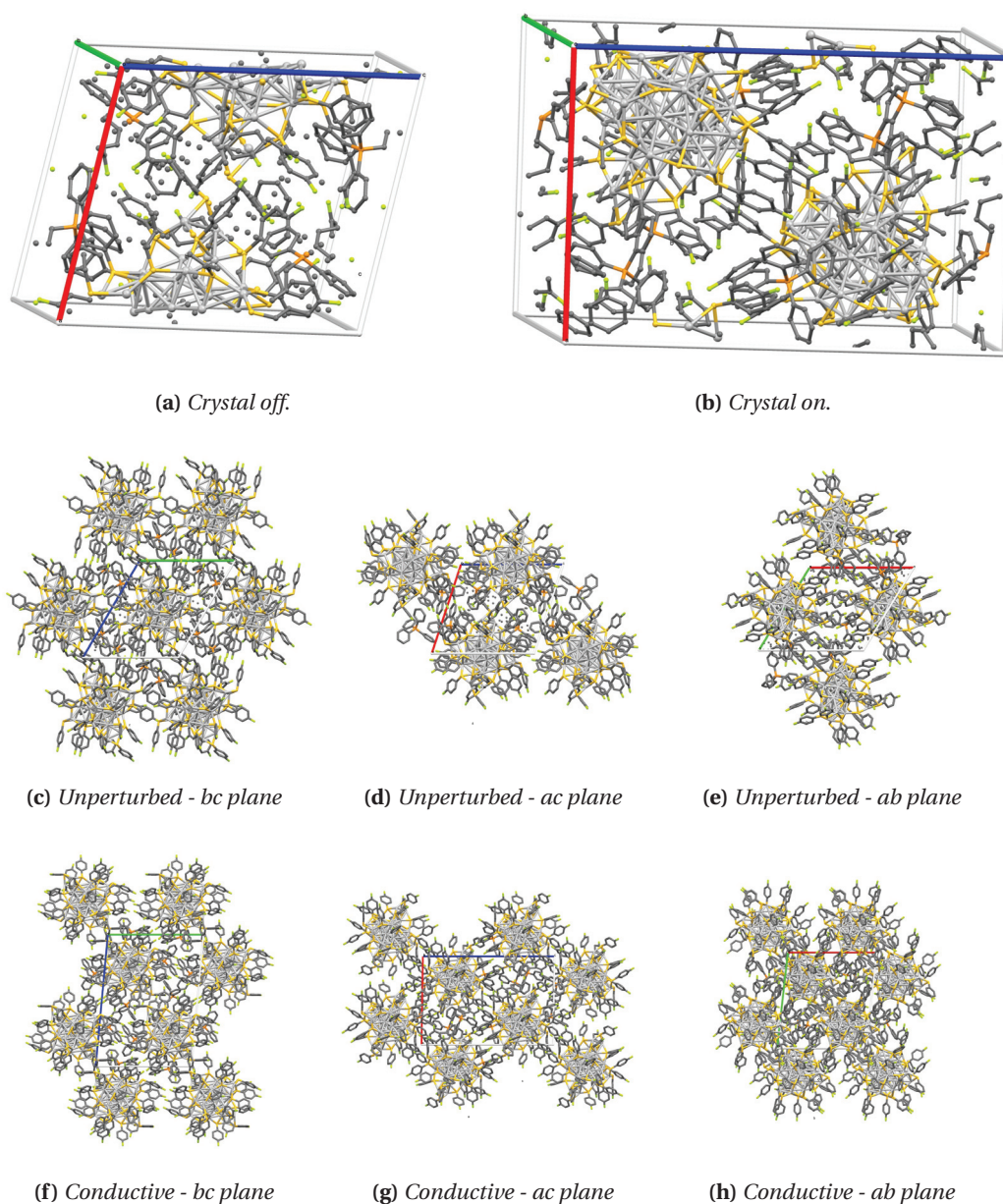


**Figure 4.23** – Unit cells of the refined structures. In 4.23a the unit cell of the unperturbed crystal. The unpaired dots represent disorder in the structure, with atoms having different occupancies; in 4.23b is represented the unit cell of the crystal subjected to an external field. Here two NCs per unit cell are present. The second row of images 4.23c, 4.23d and 4.23e contains the the unit cell of the off crystal viewed along the bc-, ac- and ab-planes; lastly, the third row (4.23f, 4.23g and 4.23h) contains the same projections for the crystal subjected to an external electric field.

FTP ligands having dual occupancies. Out of the 90329 reflections measured, 26749 were found to be unique ( $R_{int} = 0.1045$ ) and these were subsequently used in all calculations. The final weighted R2 was 0.2455 (all data) and R1 was 0.0686.

**Electrically conductive crystal** For this crystal two sets of unrelated frames were measured. Integration of either of the sets yielded good quality data, and it was possible to merge the two datasets in order to increase the overall coverage, at the expense of a slight increase of the internal R. In this case the determination of the triclinic unit cell was straightforward and unambiguous, with 98.3% of the reflections fitting the cell. The data resulting from these reflections were exceptionally good ( $\frac{I}{\sigma} = 21.7$ ), the internal R factor was 4.91% and the completeness to  $\lambda = 0.79 \text{ \AA}$  was 92%. The space group was again found to be centrosymmetric with  $\langle |E^2 - 1| \rangle = 1.117$ . Compared to the previous unit cell, there was a whole molecule as well as four counterions present in the asymmetric unit. Interestingly, disorder was not present in this structure. Regarding the refinement, out of the 334938 reflections measured 56152 were found unique ( $R_{int} = 0.0491$ ) which were used in all calculations. The final weighted R2 was 0.1436 (all data) and R1 was 0.0420.

The two unit cells were significantly different (see Figure 4.23), with the difference in size being the most striking result: the volume of unit cell of the crystal subjected to the electric field was found to be twice that of the unperturbed crystal, accommodating 1168 atoms, an incredibly large amount of atoms for molecular crystals. Nonetheless, thanks to a minimization algorithm that calculated the Ag–S–Ag angles for the six  $\text{Ag}_2\text{S}$  units described in Figure 2.6, we were able to identify an overlay pattern for the two crystal lattices, so that the metallic core of the NCs were sitting on the same lattice sites. The overlay can be seen in Figure 4.24, where the two unit cells have been grown in all the direction until they overlapped. In these overlays, the metallic silver cores together with the  $\text{Ag}_2\text{S}$  motifs of the perturbed and unperturbed structures are represented in blue and orange respectively. The overlapping atoms do not show a significant shift, being the maximum atomic displacement calculated smaller than the diffraction wavelength,  $d_a = 0.568 \text{ \AA} < \lambda = 0.79 \text{ \AA}$ . A substantial difference is present in the decorating FTP ligands and in the TPPB counterions. In this case, the FTP ligands exhibit either a bending of the whole structure or a rotation of the phenyl ring. Notably, this change was accompanied by the tilting of a facing counterions. An example of this is shown in Figure 4.25.

### 4.5.1 Reproducibility

In order to confirm the XRD results, the structure of approximately one hundred crystals was measured, both unperturbed and switched. Half of the crystals were measured with the aforementioned synchrotron source. Unfortunately, the outcome of these diffraction experiments coincided always with the structure corresponding to the unperturbed structure. The unit cell was found to be the same in all cases within the experimental error, and the disorder was always present. At the beginning, I was discouraged by the possible presence of polymorphs among the  $\text{Ag}_{44}(\text{FTP})_{30}$  crystals, but as the number of diffraction experiments increased and the only unit cell found was that of the unperturbed structure, it became reasonable to suppose that the irreproducibility could have come from experimental procedure. As described in Section 4.3.1, crystals remained in the switched state for a limited amount of

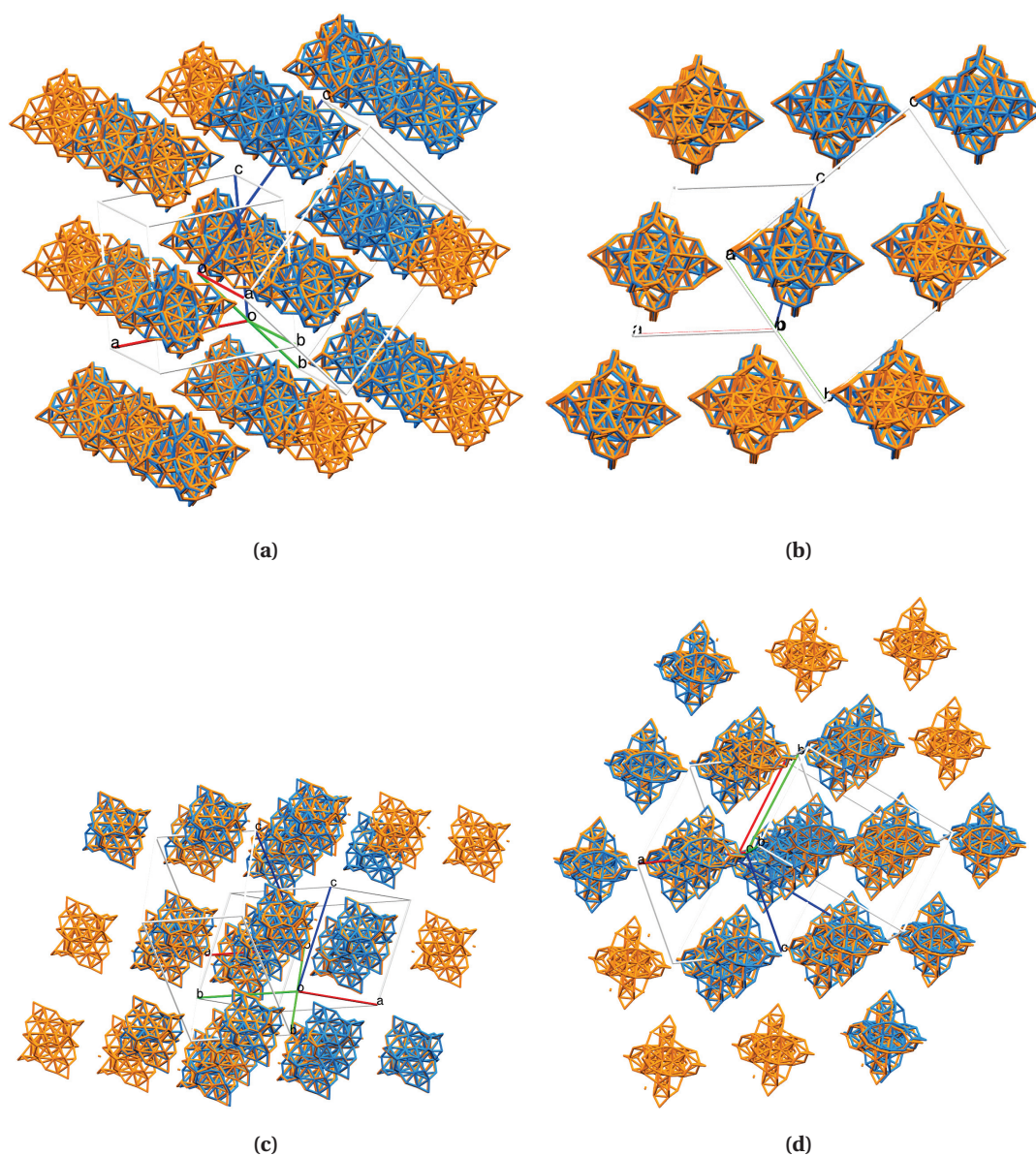


**Figure 4.24** – Overlay of the two crystal lattices. The unperturbed structure is represented by orange atoms, the other with blue atoms. The metallic core as well as the  $\text{Ag}_2\text{S}$  units do not show a significant shift, with the maximum atomic displacement being smaller than the diffraction wavelength.

time. In the process of picking up crystals, after the application of a voltage, there was a lag of time between the disengagement of the probes and the pick-up, typically a couple of minutes, in which the crystal had time to relax back to the unperturbed structure. The counterions and ligands are able to move and vibrate even after shock-freezing at 77 K, therefore it seems reasonable to presume that the unique crystal that showed a different structure might have been pinned in its perturbed state by an external factor or by a combination of factors, such as the pressure induced by water molecules adsorbed on the surface or residual stress induced

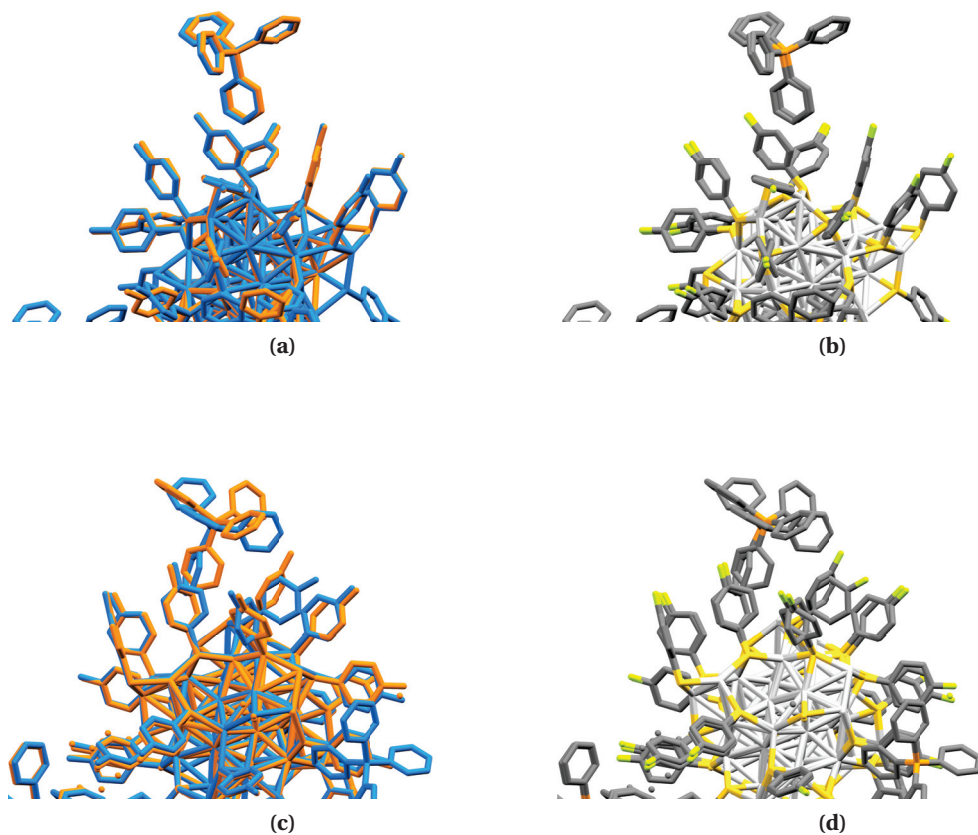


**Figure 4.25** – Modification of the decorating motifs of  $\text{Ag}_{44}(\text{FTP})_{30}$ . The unperturbed structure is represented by orange atoms, the other with blue atoms. The full overlay coincides precisely with the counterions not moving (Figure 4.25a and 4.25b), while when the counterions move, the facing FTP ligands bend and rotate to accommodate the shifting of the former (Figure 4.25c and 4.25d)

by the tip. These external factors are not easy to reproduce. A different experimental approach, such as *in situ* XRD, may remove all the doubts.

## 4.6 A polymorph

A polymorph was indeed found, but never in the same crystallisation batch. In the process of crystallising IBAN, we tested different solvent-antisolvent binary systems. The results reported so far were obtained, as described in 3.3, used DCM and hexane. Only one other solvent couple led to the crystallisation of a different polymorph, namely acetone and hexane. The use of these solvents led to crystals of slightly bigger dimensions compared to those crystallised from DCM-hexane (see Figure 4.26 and 3.2) with a higher occurrence of twinned crystals.

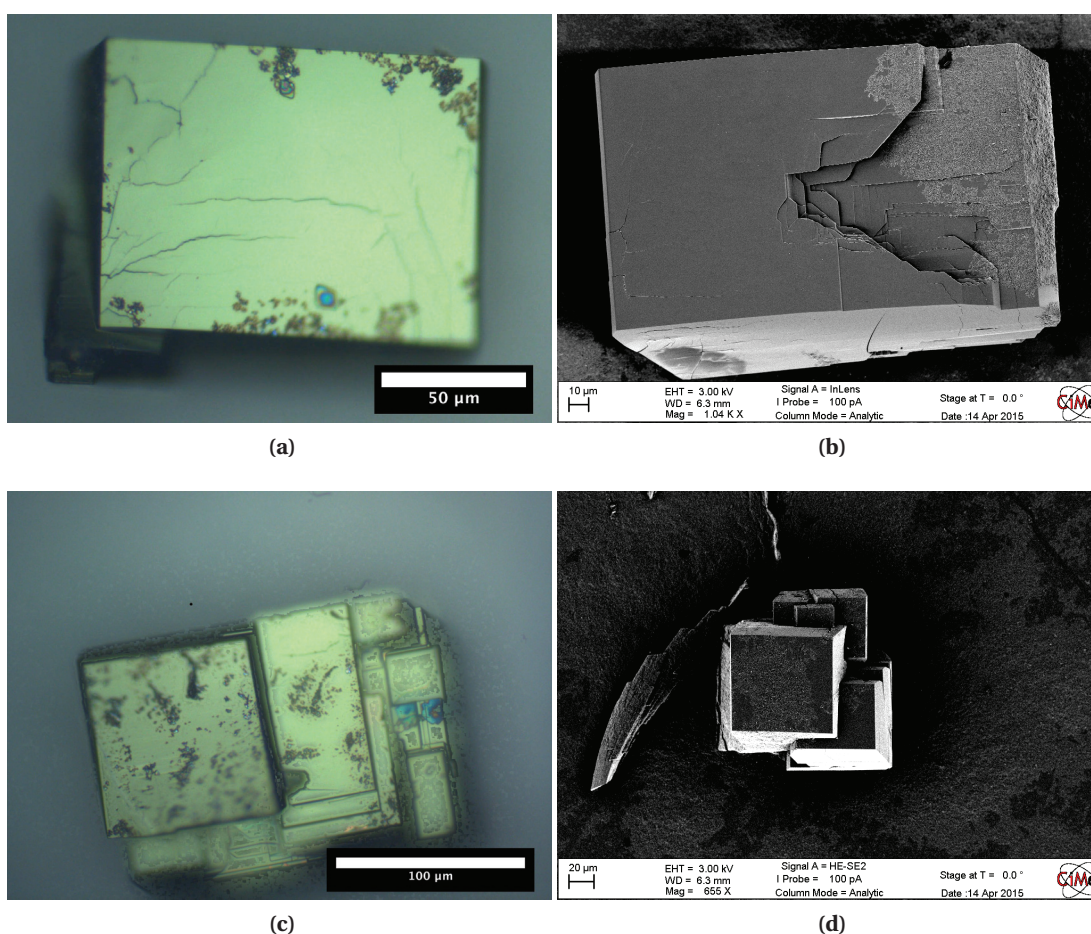


**Figure 4.26** – Examples of the polymorph obtained through acetone-hexane crystallisation. Figures 4.26a and 4.26c show microscope image of this polymorph, while 4.26b and 4.26d show SEM images.

### 4.6.1 Electrical testing

These crystals exhibited different electric properties than the ones mentioned in Section 4.3.1: their conductivity, in the voltage span tested (–100 V to 100 V), did not show a dramatic increase and even at high voltages the current hardly ever exceeded the nanoampere range.

## Chapter 4. Experimental results

This behaviour can be observed in Figure 4.27, where two crystals have been subjected to an external electric field: during the voltage sweep of Figure 4.27a (Figure 4.27b in logarithmic scale) there seemed to be a change in conductivity which resembled that of  $\text{Ag}_{44}(\text{FTP})_{30}$  crystals originated from DCM-hexane (see Figure 4.7).

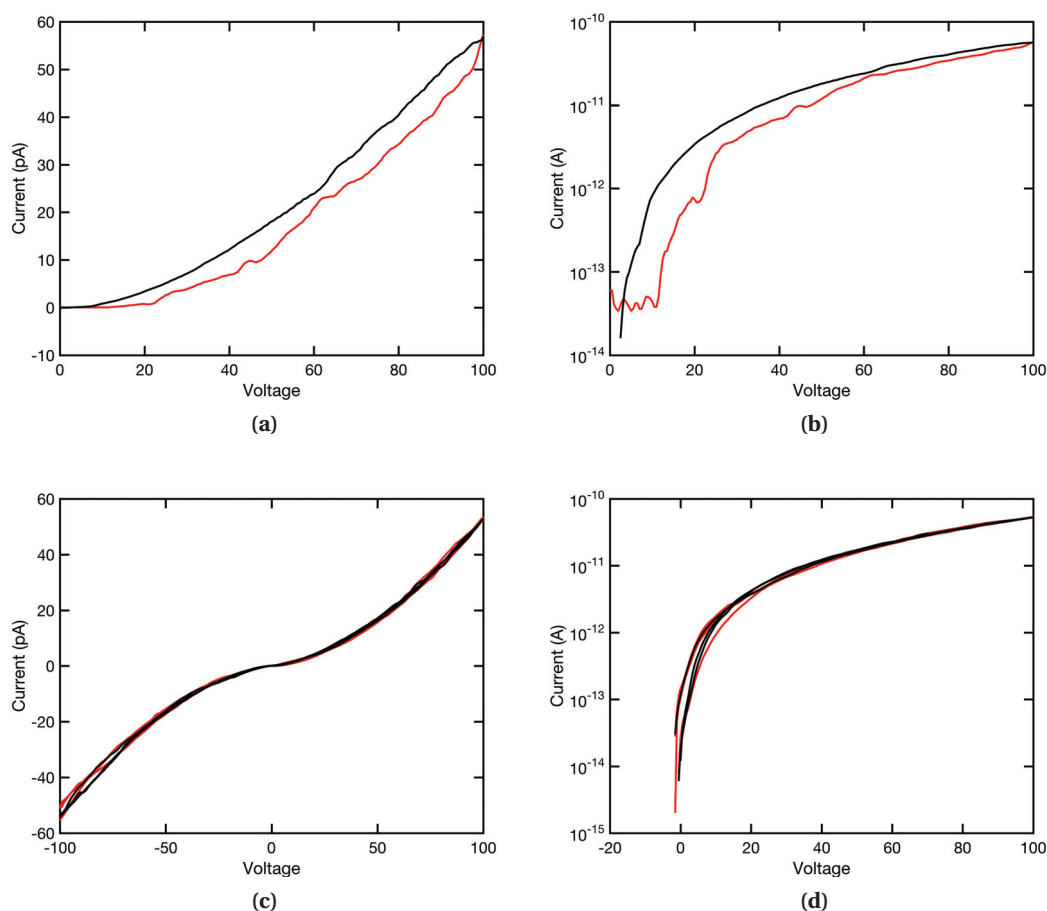


**Figure 4.27** – I(V) characteristics of the polymorph obtained from acetone-hexane crystallisation. In the voltage span tested ( $-100\text{ V}$  to  $100\text{ V}$ ), these crystals did not show a dramatic increase (Figure 4.27a and 4.27c). During the voltage sweep of Figure 4.27a (Figure 4.27b in logarithmic scale) there seemed to be a change in conductivity which resembled that of  $\text{Ag}_{44}(\text{FTP})_{30}$  crystals originated from DCM-hexane (see Figure 4.7).

A comparison between the two crystallised polymorphs is shown in Figure 4.28, where it is possible to appreciate the difference in conductivity, with that of the new crystals being lower than two orders of magnitude. While in the original polymorph is clearly possible to define a threshold voltage after which the conductivity drastically increases, in the other polymorph a small kink is the only footprint of a weak change in conductivity. One possible reason why these crystals did not exhibited a big change might be found in the range of applied voltages, which was not sufficiently high to cause a larger increase in conductivity.



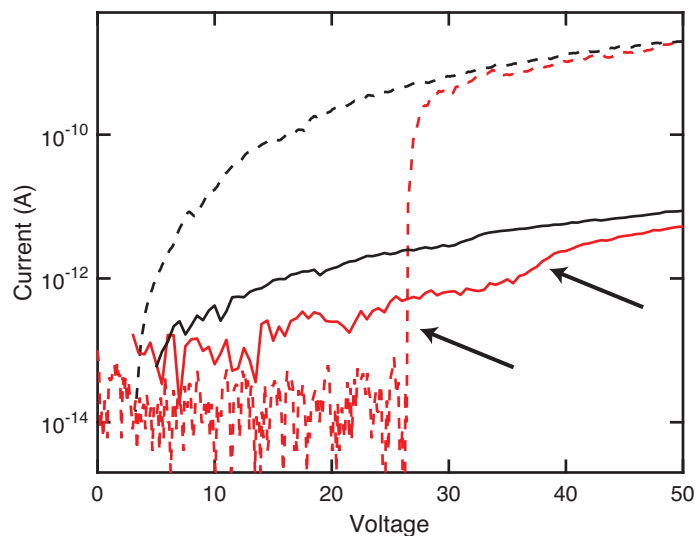


**Figure 4.28** – A comparison of the electrical characteristics for two different samples crystallised by vapour-vapour diffusion of DCM-hexane (dashed red and black lines) and acetone-hexane (solid red and black lines). The two arrows point at the change in conductivity for the respective crystal. The crystal obtained from the former couple of solvents shows a drastic change of conductivity, while that crystallised with the latter exhibit a small kink

#### 4.6.2 Polymorph XRD characterization

Crystals from the same batch had been taken for single crystal XRD experiments, with and without being subjected to an external electric field. The result for two crystals are reported in Table 4.4

**Unperturbed crystal polymorph** The resulting diffraction for the unperturbed polymorph crystal was calculated from two excellent sets of unrelated frames. A triclinic cell was found. The internal R factor was found to be 2.87%. The normalized structure factor resulted in a  $P\bar{1}$  space group, thus centrosymmetric. The final weighted R2 was 0.2352 (all data) and R1 was 0.0714.

**Crystal polymorph after biasing** The crystal polymorph obtained by acetone-hexane crystallisation, subjected to an electric field, showed excellent diffraction patterns. The internal R factor was 1.09%. The space group was again found to be centrosymmetric. The final weighted R2 was 0.1018 (all data) and R1 was 0.0373.

## Chapter 4. Experimental results

**Table 4.4** – This table summarizes the crystal data for Ag<sub>44</sub>(FTP)<sub>30</sub> polymorph obtained through vapour vapour diffusion of acetone and hexane

	<b>Crystal OFF</b>	<b>Crystal ON</b>
Formula	C <sub>276</sub> H <sub>200</sub> Ag <sub>44</sub> F <sub>30</sub> P <sub>4</sub> S <sub>30</sub>	C <sub>276</sub> H <sub>200</sub> Ag <sub>44</sub> F <sub>30</sub> P <sub>4</sub> S <sub>30</sub>
Density	2.193 g cm <sup>-3</sup>	2.182 g cm <sup>-3</sup>
$\mu$	3.142 mm <sup>-1</sup>	3.344 mm <sup>-1</sup>
Formula weight	9740.74	9692.7
Crystal system	triclinic	triclinic
Space group	<b>P<math>\bar{1}</math></b>	<b>P<math>\bar{1}</math></b>
a	21.2671 Å	21.30960 Å
b	21.4442 Å	21.43680 Å
c	21.4382 Å	21.47450 Å
$\alpha$	95.8840°	95.9470°
$\beta$	118.0720°	113.6490°
$\gamma$	113.5990°	118.2190°
Volume	7375.99 Å <sup>3</sup>	7376.73 Å <sup>3</sup>
Z	1	1
Z'	0.5	0.5
$\Theta_{min}$	1.132°	1.140°
$\Theta_{max}$	20.746°	21.386°
Measured refl.	28135	47766
Independent refl.	13412	14571
Reflections used	12404	14331
R <sub>int</sub>	0.0287	0.0109
Parameters	1738	1720
Restraints	0	0
Largest Peak	2.151	2.897
Deepest Hole	-1.378	-1.5563
GooF	1.1372	1.051
wR2 (all data)	0.2352	0.1018
wR2	0.2334	0.1015
R1 (all data)	0.0758	0.0377
R1	0.0714	0.0373

# 5 Discussion

## 5.1 Chapter outline

In this chapter I comment on the results presented in Chapter 4. The investigation of the conduction mechanism in silver NC crystals represents a novelty in this field, and more in general in the field of metal NCs. To the best of my knowledge no attempts of studying the electrical properties of IBANs or any other crystals of clusters have been done, and that is why I strongly believe that this thesis will pave the way to new interesting properties, that will hopefully lead to new applications. Starting from the analysis of the conduction mechanism that I observed in the crystals of IBAN, I present analogies found in the literature that help in explaining the complex electrical behaviour of the crystals. The focus then moves to the analysis of the switching mechanism and to its interpretation as a phase transformation. Examples of other switching mechanisms are shown in order to find similarities, as well as differences, between the phenomenon described in this thesis, and other examples of materials that exhibit a change in conductivity, without necessarily undergoing a phase transition.

## 5.2 Analysis of the crystal conduction

Since the very beginning of their discovery, metal NCs have attracted attention because of their exotic properties. The electronic structure (see Chapter 2) and the quantized nature of this material seemed to be ready to be exploited when the first crystals were made, but the handling and processing of this material revealed that extra care had to be taken. Crystals' dimensions and chemical stability affected and strongly limited the choice of fabrication methods that would have allowed the investigation of the electric properties of this NC crystals. These complications explain why, to the best of my knowledge, there are no experiments that try to investigate the electrical behaviour of NC crystals under the application of an external electric field. Therefore, in order to comment on the experimental observations presented in Chapter 4, I discuss the mechanisms that have been found in similar systems, such as NP networks,

metallic supracrystals or, more generally, in poorly conducting systems. There is a vast amount of literature on the field so I decided to focus on those mechanisms that show either structural or electrical similarities with NCs. The details of the mechanisms presented are exhaustively described in Appendix D.

I have identified three concurrent mechanisms that have a role in the electronic conduction of IBAN crystals: Schottky emission, hopping and tunnelling. All these three mechanism have been extensively studied in solid-state physics, where they produce a current of electrons through an insulating barrier in metal-oxide-semiconductor or in metal-oxide-metal structure respectively [138]. Moreover, the electric conduction of polymers and disordered materials has also been explained in terms of the three aforementioned mechanisms [134, 135, 153]. Our crystals cannot be categorized in any of these categories and the reason why these conduction models apply to  $\text{Ag}_{44}(\text{FTP})_{30}$  crystals is uniquely a consequence of the quantized nature of their electronic density of state and its localization, because thermionic emission, hopping and tunnelling occur within localized states.

### 5.2.1 Schottky emission

Schottky emission is a thermally activated process where electrons overcome an energy barrier, which is lowered by an applied voltage. The expression for the generated field current is:

$$J_{SE} = A^* T^2 \exp \left[ \frac{-q (\phi_b - \sqrt{qV/4\pi\epsilon_i w})}{k_b T} \right] \quad (5.1)$$

where  $A^* = \frac{4\pi q m_{eff} k_b^2}{h^3}$  is the effective Richardson constant,  $T$  is the absolute temperature,  $q$  is the electronic charge,  $\phi_b$  is the energy barrier height,  $V$  is the applied voltage,  $w$  is the thickness and  $\epsilon_i$  is the permittivity of the insulating material,  $m_{eff}$  is the effective mass,  $h$  is the Planck's constant and, lastly,  $k_b$  is Boltzmann's constant. This equation holds for two electrodes separated by an insulator of width  $w$  and permittivity  $\epsilon_i$ , which is not the case for  $\text{Ag}_{44}(\text{FTP})_{30}$  clusters. The equation needs to be readjusted assuming that a new length  $w$ , that represents the distance among the final and initial position of the emitted electrons, and a corrected value for the permittivity  $\epsilon_i$  could be replaced in Equation 5.1. Under this assumption, it is possible to fit the measured characteristics under constant temperature and for fixed applied electric field. The results are shown in Figure 5.1 and appear to scale well with the Schottky relationship for temperature and applied voltage. It seems reasonable to conclude that, among the contributions to the total current measured in IBAN crystals, Schottky emission contributes at least in the temperature range 238 K to 300 K, and at low biasing [154] regimes ( $V_{app} < 5\text{V}$ ). Further investigation into higher temperature range is required, given the strong dependence of this effect on  $T$ , to better ascertain the presence of this mechanism.

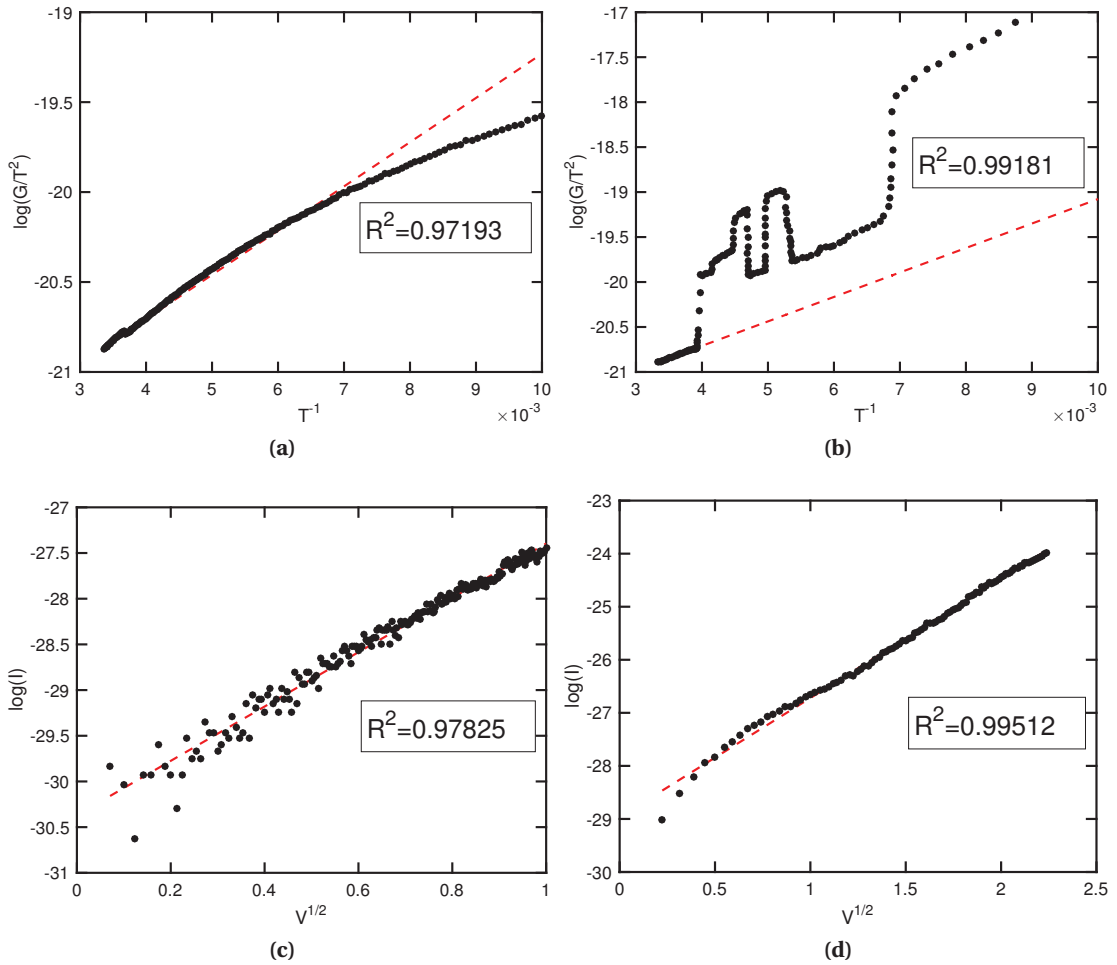


**Figure 5.1** – Figure 5.1a presents a fitting of the results shown in Figure 4.16a with the expression for Schottky emission at constant electric field. The fitting appears satisfactory exclusively at high temperature, *i.e.* 238 K to 300 K. Another measurement, which corresponds to the results presented in Figure 4.16b, shows again that around room temperature Schottky emission contributes to the total measured current. Figures 5.1c and 5.1d present a fitting of the results presented in Figure 4.6, which described the non-linear behaviour of an IBAN crystals at low voltages. At low biasing condition, under constant temperature, the model proposed by Schottky shows good agreement with our observations.

### 5.2.2 Hopping

The theory of VHR, proposed by Mott and Davis [155] and revisited by Efros and Shklovskii in the case of Coulomb interaction, is another thermally activated mechanism used to describe systems with localized charge-carrier states. VHR differs from nearest hopping range (NHR), because electrons, rather than hopping to the nearest available site, hop into sites further away, which possess lower energy. Among the other mechanisms, VHR has been applied successfully as a model to several experimental observations of electric properties of FeAu and FePt NPs [129], dodecanethiol Au NPs [156] and AuNP supracrystals [157], as well as

in molecular systems [28, 158–160]. The four-terminal results presented in Section 4.3.2 unambiguously showed that an increase of resistance for decreasing temperature, feature typical of disordered systems exhibiting hopping mechanism. The exponential dependence on temperature can be adjusted by the dimensionality of the hopping (for details see Appendix D). The general expression [161, 162] that accounts for Coulomb interaction is given by:

$$\sigma = \sigma_0 \exp \left[ \left( \frac{T_0}{T} \right)^p \right] \quad (5.2)$$

where  $p = \left[ \frac{n+1}{n+1+d} \right]$ ,  $d$  is the dimensionality and  $n=0, 1$  and  $2$  is the power of the density of state power-law. For the experiment presented in Section 4.3.2, I found good agreement for  $n=2$  and  $d=2$ , as anticipated in Figure 4.17a. These results are shown in Figure 5.2 for  $R_0 = 8.5 \text{ k}\Omega$  and  $T_0 = 150 \text{ K}$ .

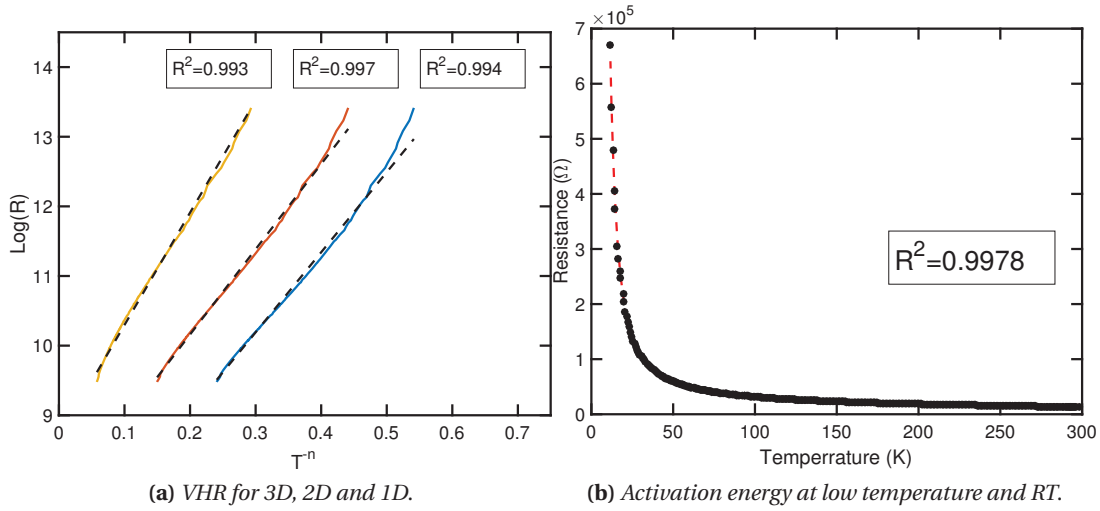


**Figure 5.2** – Figure 5.2a shows plots of  $\ln(R)$  versus  $T^{-\frac{1}{4}}$  ( $d=3$ , yellow curve),  $T^{-\frac{1}{3}}$  ( $d=2$ , orange curve), and  $T^{-\frac{1}{2}}$  ( $d=1$ , blue curve) have  $R^2$  coefficients of 0.993, 0.997, and 0.994 respectively, suggesting that the electron transport in IBAN crystals is consistent with a 2D hopping mechanism. Figure 5.2b shows the same result plotted with the exponential presented in Equation 5.2.

### 5.2.3 Tunnelling

The main difference between tunnelling and others mechanism that involve the overcoming of a potential barrier is that tunnelling is a coherent process. Coherence means that electrons preserve, under certain conditions, their phase. This property can lead to phenomena such as resonant tunnelling, the working principle of devices like resonant tunnelling diode (RTD).

Under the effect of an external potential, tunnelling can be divided into direct tunnel (DT) and Fowler-Nordheim tunnel (FN), as shown in Figure 5.3 (see Appendix D). The transition from DT to FN depends on the barrier height, width and the applied potential, and it can be

approximated as the transition from a rectangular to a triangular shaped barrier. Moreover the transition can be biased by the presence of a gate, which has the effect of reducing the effective potential barrier height.

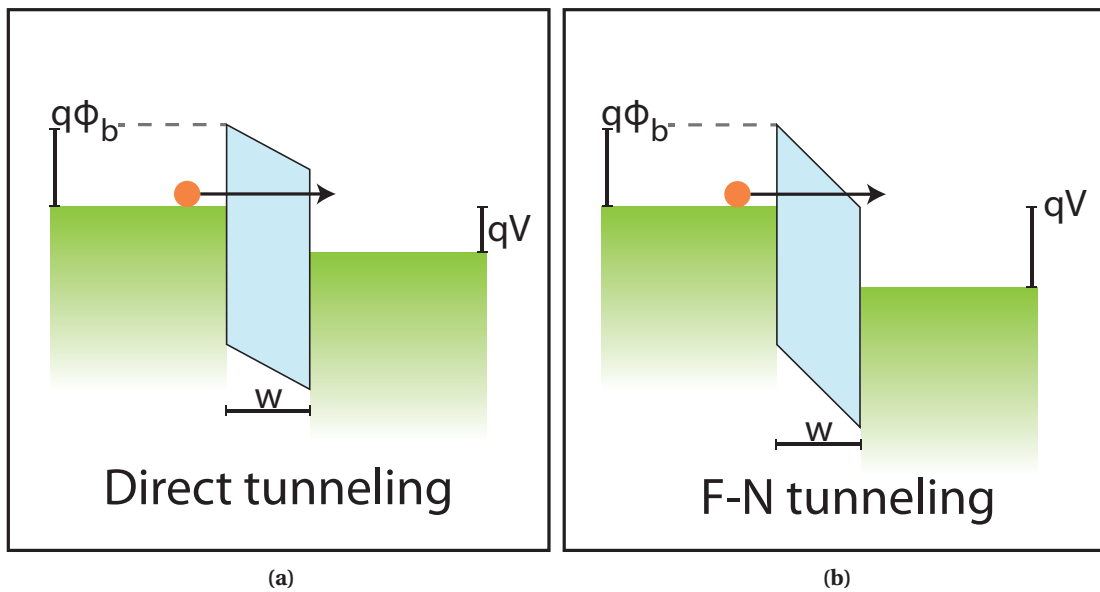


**Figure 5.3** – Tunnelling mechanisms. In 5.3a band diagram schematic for direct tunnel. The tunnelling probability decreases exponentially for increasing width and barrier height, while when voltage high enough to tilt the band is applied, the effective barrier width is diminished, as shown in 5.3b

The expression for tunnelling current is given by:

$$J_T \propto V \exp \left[ -\frac{4w \sqrt{2m_{eff}} (q\phi_b)^{\frac{3}{2}}}{3q\hbar V} \right] \quad (5.3)$$

where  $q$  is the electronic charge,  $\phi_b$  is the energy barrier height and  $w$  its width,  $V$  is the applied voltage,  $m_{eff}$  is the effective mass,  $\hbar$  is the Plank's constant. In a so-called Fowler-Nordheim plot, which linearises Equation 5.3, it is possible to discriminate DT and FN mechanisms by looking at the point of inflexion of the curve. The presence of this transition has already been demonstrated for molecular transistors and in single-molecule conductance experiments [163]. The FN plot of the results presented in Section 4.3.1 are shown in Figure 5.4.

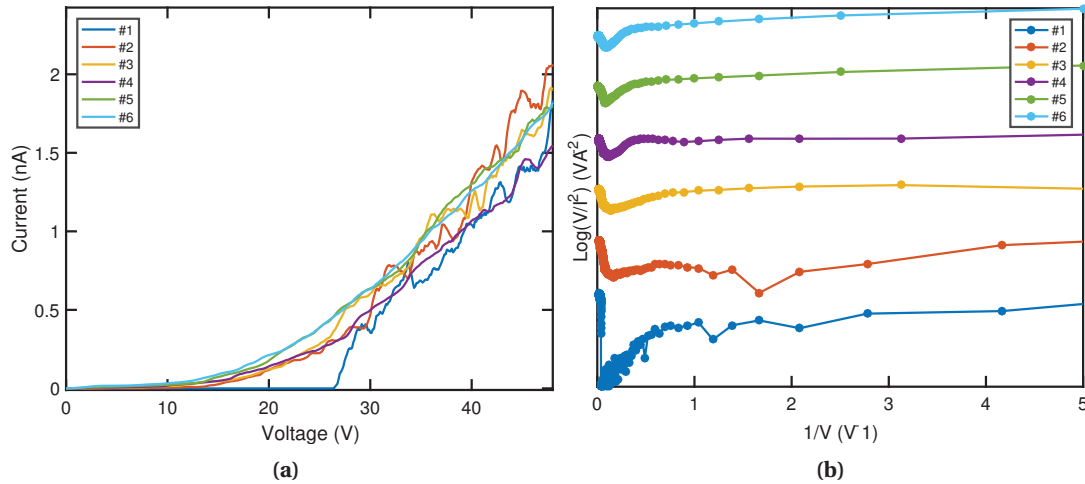


**Figure 5.4** – Transition between DT and FN mechanism. Figure 5.4a presents six consecutive measurements performed on the same crystal. The switching is present at 26 V. In Figure 5.4b are shown the corresponding curves of 5.4a, as the voltage is increased (right to left) in the lowest curve, which corresponds to the IV curve where the switching took place, the slope of the curve changes at a transition voltage  $V_{tr} \approx 26$  V, which indicates the transition from DT to FN. For the successive measurements, that are scaled in the graph for clarity, the transition voltage is lowered to around  $V_{tr} \approx 10$  V.

In all the curves shown an inflexion point is present, indicating the transition from DT to FN tunnelling. In the lowest curve, which corresponds to the IV curve where the switching took place, the slope of the curve changes at a transition voltage  $V_{tr} \approx 26$  V, while for the successive measurements the transition voltage was lowered to around  $V_{tr} \approx 10$  V. A similar behaviour has been observed by Song [163] in a molecular transistor realised with a 1,8-octanedithiol molecule as active layer, shown in Figure 5.5.

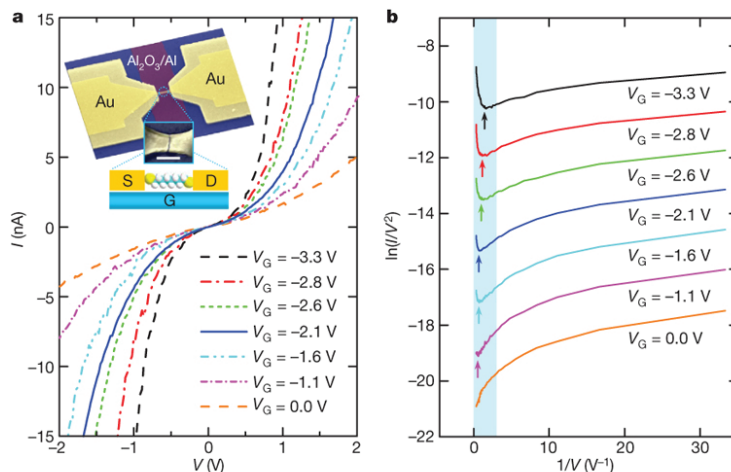


**Figure 5.5** – a)  $I(V)$  curves measured at different values of gate voltage. The inset shows the structure of the device and its schematic. S: source; D: drain; G: gate. Scale bar is 100 nm. b) FN plots indicating transition from DT to FN tunnelling with gate dependence. Reprinted with permission from [163].



### Resonant tunnelling

The presence of tunnelling as a mechanism that contributes to the total current measured in an IBAN crystal is suggested by those experimental observations that showed a fingerprint typical of resonant tunneling (RT), *i.e.* negative differential resistance (NDR). The study of this mechanism by Leo Esaki [164, 165] was awarded with the Nobel prize in physics in 1973. In NDR the current deviates from its standard tunnelling characteristics when the applied potential other than shifting the Fermi levels distorts the bands, causing a shifts of the potential well eigenstates. When the Fermi energy on one side aligns with one of the states, the transmission probability through the potential barrier is equal to the unity and corresponds to a maximum in the  $I(V)$  curve. A schematic of the process is shown in Figure 5.6.

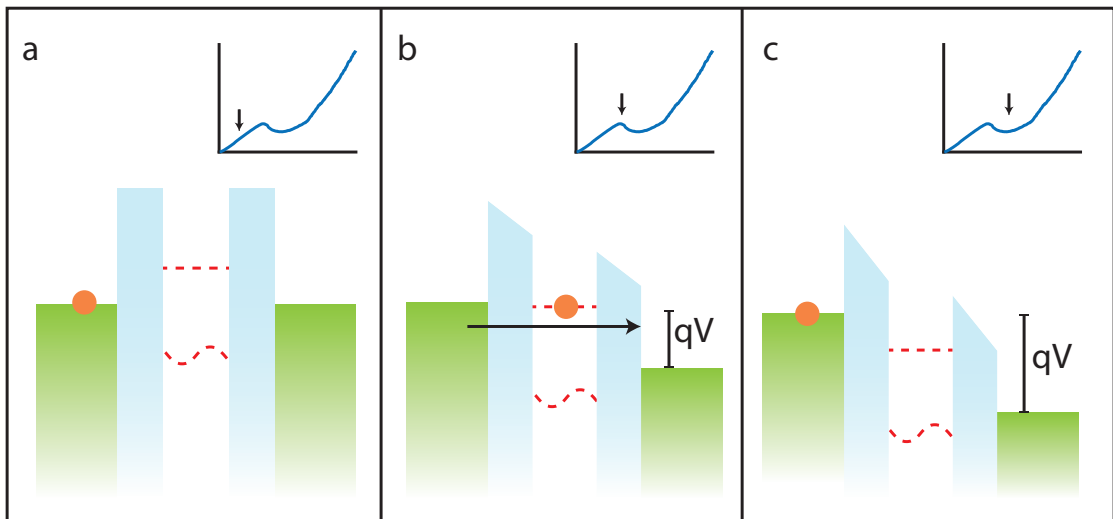


**Figure 5.6** – RT and NDR schematic. a) From the equilibrium a voltage is applied and the current starts increasing. b) When the Fermi energy (top edge of the green band) on one side aligns with one of the states the transmission probability through the potential barrier is equal to the unity and the current increases. c) If the voltage is further increased, the alignment is lost and the current shows a decrease for higher voltages.

Among the crystals tested, some exhibited NDR. Figure 5.7 shows two examples of this phenomenon. A symmetrical  $I(V)$  curve which shows NDR is shown in 5.7a, while an asymmetrical example can be seen in 5.7b. This latter can occur when the tunnelling electron transits in the potential well through energy states that are not aligned [166], so that when the voltage bias is reversed, the RT condition does not occur for the same energy band shifting. The presence of this asymmetric situation helped us also to discriminate the nature of this phenomenon from redox mechanisms, typically occurring in memristor (memory-resistor) devices [167]. One other feature of RT is that the position of the NDR peak can normally be changed by controlling the number of carriers [168]. In our case we did not have an external gate electrode, but nonetheless when I changed the delay time, that is the time waited by the parameter analyser before measuring current, I observed a shifting of the NDR peak shown in Figure

5.7c. One possible explanation is that the gating was realised electrostatically by the presence of trapped charges. This observation is consistent with the result obtained by Bauza in a metal-oxide-semiconductor (MOS) structure [169]. These NDR curves of  $\text{Ag}_{44}(\text{FTP})_{30}$  crystals have also been observed in inert atmosphere (Ar glovebox).

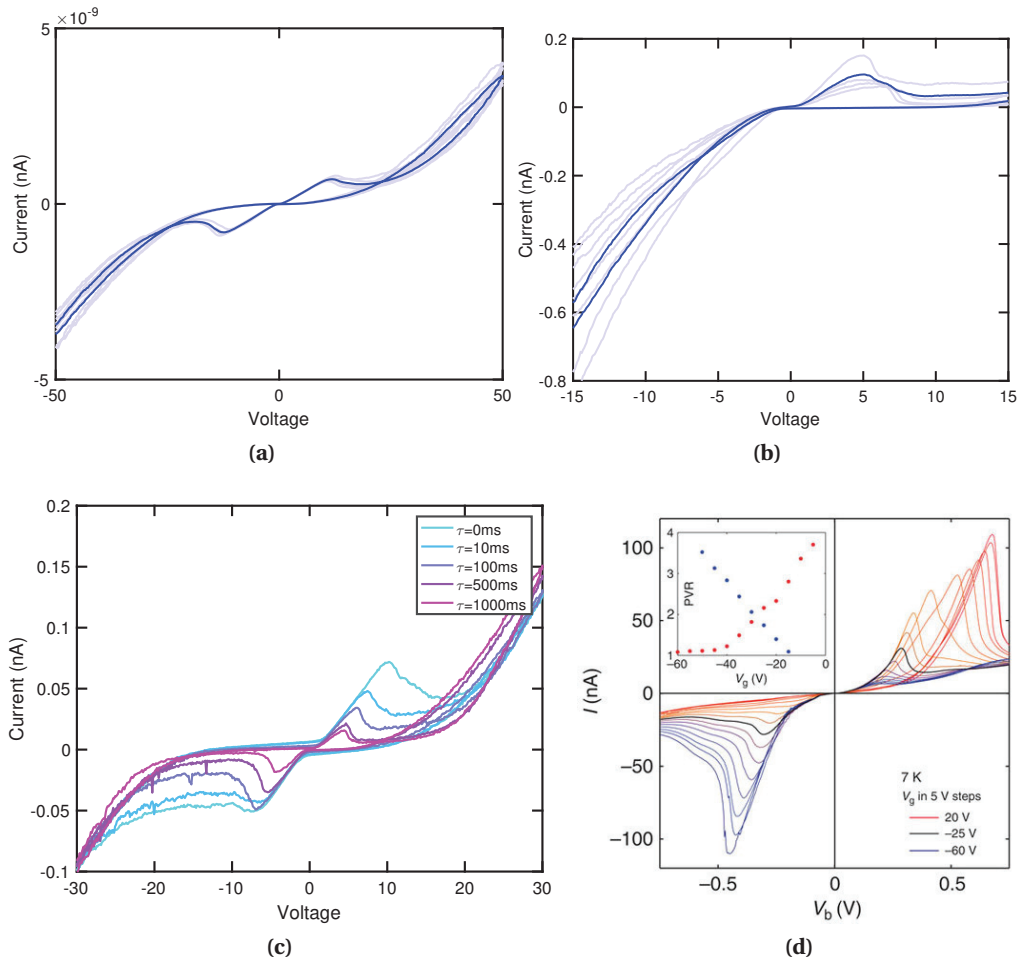


**Figure 5.7** – 5.7a shows a perfectly symmetrical  $I(V)$  curve which shows NDR. Asymmetric NDR, as in 5.7b, can occur when the tunnelling electron transits in the potential well through energy states that are not aligned [166]. The opaque curves represent the average of the underlying semitransparent curves. 5.7c shows measurements on a crystal of IBAN for varying delay time ( $\tau$ ). The position and height of the NDR peak are shifted, until the peak reaches a plateau for delay long time,  $\tau \rightarrow \infty$ . This shift may be due to an electrostatic gating realised through trapped charges, which would also cause a non-zero current when no voltage was applied. In 5.7d the results of Britnell [168] that show the NDR peak shifting of a boron nitride thin slab, sandwiched between graphene layers, realised through an external gating.

### 5.2.4 Summary

The aforementioned thermionic emission, hopping and tunnelling mechanisms were all found to contribute to the total current measured in a crystal of AgNCs. There are studies from Buttiker [170, 171] and more recently from Xiang [159] that show the possibility of an intermediate regime which predicts the coexistence of a partially coherent tunnelling transport and incoherent hopping mechanism. What arises from the analysis presented in this section is that these results are remarkable if we consider that the observed phenomena, which have, if confirmed, an intrinsic quantum origin (coherent resonant tunnelling), were measured at room temperature and on a macroscopically large sample, a crystal of several tens of micrometers. The complex crystalline structure of IBAN due to its periodically alternating metallic cores, FTP organic ligands and TPPB counterions form a varying electrostatic potential, shown in figure 5.8 and confirmed by the DFT calculation described in Appendix E, which shows spatial variation with length of the order of the electrons de Broglie's wavelength. This periodic variation forms a three dimensional atomically precise superlattice of unprecedented size. Although semiconducting one- and two-dimensional superlattices were already realised thirty years ago [165, 172, 173], example of atomically precise three dimensional structure have started to appear only recently [67, 174], thanks to the improvements in strategies for synthesizing quantum dots, magnets and noble-metal clusters [175]. To the best of my knowledge the results presented in this thesis might represent the first experimental observation of quantum collective behaviour in macroscopic superlattices.

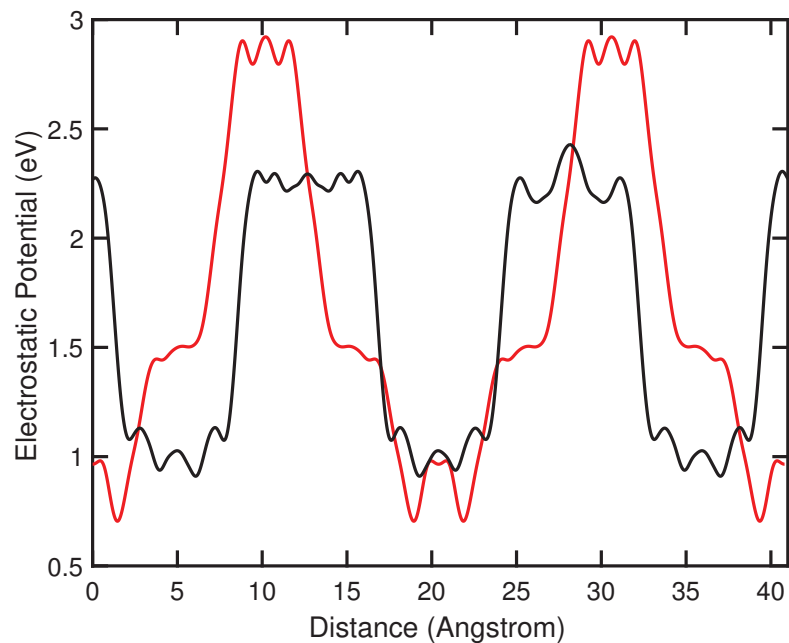


**Figure 5.8** – DFT calculated electrostatic potential for the unperturbed crystal (red curve) and the switched crystal (black curve) along the [100] and [001] crystal planes respectively.

### 5.3 Origin of the switching mechanism

Among the results presented in Chapter 4, the switching of conductivity in IBAN crystals is probably the most interesting and cumbersome at the same time. Examples from the literature offer an interpretation, but they cannot explain all the features observed. I present here three systems in which the electrical properties of a given system exhibit a sudden change, in which similarities as well as difference with AgNC crystals are found.

#### 5.3.1 Similar phenomena

**SCLC** Space charge effect is based on the dielectric relaxation of a material (*cf.* Appendix D). When charges are injected in a poorly conducting material they accumulate, until neutrality cannot be maintained, so the current density increases quadratically with the applied voltage. If the material presents impurity, defects or other kind of trap states, the injected electrons start to occupy these trap states. Once they are all filled, the current density increases dramatically for a voltage threshold defined as  $V_{TFL}$ , trap-filled limit (TFL) voltage. Deviations from standard SCLC have been found in a recent paper by Bakr [176], describing the low-trap density in organolead trihalide perovskite single crystals. However, the multiple jumps in conductivity observed in IBAN crystal, as well as switching to a lower conductive state for increasing voltages, cannot be explained within the SCLC theory.

**Nanoionic resistive switching** Nanoionic-based memristors are a promising family of material for their use in electronics because they exhibit resistive switching effects. Their use as memories come from the fact the switching mechanism is reversible, so the material can be set into a conductive state and reset to high resistance [167] by sweeping a voltage. There are two switching mechanisms: unipolar and bipolar. In the former the forming voltage is higher than the voltage at which reset takes place. For this reason a compliance, or current limitation, has to be set in order not to reach dielectric breakdown. In bipolar switching the set operation occurs at one polarity of the voltage, while the reset to high resistance requires the opposite polarity. There are several classes of materials, sandwiched between two metallic electrodes, that show resistive switching behaviour: oxides, like  $\text{TiO}_2$ ,  $\text{NiO}$  and  $\text{VO}_2$ , semiconductor heterojunctions, metal or semiconducting perovskite interfaces, but also crystals of  $\text{Ag}_2\text{S}$  [177–179], a component of  $\text{Ag}_{44}(\text{FTP})_{30}$  clusters. These crystals undergo a redox process induced by cation migration. At the cathode and anode the following process takes place and Ag wires start to form,  $\text{Ag}^+(\text{Ag}_2\text{S}) + \text{e}^- \xrightleftharpoons[\text{oxidation}]{\text{reduction}} \text{Ag}$ , then by changing the polarity of the applied voltage metal atoms dissolve, and the formed wire is annihilated.

Despite the similarities such as the material composition and the appearance of the switching, there are differences that suggest that IBANs cannot be considered as memristor materials. Firstly, IBAN crystals did not show dielectric breakdown in the voltage range I used to measure  $I(V)$  curves, which occurs for unipolar memristor since the current increase is not sustained by the material. Secondly, in the case of unipolar switching, the voltage at which the reset

takes place in memristors is lower than that of the transition to a higher conductivity. This was not always the case for the crystals measured in this work, as shown in Figure 4.12a, where the device switched off for increasing voltages. Thirdly, to the best of my knowledge, the presence of multiple discrete switching jumps, both in the direction of increasing conductivity and in that of lowering conductivity, has not been reported for memristor device. Another difference is in the capability of storing energy, which cannot exist by definition in the case of memristors: in 1971 Chua defined memristors [180] as a passive elements, so they are not able to store energy. IBANs however showed a non zero current for zero applied voltage under certain conditions, as shown in Figure 5.7c. The last argument is that the single crystal XRD of a switched IBAN crystal showed that components of the cluster did not change, they were neither modified nor degraded. In conclusions, it is possible to assert that despite the similarity of the switching between the two systems, IBAN cannot be considered memristors.

#### 5.3.2 Phase transition

In order to understand the origin of the switching mechanism, it is useful to summarise all the experimental observation that concern the change of IBAN's conductivity:

- a) most of the crystals showed a dramatic increase in conductivity when a voltage was applied across them;
- b) crystals appeared to switch when a threshold voltage was reached, even though there were exceptions: in some case, consecutive sweeps were required to achieve switching;
- c) the switching also appeared through jumps in conductivity, as if the process that started the transformation would not be finished in once;
- d) crystals showed a dependence of the threshold voltage upon on the orientation of the applied field with respect to the crystal's planes;
- e) after relaxation, crystals exhibited a lower threshold voltage in the successive sweeps;
- f) switching occurred while decreasing voltage;
- g) an inverse switching mechanisms was also observed;
- h) in most cases, the inverse mechanism occurred for smaller voltages and same polarity;
- i) the switch off also occurred through intermediate conductive levels;
- j) jumps between two conductive state have been observed in a four-terminal experiment as a function of decreasing temperature;

If we consider the Joule's effect, the heat dissipated is proportional to the resistance squared, which means that the temperature in the crystal must increase, therefore the exception of point

b) and point f) suggest that the transformation cannot be triggered solely by temperature. The description of point c) suggests that the transformation might encounter multiple energetic barriers before reaching the higher conductivity state. When connecting a crystal with two electric probes, presumably, the electric field distribution does not extend to the whole crystal volume. If we then consider the XRD result for the switched crystal, we know that its whole structure has changed, which indicates that the transformation resulted from the application of an electric field has successively induced an analogous effect in the rest of the crystal. If we accept this explanation, the presence of multiple conductivity jumps would indicate the presence of grain boundary domains (geminated crystal) in the crystal which act as an additional energetic barrier for the transformation to occur. This mechanism resembles the collective behaviour presented by Yoon in Ag<sub>44</sub> p-MBA crystals [67]. He observed that when compressed, the crystal showed softening and the NCs underwent chiral rotations, exactly like gears, or a chiral honeycomb [100], where the bent p-MBA ligands act as torque-transfer relays and the hydrogen bonds as "molecular hinges" [67]. In my case the superposition of a direct external stimulus, the electric field, and indirect, temperature causes the rotation of a counterion, which induce the opening of the facing FTP ligands. This new structural conformation gives rise to a new energetic landscape which may be the cause for increase in conductivity. The removal of the electric field, jointly with the decrease of crystal's temperature by thermalization with the environment, brings the crystal to its original non-conductive state. The existence of a new structural order suggests the presence of a phase transition, although some questions remain unanswered. First of all, it is not clear why a switched crystal would go back to its higher resistance state for increasing voltages. It is also not clear why in the four-terminal experiment, the resistance continued to jump between two phases for decreasing temperature. Further investigation is required to ascertain the existence of a phase transition in IBAN crystals, but the analysis carried on in this thesis constitutes a first corroborating step in this direction.

## 6 Conclusion and perspectives

The aim of this thesis was to explore and characterized the electric response of a  $\text{Ag}_{44}(\text{FTP})_{30}$  crystal to an electric field. The appearance of a low resistance state in these crystals has been demonstrated and its origins have been identified.

I presented the motivations that moved the boundaries of interest in metal clusters as a new family of materials, from simply exotic to potentially useful, I found that the reason lies in the entangled relationship between size, discrete energetic density of states and access to the fundamental properties through precise control of the synthesis and composition.

Given the complexity and discrete energetic nature of the single unit components of the crystals, non-trivial behaviours were expected and confirmed by experiments. To the best of my knowledge this work does not only constitute the first experimental investigation of the electronic properties of AgNC crystals, but, more generally, it represents the first study of the electronic bulk properties of a crystal of metal clusters. Interest in these materials has driven a rapid development in their synthesis and processing, which I was able to utilise to obtain crystals of  $\text{Ag}_{44}(\text{FTP})_{30}$  clusters of few tens of micrometers in size. These assemblies of clusters were then used to extract meaningful physical properties, such as the material permittivity, through UV-VIS absorption measurement of thin crystals. The electric response of crystals of IBANs was then tested in two- and four- terminal configurations and showed conductivity switching at high voltages between a less and a more conductive phase. Single crystal x-ray diffraction measurements showed that each of the conductive phase was characterized by a different crystal structure. It is worth mentioning the transformed crystal did not undergo a structural reconstruction, *i.e.* the silver cores were not affected by the electric field, but it exhibited a relocation of the tetraphenyl phosphonium  $[(\text{C}_6\text{H}_5)_4\text{P}^+]$  and of 3 of the 30 fluorophenyl thiols per unit cell, which is thought of being responsible for the improved electrical performances. These findings are remarkable because, as shown by the single crystal XRD result of the switched crystal, the change involved the whole crystal, not only the portion directly exposed to the electric field: the field induced a shift in the mobile counterions, which translated towards the cluster and resulted in opening of the ligands on top of the cluster's surface. This relocation triggered the rearrangement of the cations and ligands of the whole

## Chapter 6. Conclusion and perspectives

---

crystal, suggesting an electric-field induced phase transition. A similar collective response to an applied external pressure has been predicted by Yoon [67], but no experimental results have ever been shown, neither for pressure nor electrical stimuli.

In a paper published in Nature in 2003, O'Brien realised a "precisely ordered three-dimensional superlattice" [174], made of magnetic nanocrystals ( $\text{Fe}_2\text{O}_3$ ) and quantum dots (PbSe), a material "with properties arising from the controlled interaction of the different nanocrystals in an assembly". Analogously, the three dimensional, atomically precise periodicity offered by the crystal of clusters forms a perfect superlattice, which also exhibits properties originated from the interaction among the fundamental constituents. The analysis conducted on the measured current-voltage characteristic showed the existence of NDR, a feature typical of resonant tunnelling mechanism. Resonant tunnelling is expected to occur in superlattices whose spatial variations are such that the electron coherence is maintained, a condition which is satisfied in  $\text{Ag}_{44}(\text{FTP})_{30}$  crystals where the de Broglie's electrons wavelength is comparable with the distances between tunnelling sites. Further experiments are needed to provide a full description of the phenomenon. To the best of my knowledge, no superlattice systems that exhibit resonant tunnelling with more than a few tens of layers have been observed. This observation might be achieved with my crystals as a result of the uniqueness of their atomically precise repeating unit, that is the  $\text{Ag}_{44}(\text{FTP})_{30}$  cluster.

Gold and silver already offer a plethora of atomically precise clusters and new crystals will be realized out of them, offering the possibility of control over the hopping/tunnelling distance, varying the periodic potential and thus the resulting properties. Additionally, from an engineering point of view, an incredible amount of work could be done if the processing of the material improves. Thin crystalline films will ease the fabrication of devices and potential memory applications. In conclusion I would like to go back to the introduction and cite Feynman [1] again: "there is plenty of room. . ." for new discoveries and findings in the field of superlattices and metal clusters, and I hope the work presented in this thesis has paved the way to achieve them.



# A Microspectroscopy

A customized Olympus BX-61 microscope (see figure A.1) was used in order to measure the interaction of light with crystals of  $\text{Ag}_{44}(\text{FTP})_{30}$ . This technique allows a quantitative analysis of the light-matter interaction with the spatial resolution of a microscope. This was realized by inserting an optical beam splitter (80:20) in the optical beam path. Once the beam had been split, it was directed into an optical fiber, that worked as pinhole of variable size, depending on the core dimension. The fiber lay at the aperture conjugate plane of the sample, *i.e.* it is an illumination conjugate, and through this the beam was sent to a spectrometer (Ocean Optics QE 65000).

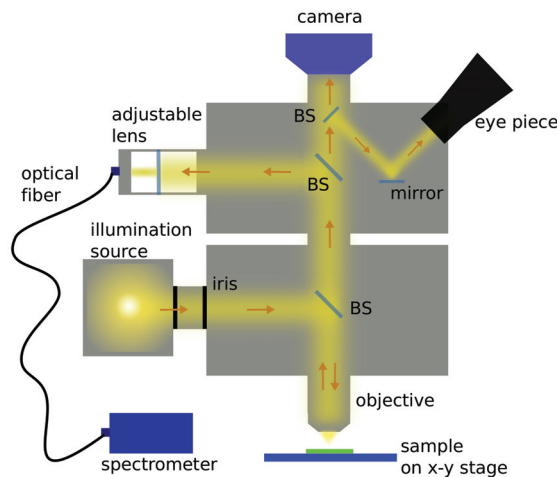


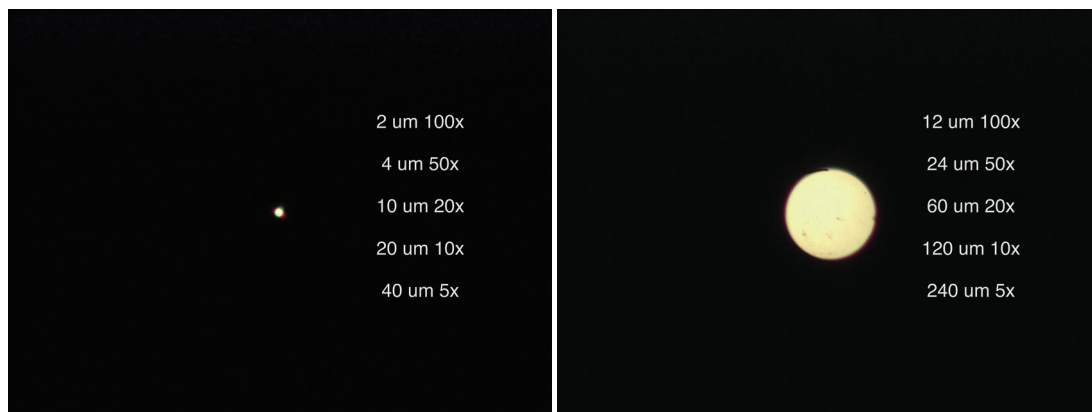
**Figure A.1** – Microspectroscopy setup. The optical pathway of a conventional light microscope is split by the presence of an optical beamsplitter (BS), and directed through an optical fiber in spectrometer.

The built-in halogen lamp (spectral range 380-860 nm) of the microscope was used as light source, but could be changed with a broader one such as Ocean Optics DH-2000, spectral range 215-2000 nm. The use of high magnification objective introduced wave vector dispersion, thus in order to minimize this effect low magnification objectives with lower numerical aperture were preferred. The region of interest (ROI) could be moved across the sample with manual

## Appendix A. Microspectroscopy

---

translational stage and the collection spot size could be chosen by the fiber core dimension together with the magnifying objective, ranging from 240  $\mu\text{m}$  with a 600  $\mu\text{m}$  core fiber and 5 $\times$  objective to 2  $\mu\text{m}$  with a 50  $\mu\text{m}$  core fiber and 100 $\times$  objective (see figure A.2)



(a) Collection beam spot size with a 50  $\mu\text{m}$  fiber.

(b) Collection beam spot size with a 600  $\mu\text{m}$  fiber.

**Figure A.2** – The size of the collection beam spot size can be varied using fibers with different core dimensions and also by changing magnification. Available fibers ranged from 50  $\mu\text{m}$  to 1000  $\mu\text{m}$  in core size. The spot size in the center of the two images can have the dimension written on the side for the corresponding objective.

## B Determining refractive index and complex dielectric function

In the previous appendix it was shown how it is possible to measure the absorption of a sample at the microscale. In reality, the physical quantity that is measured by the spectrometer is the absorbance, *i.e.* the amount of incident light absorbed. The absorbance depends on the thickness of the material the light travels through and on an extinction coefficient (or function). The spectrometer measures the amount of transmitted light  $T$ , that passing through a medium of thickness  $d$ , follows the Lambert-Beer law:

$$T = \frac{I_{out}}{I_{inc}} \quad A = \log_{10} \frac{I_{inc}}{I_{out}} = -\log_{10} T \quad (\text{B.1})$$

where  $I_{inc}$  is the intensity of the incident beam and  $I_{out}$  is that of the transmitted beam. Being the logarithm of a ratio, the absorbance is dimensionless. Because it is a linear function of the sample thickness, it is possible to define the optical density  $a_\lambda$  so that:

$$A = a_\lambda d \quad (\text{B.2})$$

The optical density is thus given by:

$$a_\lambda = -\frac{1}{d} \log_{10} T = -\frac{1}{d} \frac{\ln T}{\ln 10} \quad (\text{B.3})$$

## Appendix B. Determining refractive index and complex dielectric function

---

On the other hand the relation between the extinction coefficient  $\kappa$  and the absorption  $\alpha$ :

$$\kappa = \alpha \frac{\lambda}{4\pi} \quad (\text{B.4})$$

where:

$$\alpha = -\frac{1}{d} \ln T \quad (\text{B.5})$$

Combining together B.5, B.4 and B.3:

$$\kappa = -\frac{1}{d} \frac{\lambda}{4\pi} \ln T = a_\lambda \frac{\lambda}{4\pi} \ln 10 \quad (\text{B.6})$$

So if the last equation is multiplied and divided by the thickness  $d$ :

$$\kappa = \frac{A}{d} \frac{\lambda}{4\pi} \ln 10 \quad (\text{B.7})$$

Equation B.7 allows, knowing the thickness  $d$ , to determine the imaginary part of the complex refractive index  $\hat{n} = n + i\kappa$  from a UV-VIS spectroscopy measurement. The refractive index is an analytic function in the upper complex angular frequency plane and its complex poles are located in the lower half of the complex plane. In addition, being dispersive, *i.e.*  $\hat{n} = \hat{n}(\omega)$ , the principle of causality holds, so that the Kramers-Kronig relation (KK) can be applied [116–118], so that knowing the imaginary part of the refractive index is sufficient to determine the real one and vice versa. The KK equations that link the real and imaginary part of a complex analytic function are:

$$\kappa(\omega) = -\frac{1}{\pi} \text{P} \int_{-\infty}^{+\infty} \frac{n(\omega')}{\omega' - \omega} d\omega' \quad (\text{B.8})$$

$$n(\omega) = -\frac{1}{\pi} \text{P} \int_{-\infty}^{+\infty} \frac{\kappa(\omega')}{\omega' - \omega} d\omega' \quad (\text{B.9})$$

where P is the Cauchy principal value. This is extremely useful when it comes to determine the permittivity  $\epsilon$  of a material because it is related to  $\hat{n}$  through

$$n = \sqrt{\epsilon_r \mu_r} \quad (\text{B.10})$$

The complex permittivity is defined as:

$$\hat{\epsilon}_r = \epsilon_r^{re} + i\epsilon_r^{im} \quad (\text{B.11})$$

---

and its real and imaginary components are relate to the complex refractive index through:

$$\epsilon_r^{re} = n^2 - \kappa^2 \qquad \epsilon_r^{im} = 2n\kappa \qquad (\text{B.12})$$

MATLAB functions that implement the above mentioned equations are here presented. The functions *kkrebook2.m* and *kkimbook2.m* are taken from [118].

## Appendix B. Determining refractive index and complex dielectric function

---

```
1 function rechi=kkrebook2(omega,imchi,alpha)
2 %The program inputs are the vector of the frequency
3 %(or energy) components, the vector of the imaginary
4 %part of the susceptibility under examination, and
5 %the value of the moment considered.
6 %The two vectors must have the same length
7 %and the frequency vector omega must be equispaced.
8 %If not, apply MATLAB functions such as interp.
9 %If imchi is the imaginary part of a linear susceptibility,
10 %alpha must be 0.
11 %If imchi is the imaginary part of the nth
12 %harmonic generation susceptibility, alpha=0,1,..2n.
13 %If imchi is the imaginary part of a pump and probe
14 %susceptibility, alpha=0 or 1.
15 %This files accompanies the book
16 %"Kramers-Kronig Relations in Optical Materials Research"
17 %by Lucarini, V., Saarinen, J.J., Peiponen, K.-E., Vartiainen, E.M.
18 %Springer, Heidelberg, 2005
19 %where the theory and applications are fully developed.
20 %The output is the estimate of the real part as obtained
21 %with K-K relations.
22 %This software is distributed under the GNU licence agreement
23 %by Valerio Lucarini
24 %email: lucarini@alum.mit.edu
25 %University of Camerino
26 %Department of Mathematics and Computer Science
27 %Camerino, Italy
28
29 if size(omega,1)>size(omega,2);
30 omega=omega';
31 end; if size(imchi,1)>size(imchi,2);
32 imchi=imchi';
33 end;
34 %Here the program rearranges the two vectors so that,
35 %whichever their initial shape, they become row vectors.
36 g=size(omega,2);
37 %Size of the vectors.%
38 rechi=zeros(size(imchi));
39 %The output is initialized.
40 a=zeros(size(imchi));
41 b=zeros(size(imchi));
42 %Two vectors for intermediate calculations are initialized
43 deltaomega=omega(2)-omega(1);
44 %Here we compute the frequency (or energy) interval
45 j=1;
46 betal=0;
47 for k=2:g;
48 b(1)=betal+imchi(k)*omega(k)^(2*alpha+1)/(omega(k)^2-omega(1)^2);
49 betal=b(1);
50 end;
51 rechi(1)=2/pi*deltaomega*b(1)*omega(1)^(-2*alpha);
52 %First element of the output: the principal part integration
```

---

```

53 %is computed by excluding the first element of the input
54 j=g;
55 alpha1=0;
56 for k=1:g-1;
57 a(g)=alpha1+imchi(k)*omega(k)^(2*alpha+1)/(omega(k)^2-omega(g)^2);
58 alpha1=a(g);
59 end;
60 rechi(g)=2/pi*deltaomega*a(g)*omega(g)^(-2*alpha);
61 %Last element of the output: the principal part integration
62 %is computed by excluding the last element of the input
63 for j=2:g-1; ;
64 %Loop on the inner components of the output vector.
65 alpha1=0;
66 beta1=0;
67 for k=1:j-1;
68 a(j)=alpha1+imchi(k)*omega(k)^(2*alpha+1)/(omega(k)^2-omega(j)^2);
69 alpha1=a(j);
70 end;
71 for k=j+1:g;
72 b(j)=beta1+imchi(k)*omega(k)^(2*alpha+1)/(omega(k)^2-omega(j)^2);
73 beta1=b(j);
74 end;
75 rechi(j)=2/pi*deltaomega*(a(j)+b(j))*omega(j)^(-2*alpha);
76 end;
77 %Last element of the output: the principal part integration
78 %is computed by excluding the last element of

```

## Appendix B. Determining refractive index and complex dielectric function

---

```
1 function imchi=kkimbook2(omega,rechi,alpha)
2 %The program inputs are the vector of the frequency (or energy)
3 %components, the vector of the real part of the susceptibility
4 %under examination, and the value of the moment considered.
5 %The two vectors must have the same length
6 %and the frequency vector omega must be equispaced.
7 %If not, apply MATLAB functions such as interp.
8 %If rechi is the real part of a linear susceptibility,
9 %alpha must be 0.
10 %If rechi is the real part of the nth
11 %harmonic generation susceptibility, alpha=0,1,..2n.
12 %If rechi is the real part of a pump and probe
13 %susceptibility, alpha=0 or 1.
14 %This files accompanies the book
15 %"Kramers-Kronig Relations in Optical Materials Research"
16 %by Lucarini, V., Saarinen, J.J., Peiponen, K.-E., Vartiainen, E.M.
17 %Springer, Heidelberg, 2005
18 %where the theory and applications are fully developed.
19 %The output is the estimate of the imaginary part as obtained
20 %with K-K relations.
21 %This software is distributed under the GNU licence agreement
22 %by Valerio Lucarini
23 %email: lucarini@alum.mit.edu
24 %University of Camerino
25 %Department of Mathematics and Computer Science
26 %Camerino, Italy
27
28 if size(omega,1)>size(omega,2);
29 omega=omega';
30 end; if size(rechi,1)>size(rechi,2);
31 rechi=rechi';
32 end;
33 %Here the program rearranges the two vectors so that,
34 %whichever their initial shape, they become row vectors.
35
36 g=size(omega,2);
37 %Size of the vectors.%
38
39 imchi=zeros(size(rechi));
40 %The output is initialized.
41
42 a=zeros(size(rechi));
43 b=zeros(size(rechi));
44 %Two vectors for intermediate calculations are initialized
45
46 deltaomega=omega(2)-omega(1);
47 %Here we compute the frequency (or energy) interval
48
49 j=1;
50 betal=0;
51 for k=2:g;
52 b(1)=betal+rechi(k)*omega(k)^(2*alpha)/(omega(k)^2-omega(1)^2);
```



---

```

53  beta1=b(1);
54  end;
55  imchi(1)=-2/pi*deltaomega*b(1)*omega(1)^(1-2*alpha);
56  %First element of the output: the principal part integration
57  %is computed by excluding the first element of the input
58
59  j=g;
60  alpha1=0;
61  for k=1:g-1;
62  a(g)=alpha1+rechi(k)*omega(k)^(2*alpha)/(omega(k)^2-omega(g)^2);
63  alpha1=a(g);
64  end;
65  imchi(g)=-2/pi*deltaomega*a(g)*omega(g)^(1-2*alpha);
66  %Last element of the output: the principal part integration
67  %is computed by excluding the last element of the input.
68
69  for j=2:g-1; ;
70  %Loop on the inner components of the output vector.
71  alpha1=0;
72  beta1=0;
73  for k=1:j-1;
74  a(j)=alpha1+rechi(k)*omega(k)^(2*alpha)/(omega(k)^2-omega(j)^2);
75  alpha1=a(j);
76  end;
77  for k=j+1:g;
78  b(j)=beta1+rechi(k)*omega(k)^(2*alpha)/(omega(k)^2-omega(j)^2);
79  beta1=b(j);
80  end;
81  imchi(j)=-2/pi*deltaomega*(a(j)+b(j))*omega(j)^(1-2*alpha);
82  %Last element of the output: the principal part integration
83  %is computed by excluding the last element of the input
84  end;

```

## Appendix B. Determining refractive index and complex dielectric function

---

```
1 function [eps_complex, n_complex]=A2nk(Abs,lambda,d)
2 % It calculates the complex refractive index of a material,
3 % starting from a measured absorbance and thickness of the sample.
4 % Wavelength and thickness are expressed in nm.
5 % Abs = absorbance as measured from spectrometer
6 % lambda = wavelength sampling of the spectrometer
7 % d = thickness of the sample
8 A=Abs;
9 Lambda=lambda;
10 %Absorption calculation as described in the Appendix
11 Kappa=log(10)/4/pi*Lambda.*A/d;
12 %Define frequency vector and calculate KK relations
13 c=3e8;
14 Omega=2*pi*c./Lambda*1e9;
15 wmin=min(Omega);
16 wmax=max(Omega);
17 dw=(wmax-wmin)/(length(Omega)-1);
18 omega=(wmin:dw:wmax);
19 %Interpolates Kappa to the equally spaced frequency values
20 kappa=interp1(Omega,Kappa,omega);
21 n=1.5+kkrebook2(omega,kappa,0);
22 %Interpolate to recieved wavelength range and prepare output
23 omegal=2*pi*c./lambda*1e9;
24 kappal=interp1(Omega,Kappa,omegal,'nearest','extrap');
25 n1=interp1(omega,n,omegal,'nearest','extrap');
26 eps_complex=n1.^2-kappal.^2+2*1i*n1.*kappal;
27 n_complex=n1+1i*kappal;

1 function thickness = abs2thickness(k,wvl,abs)
2 %thickness = abs2thickness(k,wvl,abs)
3 %It gets imag(n_complex), absorbance as measured and wavelength
4 % and returns the thickness of the material
5 L = zeros(length(abs),1);
6 for i =1:length(abs)
7 L(i) = abs(i)./k(i)*log(10).*wvl(i)/(4*pi);
8 end
9 thickness= mean(L);
10 end
```

---

```

1 function n_complex = eps2nk(wvl,eps_complex)
2 %Convert epsilon values to n and k
3 n = sqrt((sqrt(real(eps_complex).^2+imag(eps_complex).^2)+real(eps_complex))
4         /2);
5 k = sqrt((sqrt(real(eps_complex).^2+imag(eps_complex).^2)-real(eps_complex))
6         /2);
7 n_complex=n+1i*k;
8
9 [AX,H1,H2] = plotyy(wvl,n,wvl,k);
10 set(get(AX(1),'Ylabel'),'String','n')
11 set(get(AX(2),'Ylabel'),'String','k')
12 xlabel('wavelength (nm)')
13 title('n and k')
14 end

1 function eps_complex = nk2eps(wvl,n_complex)
2 %Convert n and k values to epsilon
3 eps_real = real(n_complex).^2-imag(n_complex).^2;
4 eps_imag = 2*real(n_complex).*imag(n_complex);
5 eps_complex= eps_real+1i*eps_imag;
6
7 [AX,H1,H2] = plotyy(wvl,eps1,wvl,eps2);
8 set(get(AX(1),'Ylabel'),'String','\epsilon_1')
9 set(get(AX(2),'Ylabel'),'String','\epsilon_2')
10 xlabel('wavelength (nm)')
11 title('\epsilon_1 and \epsilon_2')
12 end

```



## C Customized probe station

For the electrical characterization of IBAN crystals in inert atmosphere, a home built probe station was realized to fit the glovebox. A schematic of the setup is shown in figure C.1. The  $xyz$  and rotational stages were purchased from Thorlabs, as well as the optical components, CCD camera and power meter. The system was composed of the following parts:

- A LED light source used to illuminate the sample surface;
- a 50:50 beam splitter used to measure at any given time the laser or light source power impinging on the sample;
- a silicon photodiode power meter S120C (Thorlabs)
- a DCC1645C (Thorlabs) camera to image the sample and to position the probes on the crystal.
- a 20× long working distance Mitutoyo magnification objective NA=0.42 and WD=20 mm
- a translational ( $xyz$ ) and rotational ( $\theta$ ) stage to move the sample around.

The micromanipulators (DPP 105 Cascade Microtech) were connected with triax cable to a Keithley SCS 4200 that allowed to apply voltages in the range of 0 V to 210 V, with current measured with an accuracy of  $\pm 100$  fA

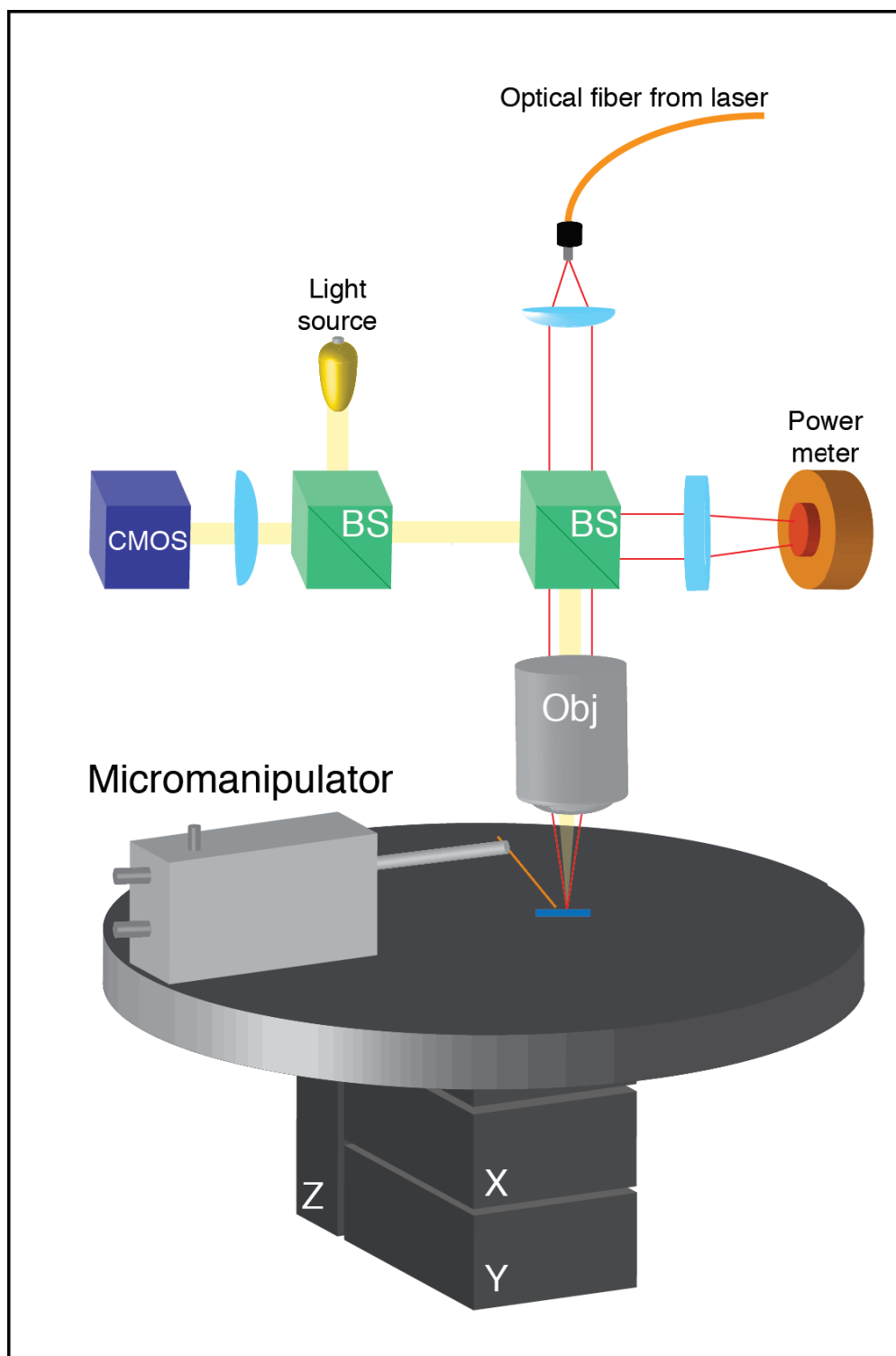


**Figure C.1** – Schematic of the custom made probe station: BS stands for beam splitter, CMOS is a camera, Obj is a 20× objective used to collimate the laser and focus onto the sample. The circular blue elements are achromatic doublets of different focal length for expand the laser beam, focus the image on the camera plane and on the power meter. For clarity only one micromanipulator is represented.

# D Conduction mechanism

## D.1 Schottky emission

Thermionic emission theory was first derived by Bethe [181] and the revisited by Schottky [182] in the case of an applied external bias. It describes the conduction of thermally activated electrons injected over the energy barrier ( $\phi_b$ ) of an insulating material as shown in Figure D.1.

The expression for the current density reads:

$$J_{SE} = A^* T^2 \exp \left[ \frac{-q(\phi_b - \sqrt{qV/4\pi\epsilon_i w})}{k_b T} \right] \quad (D.1)$$

where  $A^* = \frac{4\pi q m_{eff}^3 k_b^2}{h^3}$  is the effective Richardson constant,  $T$  is the absolute temperature,  $q$  is the electronic charge,  $\phi_b$  is the energy barrier height,  $V$  is the applied voltage,  $w$  is the thickness and  $\epsilon_i$  is the permittivity of the insulating material,  $m_{eff}$  is the effective mass,  $h$  is the Planck's constant and, lastly,  $k_b$  is Boltzmann's constant. Simmons [183] demonstrated that the field emission is modified if the mean free path of the electrons is shorter than the width of the energy barrier. In this case:

$$J_{SMSE} = \alpha T^{\frac{3}{2}} \frac{V}{w} \mu \left( \frac{m_{eff}}{m_0} \right)^{\frac{3}{2}} \exp \left[ \frac{-q(\phi_b - \sqrt{qV/4\pi\epsilon_i w})}{k_b T} \right] \quad (D.2)$$

where  $\alpha$  is a constant,  $m_0$  is the free electron mass and  $\mu$  is the bulk mobility.

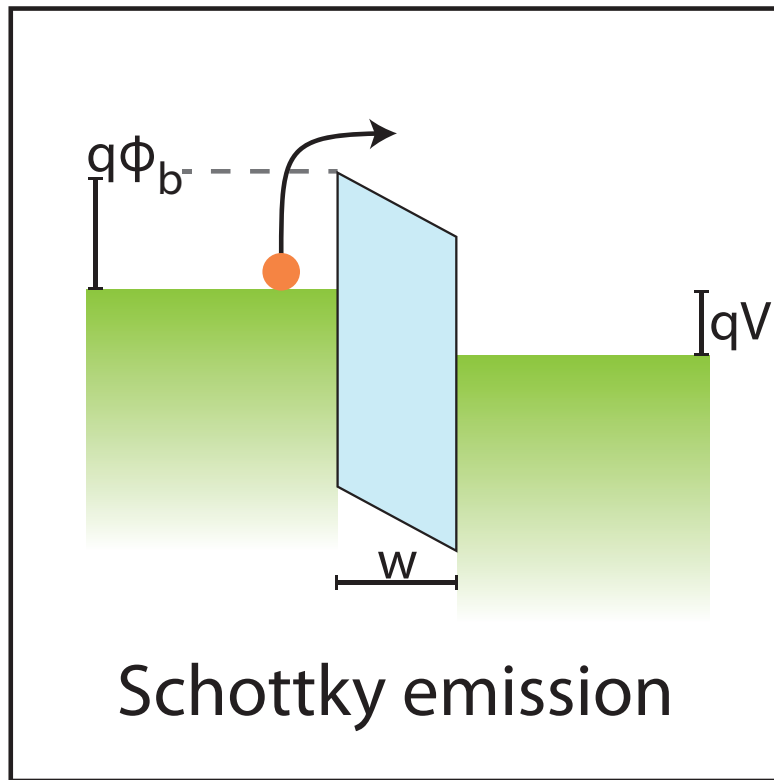


**Figure D.1** – Schottky field emission. A thermally activated electron is injected above the energy barrier  $\phi_b$  into the conduction band of an insulating material of width  $w$ . An external voltage  $V$  is applied across the whole structure and causes the band bending.

Schottky emission is a phenomenon that depends both on temperature and on the applied external voltage, therefore it can be either identified by fitting  $\log(J) \propto \sqrt{V}$  under constant temperature, or  $\log(J/T^2) \propto 1/T$  for fixed applied voltage. Results of this operation are shown in Figure D.2



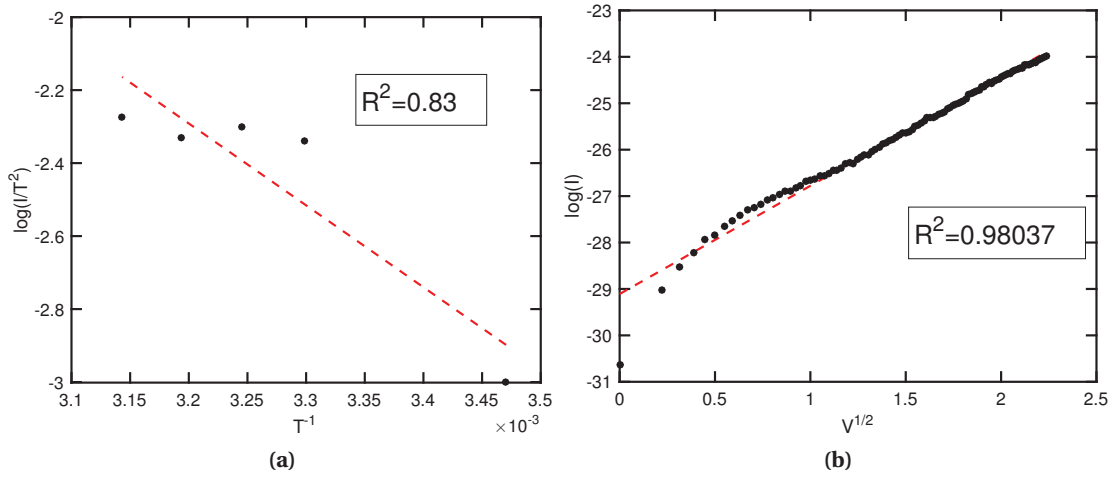


**Figure D.2** – In D.2a I fitted the results obtained in Section 4.3.2 with the expression for Schottky emission at constant electric field. The number of data points available and goodness of the fitting do not allow to ascertain the presence of thermionic field emission. In D.2b a fitting of the results presented in 4.6 under constant temperature shows better accordance between our data with the model proposed by Schottky.

## D.2 Poole-Frankel emission

P-F emission occurs when electrons trapped in localized states get excited by thermal fluctuations or by an external field, and get into the conduction band as shown in Figure D.3, where they can move through the crystal before occupying another localized trap state, or for applied voltage large enough, they can be extracted from the opposite electrode. Moreover, in the case of large electric field thermal activation becomes negligible.

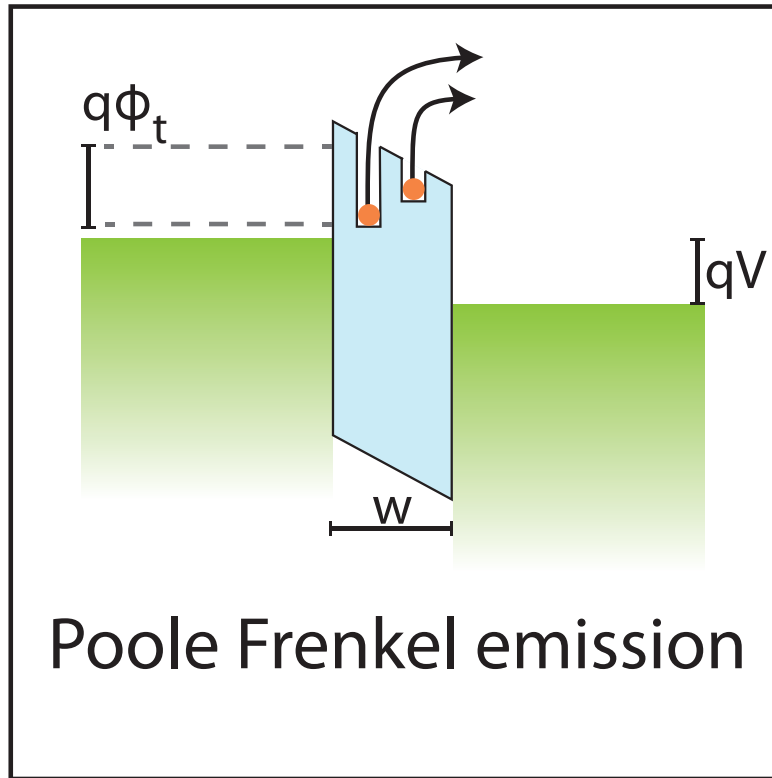


**Figure D.3** – Poole-Frenkel field emission. Electrons trapped in localized states of depth  $\phi_t$  are excited by thermal fluctuations or by an external field  $V$  and get into the conduction band. The external voltage  $V$  then pull these electron to the other electrode.

The expression for the current density [138] is very similar to Schottky emission, except for the height barrier term which is replaced by by the energy depth of the trap level ( $\phi_t$ ). The expression for the current density is:

$$J_{PF} = q\mu N_C \frac{V}{w} \exp \left[ \frac{-q(\phi_t - \sqrt{qV/\pi\epsilon_i w})}{k_b T} \right] \quad (D.3)$$

where  $q$  is the electronic charge,  $\mu$  is the bulk mobility,  $N_C$  is the density of state of the conduction band of the insulating material,  $T$  is the absolute temperature,  $\phi_t$  is the energy depth of the trap state,  $V$  is the applied voltage,  $w$  is the thickness and  $\epsilon_i$  is the permittivity of the insulating material and, lastly,  $k_b$  is Boltzmann's constant. In this case, if the conduction mechanism is dominated by Poole-Frenkel effect the measured current should be fitted with a linear regression in a  $\log(J/V)$  vs.  $\sqrt{V}/T$

### D.3 Space charge limited current

SCLC is a theory devised for disorder or low conductive materials [144, 184], whose defects, traps or impurity strongly effect the electric behaviour. This theory is based on the dielectric relaxation of conductive material which states that "if some free charge is injected into the material, this charge must be neutralized by mobile carriers either from the material boundary or from a charge reservoir" [185]. If a material is poorly conducting, when electrons are injected from one electrode, they accumulate until the dielectric relaxation is no longer maintained. When this situation occurs, the current characteristic deviates from the classical linear ohmic region and enters a quadratic region described by the Mott-Gurney's law:

$$J_{SCLC} = \frac{9}{8} \theta \epsilon_i \mu \frac{V^2}{L^3} \quad (D.4)$$

where  $\epsilon_i$  is the permittivity and  $\mu$  is the bulk mobility.  $\theta$  is a factor that accounts for the presence of traps,  $\theta=1$  in case of trap-free material or once all trap have been filled. To summarise, SCLC can be divided into three sections:

- an ohmic region at low voltages, where  $J \propto V$ ;
- a region with traps in which  $\theta < 1$  and the current obeys to the Mott-Gurney's law  $J \propto V^2$ ;
- a trap-filled region, which is entered at a threshold voltage  $V_{TFL}$  and that follows D.4 with  $\theta = 1$ .

### D.4 Hopping

Hopping is a thermally activated incoherent conduction mechanism between localized states that has been applied successfully as a model to several experimental observation of electric properties of FeAu and FePt NPs [129], dodecanethiol Au NPs [156] and AuNP supracrystals [157]. The VHR theory was developed by Mott and Davis [155] for a three dimensional hopping mechanism and was found to follow:

$$J_{VHR} = \sigma_0 \exp \left[ \left( -\frac{T_0}{T} \right)^{\frac{1}{4}} \right] E \quad (D.5)$$

where  $\sigma_0$  is the conductivity at  $T = T_0$  and  $E$  is the applied electric field. This expression was then modified to satisfy cases with lower dimensionality  $d$ , so that in its final version the current density is given by:

$$J_{VHR} = \sigma_0 \exp \left[ \left( -\frac{T_0}{T} \right)^{\frac{1}{d+1}} \right] E \quad (D.6)$$

## Appendix D. Conduction mechanism

Later Efros and Shklovskii [186] demonstrated that, when Coulomb interaction is taken into account, the VRH exponent becomes 1/2

$$J_{ES} = \sigma_0 \exp \left[ \left( -\frac{T_0}{T} \right)^{\frac{1}{2}} \right] E \quad (D.7)$$

Other interpretation of the hopping mechanism have been proposed by Zuppiroli [135] for adiabatic hops and multiphonon interaction and by Sheng for granular metals [153].

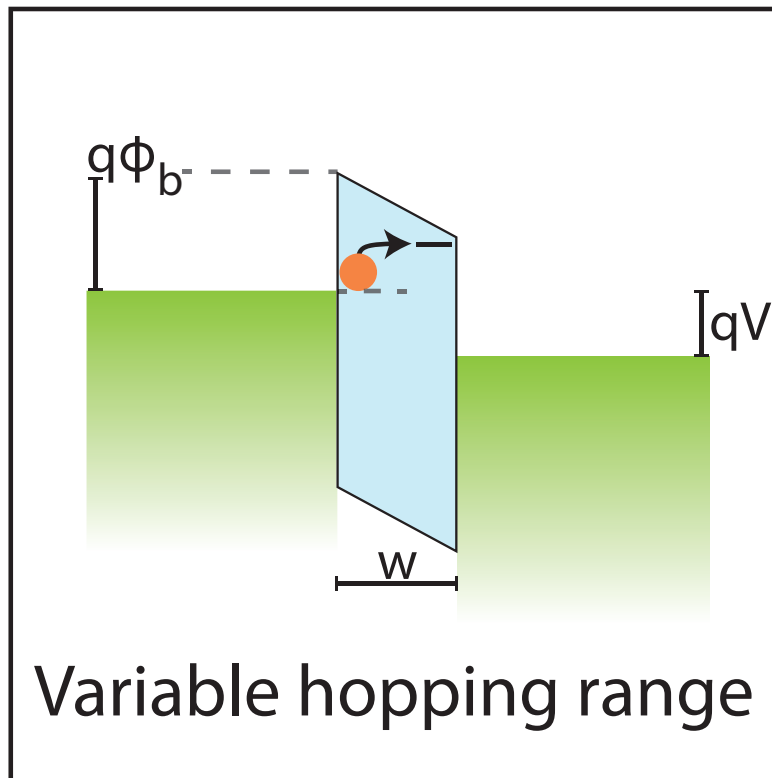


**Figure D.4** – Variable hopping range (VHR). Schematic energy band diagram for hopping in an insulating material through localized states.

## D.5 Tunnelling

I present here two tunnelling mechanism that I found to occur in the electronic conduction of IBAN crystals, direct tunnelling and Fowler-Nordheim tunnelling. The two mechanism are shown in Figure D.5. Within a quantum mechanical picture electrons are fully described with a wavefunction, that is a solution of the Schroedinger equation. The wavefunction gives the probability density of finding an electron at a given position. For an electron trapped between two energy barriers, the Schroedinger equation can be solved analytically and it shows that there is a finite probability of finding the electron across the barrier, which decreases exponentially for increasing width and height of the barrier. Therefore the density current,

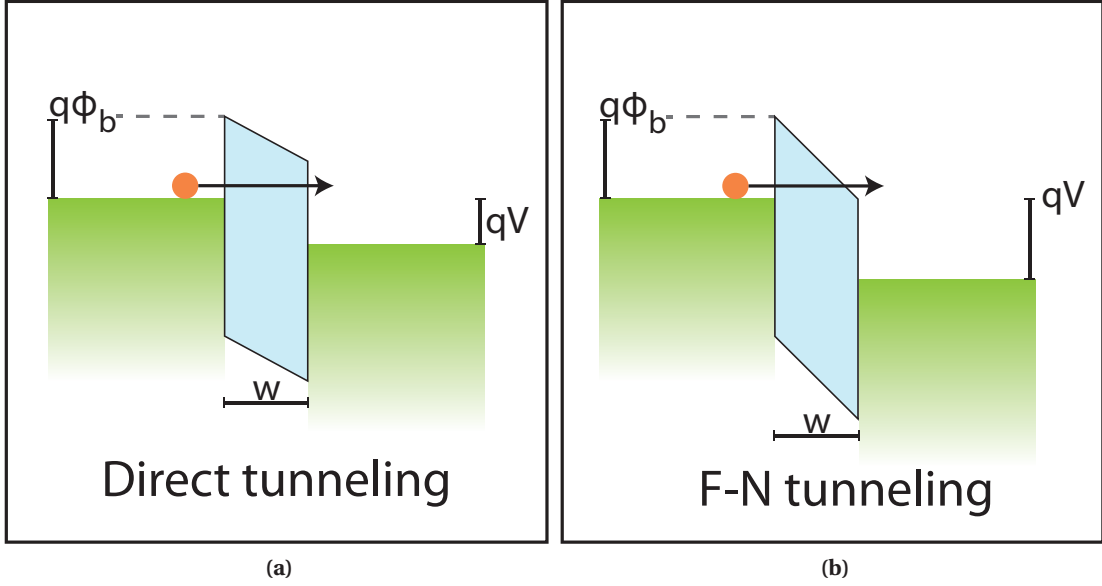


**Figure D.5** – Tunnelling mechanisms. In (a) band diagram schematic for direct tunnel. The tunnelling probability decreases exponentially for increasing width and barrier height, while when a voltage, high enough to tilt the band is applied, the effective barrier width is diminished, as shown in (b)

for tunnelling in one direction only, as calculated by Esaki and Tsu [165] is proportional to the quantum transmission coefficient  $T_p$  multiplied by the occupation probability of one side of the barrier and the unoccupied probability if the other side, that for electrons are the Fermi-Dirak distribution:

$$J = \frac{qm_{eff}k_bT}{2\pi^2\hbar^3} \int_0^\infty T_p \log \left( \frac{1 + \exp \left[ 1 + \exp[(E_F - E_l)/k_bT] \right]}{1 + \exp(1 + \exp[(E_F - E_l - eV)/k_bT])} \right) dE_l \quad (D.8)$$

where  $k_b$  is the Boltzmann's constant,  $\hbar$  is the Plank's constant,  $T$  is the absolute temperature,  $E_F$  is the Fermi energy,  $E_l$  is the longitudinal energy of the electrons and  $V$  is the applied voltage.

This expression can be simplified [187] for the case of direct tunnelling shown in D.5a as follows:

$$J_D T = \alpha \exp \left[ \frac{-8\pi\epsilon_i \sqrt{2qm_{eff}\phi_b}}{3h} w \right] \quad (D.9)$$

where  $\alpha$  is a constant,  $w$  is the width of the barrier,  $m_{eff}$  is the effective electron mass,  $q$  is the electron charge,  $\epsilon_i$  is the permittivity,  $h$  is the Plank's constant and  $\phi_b$  is the barrier height.

When an electric field is applied to the structure, the tilting of the bands can be such that the barrier width seen by the electrons is smaller than its actual size, as shown in Figure D.5b. In

## Appendix D. Conduction mechanism

---

this case the current density is given by the following relationship [183, 188]:

$$J_{FN} = \frac{q^2}{8\pi h \phi_b} \frac{V^2}{w^2} \exp \left[ \frac{-8\pi \sqrt{2q m_{eff}} w}{3hV} \phi_b^{\frac{3}{2}} \right] \quad (\text{D.10})$$

where  $\phi_b$  is the barrier height,  $w$  is the width of the barrier,  $m_{eff}$  is the effective electron mass,  $q$  is the electron charge,  $h$  is the Plank's constant and  $V$  is the applied voltage to tilt the bands

## E Silver supercrystals simulations

We have performed *ab initio* calculations, within the density functional theory framework, as implemented in the Quantum Espresso code [189]. The calculations were performed with ultrasoft pseudopotentials [190]. The chosen exchange-correlation functional was the van der Waals corrected rVV10 [191], with the cutoffs converged to 40 Ry for the wavefunctions and 320 Ry for the charge densities, with gamma point calculations. The force convergence criteria was  $1 \times 10^{-3}$  Ry/Bohr, while the structural energy convergence threshold was  $1 \times 10^{-5}$  Ry. The electronic self consistent cycle convergence was  $1 \times 10^{-6}$  Ry.

**Table E.1** – Simulation cell sizes and geometry.

Structure	a	b	c	$\alpha$	$\beta$	$\gamma$
Puck 316	20.40510	20.86650	43.95820	114.9564	93.7561	116.4233
Puck 246	20.82755	22.60275	30.95765	95.2173	90.2599	96.4093

The initial simulation cell of the systems were as obtained from the experimental measurements, with 1168 atoms. Two structures were simulated, both with triclinic cells, as shown in the table E.1. The atomic coordinates were relaxed, but, not the simulation cell. The final relaxed structures are shown in Figure E.1.

From the calculations the switched structure showed a lower energy,  $\Delta_{rVV10} = 0.56$  eV and  $\Delta_{PBE} = 0.15$  eV. The band gaps for the two structures are summarised in Table E.2.

**Table E.2** – Band gaps

Structure	rVV10	PBE
OFF	0.7395 eV	0.7616 eV
ON	0.7457 eV	0.7619 eV

In both cases, unperturbed and switched, the HOMO and LUMO were found on the cluster and on the counterions respectively, as shown in Figure E.2

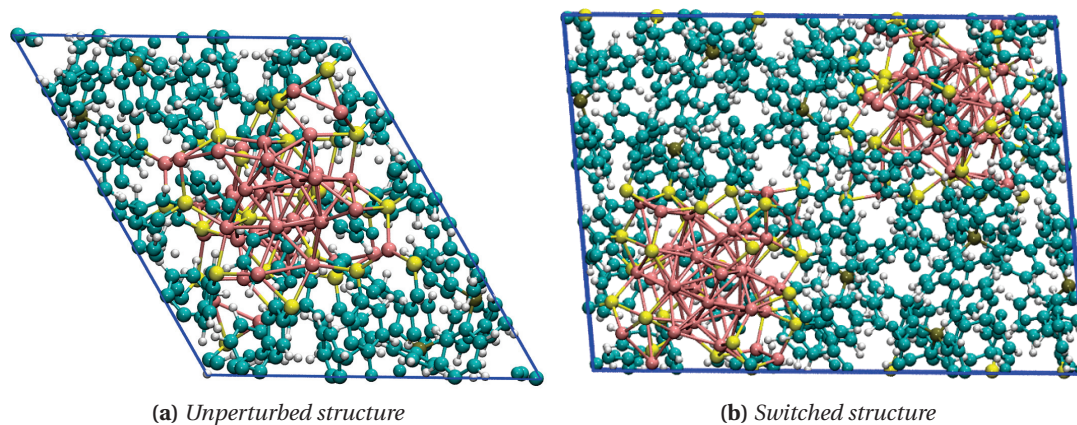


**Figure E.1** – Relaxed simulated structures.

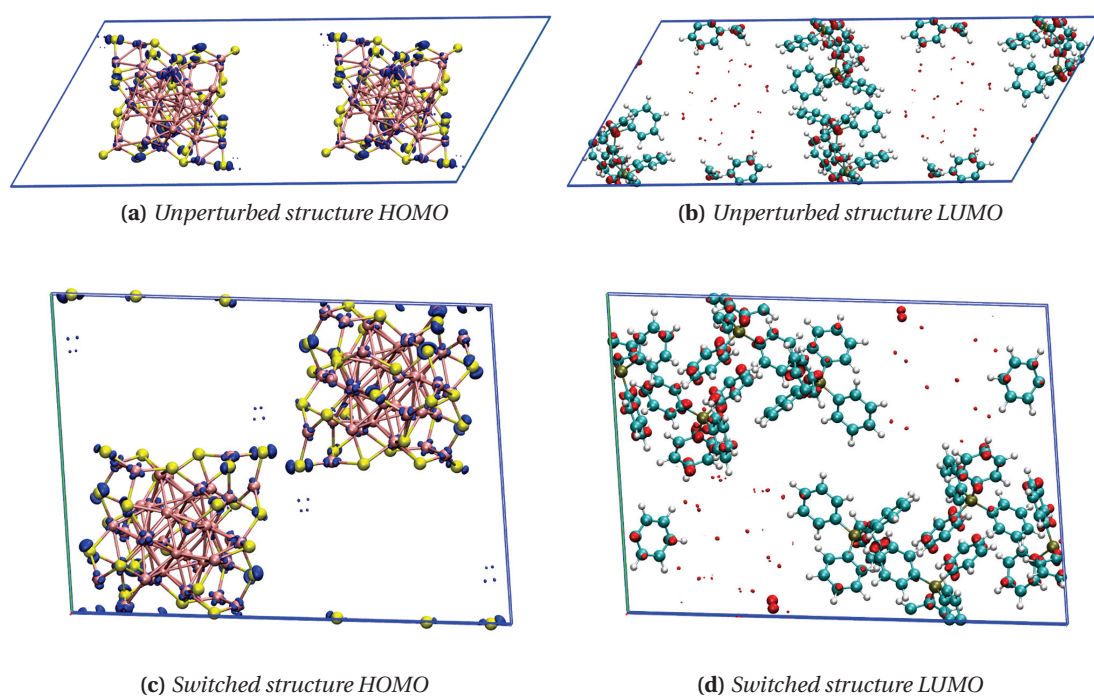


**Figure E.2** – HOMO-LUMO of the simulated structures.



# Bibliography

- [1] R. Feynman. *There is plenty of room at the bottom*. American Physical Society Meeting, 1959.
- [2] R. Feynman. “There’s plenty of room at the bottom”. In: *Engineering and science* 23.5 (1960), pp. 22–36.
- [3] I. Rau et al. “Reaching the magnetic anisotropy limit of a 3d metal atom”. In: *Science* 344.6187 (2014), pp. 988–992.
- [4] F. Donati et al. “Magnetic remanence in single atoms”. In: *Science* 352.6283 (2016), pp. 318–321.
- [5] D. Carr and R. Tiberio. “Direct-write electron beam lithography: history and state of the art”. In: *Material Issues and Modeling for Device Nanofabrication*. Vol. 584. 1999, pp. 33–35.
- [6] G. Binnig, C. Quate, and C. Gerber. “Atomic force microscope”. In: *Physical Review Letters* 56.9 (1986), pp. 930–933.
- [7] G. Binnig. “Tunneling through a controllable vacuum gap”. In: *Applied Physics Letters* 40.2 (1982), pp. 178–180.
- [8] N. Taniguchi. *On the Basic Concept of Nano-Technology*. Proceedings of the International Conference on Production Engineering. 1974.
- [9] L. de Broglie. “The reinterpretation of wave mechanics”. In: *Foundations of Physics* 1.1 (1970), pp. 5–15.
- [10] D.J. Griffiths. *Introduction to Quantum Mechanics*. Pearson Prentice Hall, 2005.
- [11] I. Harald and H. Luth. *Solid-state Physics: An Introduction to Principles of Materials Science*. Advanced texts in physics. Springer London, Limited, 2003.
- [12] R. Kubo and A. Kawabata. “Electronic properties of small particles”. In: *Annual Review of Materials Science* 14.1 (1984), pp. 49–66.
- [13] N.W. Ashcroft and N.D. Mermin. *Solid State Physics*. Brooks Cole, 1976.
- [14] T. Schaaff et al. “Isolation of smaller nanocrystal Au molecules: robust quantum effects in optical spectra”. In: *The Journal of Physical Chemistry B* 101.40 (1997), pp. 7885–7891.

## Bibliography

---

- [15] W. de Heer. "The physics of simple metal clusters: experimental aspects and simple models". In: *Reviews of Modern Physics* 65 (1993), pp. 611–676.
- [16] C. Toumey. "Plenty of room, plenty of history". In: *Nature nanotechnology* 4.12 (2009), pp. 783–784.
- [17] J. Turkevich, P. Cooper Stevenson, and J. Hillier. "A study of the nucleation and growth processes in the synthesis of colloidal gold". In: *Discussions of the Faraday Society* 11 (1951), pp. 55–75.
- [18] L. Chi et al. "Single-electron tunneling in Au<sub>55</sub> cluster monolayers". In: *Applied Physics A Materials Science and Processing* 66.1 (1998), pp. 187–190.
- [19] G. Schmid et al. "Au<sub>55</sub>[P(C<sub>6</sub>H<sub>5</sub>)<sub>3</sub>]<sub>12</sub>Cl<sub>6</sub> - ein goldcluster ungewöhnlicher gröÙe". In: *Chemische Berichte* 114.11 (1981), pp. 3634–3642.
- [20] J. van der Velden et al. "Gold clusters containing bidentate phosphine ligands." In: *Recueil des Travaux Chimiques des Pays-Bas* 100.4 (1981), pp. 148–152.
- [21] G. Schmid. "The relevance of shape and size of Au<sub>55</sub> clusters". In: *Chemical Society Reviews* 37.9 (2008), pp. 1909–1930.
- [22] G. Schmid. "Large clusters and colloids. Metals in the embryonic state". In: *Chemical Reviews* 92.8 (1992), pp. 1709–1727.
- [23] M. Brust et al. "Synthesis of thiol-derivatised gold nanoparticles in a two-phase Liquid-Liquid system". In: *Journal of the Chemical Society, Chemical Communications*. 0.7 (1994), pp. 801–802.
- [24] R. Price and R. Whetten. "All-aromatic, nanometer-scale, gold-cluster thiolate complexes". In: *Journal of the American Chemical Society* 127.40 (2005), pp. 13750–13751.
- [25] S. Kumar, M. Bolan, and T. Bigioni. "Glutathione-stabilized magic-number silver cluster compounds". In: *Journal of the American Chemical Society* 132.38 (2010), pp. 13141–13143.
- [26] Y. Negishi, K. Nobusada, and T. Tsukuda. "Glutathione-protected gold clusters revisited: bridging the gap between gold(I)-thiolate complexes and thiolate-protected gold nanocrystals". In: *Journal of the American Chemical Society* 127.14 (2005), pp. 5261–5270.
- [27] S. Knoppe et al. "Size exclusion chromatography for semipreparative scale separation of Au<sub>38</sub>(SR)<sub>24</sub> and Au<sub>40</sub>(SR)<sub>24</sub> and larger clusters". In: *Analytical Chemistry* 83.13 (2011), pp. 5056–5061.
- [28] M. Branham et al. "Arylthiolate-protected silver quantum dots". In: *Langmuir* 22.26 (2006), pp. 11376–11383.
- [29] O. M Bakr et al. "Silver nanoparticles with broad multiband linear optical absorption." In: *Angewandte Chemie (International ed. in English)* 48.32 (2009), pp. 5921–5926.

- [30] L. Abdul Halim et al. "A scalable synthesis of highly stable and water dispersible  $\text{Ag}_{44}(\text{SR})_{30}$  nanoclusters". In: *Journal of Materials Chemistry A* 1.35 (2013), pp. 10148–10154.
- [31] L. Abdul Halim et al. "Neat and Complete: Thiolate-Ligand Exchange on a Silver Molecular Nanoparticle". In: *Journal of the American Chemical Society* 136.45 (2014), pp. 15865–15868.
- [32] M. Koskinen, P. Lipas, and M. Manninen. "Electron-gas clusters - the ultimate jellium model". In: *Zeitschrift Fur Physik D-Atoms Molecules and Clusters* 35.4 (1995), pp. 285–297.
- [33] F. Catara, P. Chomaz, and N. Van Giai. "Electronic properties of large metal clusters in jellium and pseudo-jellium models". In: *Zeitschrift Fur Physik D-Atoms Molecules and Clusters* 33.3 (1995), pp. 219–227.
- [34] M. Brack. "The physics of simple metal clusters: self-consistent jellium model and semiclassical approaches". In: *Reviews of Modern Physics* 65.3 (1993), p. 677.
- [35] M. Walter et al. "A unified view of ligand-protected gold clusters as superatom complexes." In: *Proceedings of the National Academy of Sciences* 105.27 (2008), pp. 9157–9162.
- [36] W. Knight et al. "Electronic shell structure and abundances of sodium clusters". In: *Physical review letters* 52.24 (1984), pp. 2141–2143.
- [37] N. Khanna and P. Jena. "Assembling crystals from clusters". In: *Physical Review Letters* 69.11 (1992), pp. 1664–1667.
- [38] J. Reveles et al. "Multiple valence superatoms". In: *Proceedings of the National Academy of Sciences* 103.49 (2006), pp. 18405–18410.
- [39] B. Kiran et al. "Magic rule for  $\text{Al}_n\text{H}_m$  magic clusters". In: *Physical Review Letters* 98.25 (2007), pp. 2568021–2568024.
- [40] D. Bergeron et al. "Al cluster superatoms as halogens in polyhalides and as alkaline earths in iodide salts". In: *Science* 307.5707 (2005), pp. 231–235.
- [41] J. Hartig et al. "A metalloid cluster: the Jellium model put to test." In: *Angewandte Chemie (International ed. in English)* 46.10 (2007), pp. 1658–1662.
- [42] B. Yoon et al. "Size-dependent structural evolution and chemical reactivity of gold clusters." In: *ChemPhysChem: a European Journal of Chemical Physics and Physical Chemistry* 8.1 (2007), pp. 157–161.
- [43] M. Walter and H. Häkkinen. "A hollow tetrahedral cage of hexadecagold dianion provides a robust backbone for a tuneable sub-nanometer oxidation and reduction agent via endohedral doping". In: *Physical Chemistry Chemical Physics* 8.46 (2006), pp. 5407–5411.
- [44] A. Wong et al. "Ligand symmetry-equivalence on thiolate protected gold nanoclusters determined by NMR spectroscopy". In: *Nanoscale* 4.14 (2012), pp. 4099–4102.

## Bibliography

---

- [45] Z. Hens and J. Martins. "A solution NMR toolbox for characterizing the surface chemistry of colloidal nanocrystals". In: *Chemistry of Materials* 25.8 (2013), pp. 1211–1221.
- [46] T. Forrester and W. Whalley. "Panoramic mass spectrometer observation". In: *Review of Scientific Instruments* 17.12 (1946), pp. 549–552.
- [47] K. Downard. *Mass spectrometry: a foundation course*. Royal Society of Chemistry, 2004.
- [48] A. Dass et al. "Nanoparticle MALDI-TOF mass spectrometry without fragmentation: Au<sub>25</sub>(SCH<sub>2</sub>CH<sub>2</sub>Ph)<sub>18</sub> and mixed monolayer Au<sub>25</sub>(SCH<sub>2</sub>CH<sub>2</sub>Ph)<sub>18-x</sub>(L)<sub>x</sub>". In: *Journal of the American Chemical Society* 130.18 (2008), pp. 5940–5946.
- [49] H. Qian, Y. Zhu, and R. Jin. "Size-focusing synthesis, optical and electrochemical properties of monodisperse Au<sub>38</sub>(SC<sub>2</sub>H<sub>4</sub>Ph)<sub>24</sub> nanoclusters". In: *ACS Nano* 3.11 (2009), pp. 3795–3803.
- [50] K. Harkness et al. "Ag<sub>44</sub>(SR)<sub>30</sub>(4-): a silver-thiolate superatom complex." In: *Nanoscale* 4.14 (2012), pp. 4269–4274.
- [51] M. Bootharaju et al. "Reversible size control of silver nanoclusters via ligand-exchange". In: *Chemistry of Materials* 27.12 (2015), pp. 4289–4297.
- [52] F. Bertorelle et al. "Synthesis, characterization and optical properties of low nuclearity liganded silver clusters: Ag<sub>31</sub>(SG)<sub>19</sub> and Ag<sub>15</sub>(SG)<sub>11</sub>". In: *Nanoscale* 5.12 (2013), pp. 5637–5643.
- [53] T. Rao, B. Nataraju, and T. Pradeep. "Ag<sub>9</sub> quantum cluster through a solid-state route". In: *Journal of the American Chemical Society* 132.46 (2010), pp. 16304–16307.
- [54] R. Carney et al. "Determination of nanoparticle size distribution together with density or molecular weight by 2D analytical ultracentrifugation". In: *Nature Communications* 2.335 (2011), pp. 1–8.
- [55] G. Mie. "Beiträge zur optik trüber medien, speziell kolloidaler metallösungen". In: *Annalen der Physik* 330.3 (1908), pp. 377–445.
- [56] H. Hulst and H. van de Hulst. *Light scattering by small particles*. Courier Corporation, 1957.
- [57] C. Aikens, S. Li, and G. Schatz. "From discrete electronic states to plasmons: TDDFT optical absorption properties of Ag<sub>n</sub> (n= 10, 20, 35, 56, 84, 120) tetrahedral clusters". In: *The Journal of Physical Chemistry C* 112.30 (2008), pp. 11272–11279.
- [58] H. Qian et al. "Quantum sized gold nanoclusters with atomic precision". In: *Accounts of Chemical Research* 45.9 (2012), pp. 1470–1479.
- [59] Q. Yao et al. "Counterion-assisted shaping of nanocluster supracrystals." In: *Angewandte Chemie (International ed. in English)* 54.1 (2015), pp. 184–189.
- [60] P. Jadzinsky et al. "Structure of a thiol monolayer-protected gold nanoparticle at 1.1 Ångström resolution". In: *Science* 318 (2007), p. 430.
- [61] J. Ascencio et al. "Structure determination of small particles by HREM imaging: theory and experiment". In: *Surface Science* 396.1 (1998), pp. 349–368.

- [62] C. Cleveland et al. "Structural evolution of smaller gold nanocrystals: the truncated decahedral motif". In: *Physical Review Letters* 79.10 (1997), pp. 1873–1876.
- [63] M. Heaven et al. "Crystal structure of the gold nanoparticle  $[\text{Au}_{25}(\text{SCH}_2\text{CH}_2\text{Ph})_{18}]$ ". In: *Journal of the American Chemical Society* 130.12 (2008), pp. 3754–3755.
- [64] M. Zhu et al. "Correlating the crystal structure of a thiol-protected  $\text{Au}_{25}$  cluster and optical properties". In: *Journal of the American Chemical Society* 130.18 (2008), pp. 5883–5885.
- [65] H. Yang et al. "All-thiol-stabilized  $\text{Ag}_{44}$  and  $\text{Au}_{12}\text{Ag}_{32}$  nanoparticles with single-crystal structures." In: *Nature Communications* 4 (2013), pp. 2422–2430.
- [66] A. Desireddy et al. "Ultrastable silver nanoparticles." In: *Nature* 501.7467 (2013), pp. 399–402.
- [67] B. Yoon et al. "Hydrogen-bonded structure and mechanical chiral response of a silver nanoparticle superlattice." In: *Nature Materials* 13.8 (2014), pp. 807–811.
- [68] S. Knoppe, S. Michalet, and T. Bürgi. "Stabilization of thiolate-protected gold clusters against thermal inversion: diastereomeric  $\text{Au}_{38}(\text{SCH}_2\text{CH}_2\text{Ph})_{24-2x}(\text{R-BINAS})_x$ ". In: *The Journal of Physical Chemistry C* 117.29 (2013), pp. 15354–15361.
- [69] A. Guerrero-Martínez et al. "From individual to collective chirality in metal nanoparticles". In: *Nano Today* 6.4 (2011), pp. 381–400.
- [70] C. Noguez and I. Garzon. "Optically active metal nanoparticles". In: *Chemical Society Reviews* 38.3 (2009), pp. 757–771.
- [71] S. Knoppe and T. Bürgi. "Chirality in thiolate-protected gold clusters". In: *Accounts of Chemical Research* 47.4 (2014), pp. 1318–1326.
- [72] C. Zeng et al. "Chiral structure of thiolate-protected 28-gold-atom nanocluster determined by x-ray crystallography". In: *Journal of the American Chemical Society* 135.27 (2013), pp. 10011–10013.
- [73] S. Knoppe et al. "Ligand exchange reactions on  $\text{Au}_{38}$  and  $\text{Au}_{40}$  clusters: a combined circular dichroism and mass spectrometry study". In: *Journal of the American Chemical Society* 132.47 (2010), pp. 16783–16789.
- [74] C. Gautier and T. Bürgi. "Chiral gold nanoparticles". In: *ChemPhysChem: a European Journal of Chemical Physics and Physical Chemistry* 10.3 (2009), pp. 483–492.
- [75] I. Dolamic et al. "First enantioseparation and circular dichroism spectra of  $\text{Au}_{38}$  clusters protected by achiral ligands". In: *Nature Communications* 3.798 (2012), pp. 1–6.
- [76] S. Si et al. "Ligand exchange on  $\text{Au}_{25}$  cluster with chiral thiols". In: *The Journal of Physical Chemistry C* 113.30 (2009), pp. 12966–12969.
- [77] C. Gautier and T. Bürgi. "Chiral n-isobutyryl-cysteine protected gold nanoparticles: preparation, size selection, and optical activity in the uv-vis and infrared". In: *Journal of the American Chemical Society* 128.34 (2006), pp. 11079–11087.

## Bibliography

---

- [78] M. Farrag, M. Tschurl, and U. Heiz. “Chiral gold and silver nanoclusters: preparation, size selection, and chiroptical properties”. In: *Chemistry of Materials* 25.6 (2013), pp. 862–870.
- [79] Y. Liu et al. “Synthesis of chiral silver nanoclusters capped with small molecules”. In: *Colloids and Surfaces A: Physicochemical and Engineering Aspects* 426 (2013), pp. 12–17.
- [80] S. Swasey et al. “Chiral electronic transitions in fluorescent silver clusters stabilized by DNA”. In: *ACS Nano* 8.7 (2014), pp. 6883–6892.
- [81] J. Petty et al. “A segregated, partially oxidized, and compact Ag<sub>10</sub> cluster within an encapsulating DNA host”. In: *Journal of the American Chemical Society* 138.10 (2016), pp. 3469–3477.
- [82] G. Hutchings. “Access granted”. In: *Nature Chemistry* 2.12 (2010), pp. 1005–1006.
- [83] F. Zaera. “Nanostructured materials for applications in heterogeneous catalysis”. In: *Chemical Society Reviews* 42.7 (2013), pp. 2746–2762.
- [84] M. Nigra, J. Ha, and A. Katz. “Identification of site requirements for reduction of 4-nitrophenol using gold nanoparticle catalysts”. In: *Catalysis Science and Technology* 3.11 (2013), pp. 2976–2983.
- [85] N. de Silva et al. “A bioinspired approach for controlling accessibility in calix[4]arene-bound metal cluster catalysts”. In: *Nature Chemistry* 2.12 (2010), pp. 1062–1068.
- [86] A. Corma and H. Garcia. “Supported gold nanoparticles as catalysts for organic reactions”. In: *Chemical Society Reviews* 37.9 (2008), pp. 2096–2126.
- [87] A. Ghosh et al. “Simple and efficient separation of atomically precise noble metal clusters”. In: *Analytical Chemistry* 86.24 (2014), pp. 12185–12190.
- [88] X. Chen and H. Häkkinen. “Protected but accessible: oxygen activation by a calixarene-stabilized undecagold cluster”. In: *Journal of the American Chemical Society* 135.35 (2013), pp. 12944–12947.
- [89] J. Lu et al. “Effect of the size-selective silver clusters on lithium peroxide morphology in lithium–oxygen batteries”. In: *Nature Communications* 5 (2014), pp. 1–8.
- [90] Y. Lu and W. Chen. “Size effect of silver nanoclusters on their catalytic activity for oxygen electro-reduction”. In: *Journal of Power Sources* 197 (2012), pp. 107–110.
- [91] I. Chakraborty et al. “Atomically precise silver clusters as new SERS substrates”. In: *The Journal of Physical Chemistry Letters* 4.16 (2013), pp. 2769–2773.
- [92] R. White. *Quantum Theory of Magnetism: Magnetic Properties of Materials*. Springer Series in Solid State Sciences. Springer, 2007.
- [93] M. Zhu et al. “Reversible switching of magnetism in thiolate-protected Au<sub>25</sub>superatoms”. In: *Journal of the American Chemical Society* 131.7 (2009), pp. 2490–2492.
- [94] M. Pereiro, D. Baldomir, and J. Arias. “Unexpected magnetism of small silver clusters”. In: *Physical Review A* 75.6 (2007), pp. 0632041–0632046.

- [95] Y. Negishi et al. "X-ray magnetic circular dichroism of size-selected, thiolated gold clusters". In: *Journal of the American Chemical Society* 128.37 (2006), pp. 12034–12035.
- [96] Y. Yamamoto et al. "Direct observation of ferromagnetic spin polarization in gold nanoparticles." In: *Physical Review Letters* 93.11 (1994), pp. 1168011–1168014.
- [97] W. Luo, S. Pennycook, and S. Pantelides. "s-Electron Ferromagnetism in Gold and Silver Nanoclusters". In: *Nano Letters* 7.10 (2007), pp. 3134–3137.
- [98] P. Crespo et al. "Permanent magnetism, magnetic anisotropy, and hysteresis of thiol-capped gold nanoparticles". In: *Physical Review Letters* 93.8 (2004), pp. 0872041–0872044.
- [99] R. Desiraju. "Supramolecular synthons in crystal engineering - a new organic-synthesis". In: *Angewandte Chemie (International ed. in English)* 34.21 (1995), pp. 2311–2327.
- [100] R. Lakes. "Deformation mechanisms in negative Poisson's ratio materials: structural aspects". In: *Journal of Materials Science* 26.9 (1991), pp. 2287–2292.
- [101] M. Brust et al. "Synthesis and reactions of functionalised gold nanoparticles". In: *Journal of the Chemical Society, Chemical Communications* 16 (1995), pp. 1655–1656.
- [102] L. Abdul Halim. "Silver Nanoclusters: From Design Principles to Practical Applications". PhD thesis. KAUST, 2015.
- [103] M. Pelton et al. "Long-lived charge-separated states in ligand-stabilized silver clusters." In: *Journal of the American Chemical Society* 134.29 (2012), pp. 11856–11859.
- [104] A. Mersmann. *Crystallization Technology Handbook*. CRC Press, 2001.
- [105] G. Desiraju. *Crystal Design: Structure and Sunction*. Wiley, 2003.
- [106] M. Benvenuti and S. Mangani. "Crystallization of soluble proteins in vapor diffusion for x-ray crystallography". In: *Nature Protocols* 2.7 (2007), pp. 1633–1651.
- [107] B. Chopard, H. Herrmann, and T. Vicsek. "Structure and growth mechanism of mineral dendrites". In: *Nature* 353.6343 (1991), pp. 409–412.
- [108] J. Fang et al. "Dendritic silver nanostructure growth and evolution in replacement reaction". In: *Crystal Growth and Design* 7.5 (2007), pp. 864–867.
- [109] H. Ibach and H. Luth. *Solid-State Physics: An Introduction to Principles of Materials Science*. Advanced texts in physics. Springer London, Limited, 2009.
- [110] B. Warren. *X-ray Diffraction*. Courier Corporation, 1969.
- [111] E. Sánchez, J. Krug, and X. Xie. "Ion and electron beam assisted growth of nanometric  $\text{Si}_m\text{O}_n$  structures for near-field microscopy". In: *Review of Scientific Instruments* 73.11 (2002), pp. 3901–3907.
- [112] J. Orloff, L. Swanson, and M. Utlaut. *The Physics of Liquid Metal Ion Sources and Ion Optics and Their Application to Focused Ion Beam Technology*. Springer Science & Business Media, 2003.

## Bibliography

---

- [113] Y. Takai et al. “Transport properties of Pt nanowires fabricated by beam-induced deposition”. In: *Japanese Journal of Applied Physics* 44.7 (2005), pp. 5683–5686.
- [114] A. Vaz et al. “Platinum thin films deposited on silicon oxide by focused ion beam: characterization and application”. In: *Journal of Materials Science* 43.10 (2008), pp. 3429–3434.
- [115] C. D. Geddes. *Reviews in Plasmonics 2015*. Springer International Publishing, 2016.
- [116] J. Chamberlain. “On a relation between absorption strength and refractive index”. In: *Infrared Physics* 5.4 (1965), p. 175.
- [117] K. Yamamoto and H. Ishida. “Kramers-Kronig analysis applied to reflection-absorption spectroscopy”. In: *Vibrational Spectroscopy* 15.1 (1997), pp. 27–36.
- [118] V. Lucarini et al. *Kramers-Kronig Relations in Optical Materials Research*. Springer Science and Business Media, Apr. 2005.
- [119] R. Feynman, R. Leighton, and M. Sands. *The Feynman Lectures on Physics*. Addison-Wesley Publishing Company, 1964.
- [120] S. Orfanidis. *Electromagnetic Waves and Antennas*. Rutgers University New Brunswick, NJ, 2002.
- [121] J. Seybold. *Introduction to RF Propagation*. John Wiley & Sons, 2005.
- [122] L. Gell and H. Häkkinen. “Theoretical analysis of the  $M_{12}Ag_{32}(SR)_{40}^{4-}$  and  $X@M_{12}Ag_{32}(SR)_{40}^{4-}$  nanoclusters.” In: *The Journal of Physical Chemistry C* 119.20 (2015), pp. 10943–10948.
- [123] I. Chakraborty et al. “ $Ag_{44}(SeR)_{30}$ : A hollow cage silver cluster with selenolate protection”. In: *The Journal of Physical Chemistry Letters* 4.19 (2013), pp. 3351–3355.
- [124] A. Allain et al. “Electrical contacts to two-dimensional semiconductors”. In: *Nature Materials* 14.12 (2015), pp. 1195–1205.
- [125] H. Michaelson. “The work function of the elements and its periodicity”. In: *Journal of Applied Physics* 48.11 (1977), pp. 4729–4733.
- [126] P. Agarwal, S. Bhattacharyya, and D. Ghose. “Transient effect in light emission during oxygen ion bombardment of a beryllium-copper target”. In: *Applied Surface Science* 133.3 (1998), pp. 166–170.
- [127] M. Rodríguez, I. Bonalde, and E. Medina. “Pre-factor effect in the Efros-Shklovskii variable range hopping regime”. In: *Low Temperature Physics: : 24th International Conference on Low Temperature Physics; LT24 850* (2006), pp. 1466–1467.
- [128] I. Beloborodov, A. Lopatin, and V. Vinokur. “Coulomb effects and hopping transport in granular metals”. In: *Physical Review B* 72.12 (2005), pp. 1251211–12512120.
- [129] T. Abraham et al. “Efros-Shklovskii variable range hopping transport in nanocluster metallic films”. In: *Journal of Applied Physics* 111.10 (2012), pp. 1043181–1043184.
- [130] B. Skinner, T. Chen, and B. Shklovskii. “Theory of hopping conduction in arrays of doped semiconductor nanocrystals”. In: *Physical Review B* 85.20 (2012), pp. 2053161–20531613.



- [131] J. Dugay et al. "Charge transport and interdot coupling tuned by the tunnel barrier length in assemblies of nanoparticles surrounded by organic ligands". In: *Physical Review B* 89.4 (2014), pp. 0414061–0414065.
- [132] N. Bodappa et al. "Controlled assembly and single electron charging of monolayer protected Au<sub>144</sub> clusters: an electrochemistry and scanning tunneling spectroscopy study". In: *Nanoscale* 6.24 (2014), pp. 15117–15126.
- [133] Q. Li et al. "Structure-dependent electrical properties of carbon nanotube fibers". In: *Advanced Materials* 19.20 (2007), pp. 3358–3363.
- [134] P. Pipinys and A. Kiveris. "Variable range hopping and/or phonon-assisted tunneling mechanism of electronic transport in polymers and carbon nanotubes". In: *Central European Journal of Physics* 10.2 (2012), pp. 271–281.
- [135] L. Zuppiroli et al. "Hopping in disordered conducting polymers." In: *Physical Review. B* 50.8 (1994), pp. 5196–5203.
- [136] N. Mott. "Amorphous and Liquid Semiconductors Introductory talk; Conduction in non-crystalline materials". In: *Journal of Non-Crystalline Solids* 8 (1972), pp. 1–18.
- [137] M. Dias, H. Stumpf, and R. Mambrini. "A new molecular magnetic semiconductor based on tetrathiafulvalene (tff) and oxamato ligand (opba):[tff]<sub>2</sub> [Cu (opba)] H<sub>2</sub>O". In: *Journal of the Brazilian Chemical Society* 21.7 (2010), pp. 1274–1282.
- [138] S. Sze and K. Ng. *Physics of Semiconductor Devices*. John Wiley & Sons, 2006.
- [139] H. Gleskova et al. "Field-effect mobility of amorphous silicon thin-film transistors under strain". In: *Journal of Non-Crystalline Solids* 338-340 (2004), pp. 732–735.
- [140] A. Moore. "Electron and hole drift mobility in amorphous silicon". In: *Applied Physics Letters* 31.11 (1977), pp. 762–764.
- [141] I. McCulloch, A. Salleo, and M. Chabinyc. "Avoid the kinks when measuring mobility". In: *Science* 352.6293 (2016), pp. 1521–1522.
- [142] C. Reese and Z. Bao. "Overestimation of the field-effect mobility via transconductance measurements and the origin of the output/transfer characteristic discrepancy in organic field-effect transistors". In: *Journal of Applied Physics* 105.2 (2009), pp. 0245061–0245068.
- [143] H. Yi et al. "Vacuum lamination approach to fabrication of high-performance single-crystal organic field-effect transistors". In: *Advanced Materials* 23.48 (2011), pp. 5807–5811.
- [144] D. Braga et al. "Bulk electrical properties of rubrene single crystals: Measurements and analysis". In: *Physical Review B* 77.11 (2008), pp. 1152051–1152054.
- [145] M. Lampert. "Simplified theory of space-charge-limited currents in an insulator with traps". In: *Physical review letter* 103.6 (1956), pp. 1648–1656.

## Bibliography

---

- [146] A. Molinari et al. "High electron mobility in vacuum and ambient for PDIF-CN<sub>2</sub> single-crystal transistors". In: *Journal of the American Chemical Society* 131.7 (2009), pp. 2462–2463.
- [147] C. Shin et al. "Fast, exact, and non-destructive diagnoses of contact failures in nano-scale semiconductor device using conductive AFM". In: *Scientific Reports* 3 (2013), p. 2088.
- [148] S. Hunter and T. Anthopoulos. "Observation of unusual, highly conductive grain boundaries in high-mobility phase separated organic semiconducting blend films probed by lateral-transport conductive-AFM". In: *Advanced Materials* 25.31 (2013), pp. 4320–4326.
- [149] A. Mishchenko et al. "Fluorination clusters on graphene resolved by conductive AFM". In: *Nanomaterials for Security*. Springer, 2016, pp. 19–24.
- [150] L. Palatinus and G. Chapuis. "SUPERFLIP - a computer program for the solution of crystal structures by charge flipping in arbitrary dimensions". In: *Journal of Applied Crystallography* 40.4 (2007), pp. 786–790.
- [151] O. Dolomanov et al. "OLEX2: a complete structure solution, refinement and analysis program". In: *Journal of Applied Crystallography* 42.2 (2009), pp. 339–341.
- [152] G. Sheldrick. "A short history of SHELX." In: *Acta crystallographica. Section A, Foundations of crystallography* 64.1 (2008), pp. 112–122.
- [153] P. Sheng. "Fluctuation-induced tunneling conduction in disordered materials". In: *Physical Review B* 21 (6 1980), pp. 2180–2196.
- [154] L. Zhong et al. "Resistive switching of Cu/SiC/Au memory devices with a high ON/OFF ratio". In: *Solid-State Electronics* 94 (2014), pp. 98–102.
- [155] N. Mott. "Metal-insulator transition". In: *Reviews of Modern Physics* 40 (1968), pp. 677–683.
- [156] H. Moreira et al. "Electron cotunneling transport in gold nanocrystal arrays". In: *Physical Review Letters* 107.17 (2011), pp. 1768031–1768035.
- [157] P. Yang et al. "Electronic properties of supracrystals of Au nanocrystals: influence of thickness and nanocrystallinity." In: *Journal of physics. Condensed matter: an Institute of Physics journal* 25.33 (2013), pp. 3353021–335306.
- [158] M. Gilbert Gatty et al. "Hopping versus tunneling mechanism for long-range electron transfer in porphyrin oligomer bridged donor–acceptor systems". In: *The Journal of Physical Chemistry B* 119.24 (2015), pp. 7598–7611.
- [159] L. Xiang et al. "Intermediate tunnelling-hopping regime in DNA charge transport". In: *Nature Chemistry* 7.3 (2015), pp. 221–226.
- [160] A. Zabet-Khosousi and A. Dhirani. "Charge transport in nanoparticle assemblies". In: *Chemical Reviews* 108.10 (2008), pp. 4072–4124.

- [161] M. Fogler, S. Teber, and I. Shklovskii. “Variable-range hopping in quasi-one-dimensional electron crystals”. In: *Physical Review B* 69.3 (2004), pp. 0354131–03541318.
- [162] M. Errai et al. “Crossover from Efros-Shklovskii to Mott variable range hopping in amorphous thin  $\text{Ni}_x\text{Si}_{1-x}$  films”. In: *Chinese Journal of Physics* 52.1 (2014), pp. 251–261.
- [163] H. Song et al. “Observation of molecular orbital gating”. In: *Nature* 462.7276 (2009), pp. 1039–1043.
- [164] L. Esaki and R. Tsu. “Superlattice and negative differential conductivity in semiconductors”. In: *IBM Journal of Research and Development* 14.1 (1970), p. 61.
- [165] R. Tsu and L. Esaki. “Tunneling in a finite superlattice”. In: *Applied Physics Letters* 22.11 (1973), pp. 562–564.
- [166] M. Perrin et al. “Single-molecule resonant tunneling diode”. In: *The Journal of Physical Chemistry C* 119.10 (2015), pp. 5697–5702.
- [167] R. Waser and M. Aono. “Nanoionics-based resistive switching memories”. In: *Nature Materials* 6.11 (2007), pp. 833–840.
- [168] L. Britnell et al. “Resonant tunnelling and negative differential conductance in graphene transistors”. In: *Nature Communications* 4 (2013), pp. 1794–1795.
- [169] N. Guenifi and D. Bauza. “Characterization of Slow Trap in MOS Capacitor”. In: *African Physical Review* 2.21 (2009), pp. 44–45.
- [170] M. Buttiker. “Coherent and sequential tunneling in series barriers”. In: *IBM Journal of Research and Development* 32.1 (1988), pp. 63–75.
- [171] M. Buttiker and R. Landauer. “traversal time for tunneling”. In: *Physical Review Letters* 49 (1982), pp. 1739–1742.
- [172] F. Capasso et al. “Effective mass filtering: giant quantum amplification of the photocurrent in a semiconductor superlattice”. In: *Applied Physics Letters* 47.4 (1985), pp. 420–422.
- [173] F. Capasso, K. Mohammed, and A. Cho. “Resonant tunneling through double barriers, perpendicular quantum transport phenomena in superlattices, and their device applications”. In: *IEEE Journal of Quantum Electronics* 22.9 (1986), pp. 1853–1869.
- [174] F. Redl et al. “Three-dimensional binary superlattices of magnetic nanocrystals and semiconductor quantum dots.” In: *Nature* 423.6943 (2003), pp. 968–971.
- [175] T. Trindade, P. O’Brien, and N. Pickett. “Nanocrystalline semiconductors: synthesis, properties, and perspectives”. In: *Chemistry of Materials* 13.11 (2001), pp. 3843–3858.
- [176] D. Shi et al. “Low trap-state density and long carrier diffusion in organolead trihalide perovskite single crystals”. In: *Science* 347.6221 (2015), pp. 519–522.
- [177] C. Wagner. “Physical chemistry of ionic crystals involving small concentrations of foreign substances”. In: *The Journal of Physical Chemistry* 57 (1953), pp. 738–742.

## Bibliography

---

- [178] Y. Hirose and H. Hirose. “Polarity-dependent memory switching and behavior of Ag dendrite in Ag-photodoped amorphous  $\text{As}_2\text{S}_3$  films”. In: *Journal of Applied Physics* 47.6 (1976), pp. 2767–2772.
- [179] T. Aono et al. “Switching property of atomic switch controlled by solid electrochemical reaction”. In: *Japanese Journal of Applied Physics* 45.4 (2006), pp. 364–366.
- [180] L. Chua. “Memristor-the missing circuit element”. In: *IEEE Transactions on Circuit Theory* (1971).
- [181] E. Murphy and R. Good. “Thermionic emission, field emission, and the transition region”. In: *Phys. Rev.* 102 (1956), pp. 1464–1473.
- [182] S. Pollack. “Schottky field emission through insulating layers”. In: *Journal of Applied Physics* 34.4 (1963), pp. 877–880.
- [183] J. Simmons. “Generalized formula for the electric tunnel effect between similar electrodes separated by a thin insulating film”. In: *Journal of Applied Physics* 34.6 (1963), pp. 1793–1803.
- [184] S. Colella et al. “Titanium dioxide mesoporous electrodes for solid-state dye-sensitized solar cells: cross-analysis of the critical parameters”. In: *Advanced Energy Materials* 4.9 (2014), pp. 13013621–13013626.
- [185] I. Ben-Yaacov and U. Mishra. *Unipolar Space Charge Limited Transport*. 2004.
- [186] A. Efros and B. Shklovskii. “Coulomb gap and low temperature conductivity of disordered systems”. In: *Journal of Physics C: Solid State Physics* 8.4 (1975), pp. 49–51.
- [187] E. Lim and R. Ismail. “Conduction mechanism of valence change resistive switching memory: a survey”. In: *Electronics* 4.3 (2015), pp. 586–613.
- [188] R. Fowler and L. Nordheim. “Electron emission in intense electric fields”. In: *Proceedings of the Royal Society A: Mathematical, Physical and Engineering Sciences* 119.781 (1928), pp. 173–181.
- [189] P. Giannozzi et al. “Quantum Espresso: a modular and open-source software project for quantum simulations of materials”. In: *Journal of Physics: Condensed Matter* 21.39 (2009), pp. 3955021–39550219.
- [190] D. Vanderbilt. “Soft self-consistent pseudopotentials in a generalized eigenvalue formalism”. In: *Physical Review B* 41.11 (1990), pp. 7892–7895.
- [191] R. Sabatini, T. Gorni, and S. De Gironcoli. “Nonlocal van der Waals density functional made simple and efficient”. In: *Physical Review B - Condensed Matter and Materials Physics* 87.4 (2013), pp. 4–7.

# SERGIO ALLEGRI

## PERSONAL DATA

*Date of Birth:* 4<sup>th</sup> February 1986  
*Nationality:* Italian  
*Email:* [sergio.allegri@gmail.com](mailto:sergio.allegri@gmail.com)  
*Mobile:* +41 76 6713507  
*Address:* Route du Lac 13, 1026 Denges (CH)



## ACADEMIC AND WORK EXPERIENCES

*Physics of silver nanoclusters*      2012 - present      PhD student EPFL, Switzerland  
*Supramolecular Nano-Materials and Interfaces Laboratory*, From June 2012. Advisor Prof. Francesco Stellacci. I am currently finishing my PhD, which was focused on the study of metal nanoclusters as a new family of materials. My task is to address the challenging physics that lies underneath the experimental observations of silver nanoclusters. The enticing properties, that this material exhibit, make it an excellent candidate for the next generation compound for electronics and sensing applications.

*Molecular Plasmonics*      2011-2012      Research assistant EPFL, Switzerland  
*Nanophotonics and Metrology Laboratory*, From September 2011 to April 2012. Engineering of the decay rates of fluorophores in plasmonic structures.

*Enhancing NV centers in diamond*      2010-2011      Research assistant Columbia University, NY  
*Quantum Photonics Group*, Electrical Engineering Department. From July 2010 to July 2011. Supervisor Prof. Dirk R. Englund. I enhanced the emitted fluorescence of NV centers in diamond through light-matter coupling to plasmonic structures, which resulted to be a successful step in utilising this material as label in biological applications.

*1550 nm Laser Characterization*      Spring 2008      Internship at Avago Technologies, Torino  
*III-V Semiconductor Laser Characterization*. Supervisor Dr. Filippo Ghiglieno. Characterization of 1550 nm lasers for 10 GHz telecommunication.

## EDUCATION

*Master of Science in Engineering*      2011      Politecnico di Torino, Italy  
110/110 *cum laude* · Major: Physics Engineering  
Thesis: "NV center in diamond. Emission enhancement assisted by surface plasmons"  
Advisor: Prof. Fabrizio GIORGIS

*Bachelor Degree*      2008      Politecnico di Torino, Italy  
110/110 · Major: Physics Engineering  
Thesis: "Characterization of III-V Semiconductor Lasers"  
Advisor: Prof. Fabrizio PIRRI

## ACADEMIC INFORMATIONS

- Conferences*
- HOPV 2014 : The 6th International Conference on Hybrid and Organic Photovoltaics ,11-14 May 2014.
- MNE 2014 : The 40th International Conference on Micro and Nano Engineering, September 2014.
- ECME 2015 : The 13th European Conference on Molecular Electronics, 1-5 September 2015.
- Publications*
- Le Ouay, B., Guldin, S., Luo, Z., **Allegri, S.**, Stellacci, F. (2016). Freestanding Ultrathin Nanoparticle Membranes Assembled at Transient LiquidLiquid Interfaces. *Advanced Materials Interfaces*.
- Hodges, J. S., Li, L., Lu, M., Chen, E. H., Trusheim, M. E., **Allegri, S.**, Englund, D. (2012). Long-lived NV- spin coherence in high-purity diamond membranes. *New Journal of Physics*.
- Teaching*
- Teaching assistant in the course of Thermodynamics for four years (2012-2015)
- I supervised both bachelor and master students in their semester projects, as well as summer interns
- Organizer of the winter school: **Winscool** - "New materials from physics to application", held in Champéry (CH), which had attendants from all Europe. Michael Graetzel (EPFL), Claire Grey (Cambridge Univ.), Jerome Faist (ETHZ) and Garcia de Abajo (ICFO) were among the invited speakers.
- Teacher of the course of "Fisica energetica" at the "Fondazione Casa di Carità Arti e Mestieri" (Ivrea - Torino) during the spring semester in 2010.

## ADDITIONAL INFORMATIONS

- Laboratory Experiences*
- Autocorrelation measurements, Spectrometer, Electrical characterization, single crystal XRD, EDX, SEM, AFM, confocal fluorescence microscopy, spectroscopy and microspectroscopy.
- Familiar with most of the common microfabrication techniques, such as e-beam and thermal evaporator, photo and e-beam lithography, sputtering, RIE, wet and dry etching
- Computing Skills*
- WORD PROCESSING : L<sup>A</sup>T<sub>E</sub>X, Microsoft Office Suite, Open Office
- OTHER TOOLS : Mathematica, Matlab, GNU Octave
- PLATFORMS : Windows, Mac OS, Linux/Unix
- LANGUAGES : C/C++
- Languages*
- ENGLISH · Full professional proficiency.
- FRENCH · Fluent speaker, excellent reader, poor writer.
- ITALIAN · Native speaker.
- Personal skills*
- Proud rugby player: thanks to this activity, practised for over 10 years, I developed a strong capability to cooperate, help and lead a team.
- During my free time I enjoy cycling, both on and off-roads. I am fond of all sorts of outdoor activities, especially if they involve effort and mental discipline.
- My educational path, from the humanities to science, has given me the opportunity to develop a genuine curiosity in any new environment and to appreciate the potential of multidisciplinary approaches in solving a problem

